THE DECAY PROPERTIES OF THE $\psi(3770)$

Thesis by

Yanong Zhu

In Partial Fulfillment of the Requirements

for the Degree of

Doctor of Philosophy

California Institute of Technology

Pasadena, California

1989

(Submitted July 19, 1988)

ACKNOWLEDGMENTS

I would like to thank every one in the Mark III collaboration for being my friends and teachers in the past years. I would like to thank R. Schindler, who started me on my first analysis, and W. Toki and A. Odian who have provided many suggestions and helpful discussions. Especially, I would like to thank my old friends, A. Seiden, C. Heusch, H. Sadrozinski and R. Xu for their friendship in the past eight years, which has made Mark III feel like a family.

I owe many words of appreciation to my thesis advisor David G. Hitlin. He encouraged me when I faced difficulties, lit the way when I was in the dark, and provided help when I needed it. He made my time at Caltech more enjoyable and let me have freedom for developing my own ideas and interests.

For two years, I have shared an office with G. Dubois. I have had many interesting discussions with him covering many topics and have received much help from him. I have certainly benefited from those and therefore would like to thank him.

Two years ago, W. Wisniewski and A. Mincer came to Caltech. Since then, they have provided many very useful discussions, and much advice and help. I would like to thank them for all they did.

I have enjoyed discusses and friendships with many people in Mark III, including C. Matthews, F. DeJongh, G. Eigen, S. Wasserbaech, T. Bolton, D. Coffman, I. Stockdale, C. Grab and G. Blaylock.

I would also like to thank T. Yan, M. Wise, M. Peskin and D. Silverman for conversations, calculations and suggestions.

Finally, I thank my uncle C.T. Hsiung, who has supported my education in this country, my parents, who have loved me at all times, and my wife Claire, who has shared both my happiness and sadness with love.

ABSTRACT

The decays of the $\psi(3770)$ resonance to final states that do not contain charmed D mesons are measured for the first time. Using a sample of $9.3pb^{-1}$ of e^+e^- annihilations at $\sqrt{s} = 3.77$ GeV, collected with the Mark III detector at SPEAR, we have measured the branching ratio for the decays $\psi(3770) \rightarrow J/\psi\pi^+\pi^-$ and $\gamma\chi_J$. These branching ratios together with the electronic widths of the $\psi(3685)$ and $\psi(3770)$ are used to determine the mixing angle between the 2^3S_1 and 1^3D_1 Charmonium states and are compared with a number of predictions. In addition, evidence is found for other non–$D\bar{D}$ hadronic final states, such as 3π, 4π, and 5π, as well as $\eta 2\pi$, $\eta 4\pi$, $\bar{p}p2\pi$ and $\bar{p}p3\pi$.

Table of Contents

List of Tables

List of Figures

1. INTRODUCTION

1.1 OVERVIEW

There are two classes of resonances found in the charmonium system. The first class having a mass greater than 3.74 GeV/c^2 can decay into a pair of charmed mesons, while the second, having masses below 3.74 GeV/c^2, can not.

Many resonances of the charmonium system have been observed: η_c, J/ψ, χ_J, and $\psi(3685)$ below the charmed threshold and $\psi(3770)$, $\psi(4030)$, $\psi(4160)$, $\psi(4415)$ above the threshold[2]. These resonances provide a rich source for the study of the interactions of quarks at relatively low energy.

The $\psi(3770)$ is a very interesting state of the $c\bar{c}$ family. It is the first $c\bar{c}$ state above the charmed meson production threshold and is 80 MeV above the $\psi(3685)$, which is below the charm threshold and is well studied. It is also assumed to have a large D-wave component in its wave function in the non-relativistic quarkonium model, and is the only state with orbit angular momentum 2, which has been experimentally accessible in a heavy quark system.

A state above the charmed meson threshold can, in principle, decay into five major channels: 1) the c and $\bar{c}$ can annihilate into three gluons (Fig. 1.4.1); 2) it can annihilate into two gluons and one photon (Fig. 1.4.2); 3) it can radiate gluons or photons, making a transition to a lower energy charmonium state (Fig. 1.5.1 and Fig. 1.6.1); and 5) it can decay into a pair of charmed mesons (Fig. 1.7.1).

In the past, it has been assumed that the dominant decays of $\psi(3770)$ would be $D\bar{D}$ decays[3]. Recently, however, several problems stimulated interest in looking into the non-$D\bar{D}$ decays in more detail. First, there is no direct evidence indicating that $D\bar{D}$ is the only $\psi(3770)$ decay channel. Second, as discussed later, the mixing of $c\bar{c}$ states can have a large effect on the EM (electromagnetic) transition rates of both the $\psi(3685)$ and $\psi(3770)$. This is an old problem; it has long been noticed that there are discrepancies between the predicted and

Experiment	$\sigma_{\psi(3770)}$ (nb)
Crystal Ball[39]	6.7±0.9
Delco[39]	≃6
Lead Glass Wall[44]	10.3 ± 1.6
Mark II[37]	9.3±1.4
Mark III[5]	5.0±0.5

Table 1.I. $\psi(3770)$ cross section.

experimental EM transition rates for the decays of the $\psi(3685)$ into χ_J even with relativistic corrections[6,21,22,13]. This discrepancy could be caused by the mixing of the S and D wave components of the $c\bar{c}$ resonances[40,47]. Third, the ratio of the annihilation rates of the J/ψ and $\psi(3685)$ are not constant for different decay modes[8,23]. We would therefore like to find the annihilation rates of the $\psi(3770)$ into these modes. Finally, the Mark III experiment has the ability to search for non-$D\bar{D}$ decays of the $\psi(3770)$ because of its high photon detection efficiency, high charged track reconstruction efficiency and good momentum resolution.

Measurements of the resonance parameters of the $\psi(3770)$ are summarized in Table 1.I. The agreement between measured values of the production cross section are not consistent. Thus, while the presence of the $\psi(3770)$ in the e^+e^- annihilation cross section provides the possibility of extracting D meson branching ratios from $\sigma \cdot B$ measurements at the peak of the $\psi(3770)$ (on the assumption that the $\psi(3770)$ decays solely to $D\bar{D}$ pairs), it has not been possible to do this in a reliable manner. The Mark III has recently made absolute measurements of D meson branching ratios by a double tag method, which is independent of the $\psi(3770)$ resonance parameters[5,43]. Using these branching ratios together with the Mark III $\sigma \cdot B$ measurements, one obtains a value of $\sigma(\psi(3770)) = 5.0 \pm 0.5\ nb$, smaller than the average of $8.0 \pm 0.7\ nb$ obtained from direct measurements.

These comparisons suggest that there are problems either with experiments or with the assumptions regarding the decay properties of the $\psi(3770)$. The Mark III value of $\sigma(\psi(3770))$ is based on the assumption that $D\bar{D}$ decay is 100% . The most direct way to test this assumption is to search for non-$D\bar{D}$ decays of the $\psi(3770)$.

1.2 THE QCD LAGRANGIAN

As in any other theory, we would like to find some fundamental rules that guide the strong interaction between quark and antiquark.

In QED, the Lagrangian takes the form:

$$L = \bar{\psi}(i\gamma^\mu \partial_\mu - m)\psi + e\bar{\psi}\gamma^\mu A_\mu \psi - \frac{1}{4}F_{\mu\nu}F^{\mu\nu}, \tag{1.1}$$

where, ψ is the fermion field, A_μ is the vector potential, and

$$F_{\mu\nu} = \partial_\mu A_\nu - \partial_\nu A_\mu \tag{1.2}$$

is the field strength tensor.

Now, in QCD, in an analogous way, the Lagrangian takes the form:

$$L = \bar{q}(i\gamma^\mu \partial_\mu - m)q - g\bar{q}\gamma^\mu A_\mu q - \frac{1}{4}G^a_{\mu\nu}G^{\mu\nu}_a. \tag{1.3}$$

It is a little different from QED because of the SU(3) color symmetry. In Eq. 1.3, the quark field q has three colors R, G, B and is therefore a vector:

$$q = \begin{pmatrix} q_R \\ q_G \\ q_B \end{pmatrix}. \tag{1.4}$$

The vector potential A_μ is given by:

$$A_\mu = T_a G^a_\mu, \tag{1.5}$$

where G^a_μ is the gluon field; $a = 1...8$ is an eightfold color index; T_a are SU(3)

generators. The field strength tensor is given by:

$$G^a_{\mu\nu} = \partial_\mu G^a_\nu - \partial_\nu G^a_\mu - g f_{abc} G^b_\mu G^c_\nu. \tag{1.6}$$

Because of the different vector gauge field A_μ in QCD, the interactions are quite different from those in QED. One of the typical examples is the running coupling constant of the perturbation theory because of the additional gluon–gluon coupling. It gives asymptotic freedom at short distances and approaches unity at large distances, causing the perturbation theory to fail.

In principle, we could calculate all decay processes shown in Fig. 1.4.1, Fig. 1.4.2, Fig. 1.5.1, Fig. 1.6.1, and Fig. 1.7.1 by using the Lagrangian of QED (Eq. 1.1) and QCD (Eq. 1.3). However, in reality we cannot, as the coupling constant $\alpha_s(q^2)$ at $q^2 \sim 1.5 - 2$ GeV^2/c^4 places us in a non–perturbative region.

1.3 $^3S_1 - ^3D_1$ MIXING

The physical $\psi(3685)$ and the $\psi(3770)$ are not pure S wave or pure D wave. Rather, they are linear combinations of the pure S wave and the pure D wave. From the quark currents[14,15]

$$j^a_\mu(q) = \bar{c}\frac{\lambda^a}{2}\{f(q^2)\gamma_\mu - \frac{g(q^2)}{2m}\sigma_{\mu\nu}q_\nu\}c, \tag{1.7}$$

and the definition

$$\kappa = 1 + g(q^2)/f(q^2), \tag{1.8}$$

the interaction tensor responsible for the mixing is:[15]

$$V_T = \frac{\kappa^2}{6m^2}(\vec{S}^2 - 3(\vec{S}\cdot\vec{n})(\vec{S}\cdot\vec{n}))(V''(r) - V'(r)/r). \tag{1.9}$$

The matrix element between 2^3S_1 and 1^3D_1,

$$\langle 1^3D_1|V_T|2^3S_1\rangle = \frac{\sqrt{2}\kappa^2}{6m^2}\int_0^\infty R_{1D}(r)(V'' - V'/r)R_{2S}(r)r^2dr, \tag{1.10}$$

may not be zero. Where R_{nl} are the radial part of the wave functions with

energy level n and orbit angular momentum l. Therefore, from the first–order perturbation theory, two eigenstates of the Hamiltonian are:

$$\begin{pmatrix} \psi(3685) \\ \psi(3770) \end{pmatrix} = \begin{pmatrix} 1 & -\epsilon \\ \epsilon & 1 \end{pmatrix} \begin{pmatrix} 2^3S_1 \\ 1^3D_1 \end{pmatrix} \tag{1.11}$$

or approximately,

$$\begin{pmatrix} \psi(3685) \\ \psi(3770) \end{pmatrix} = \begin{pmatrix} \cos\theta & -\sin\theta \\ \sin\theta & \cos\theta \end{pmatrix} \begin{pmatrix} 2^3S_1 \\ 1^3D_1 \end{pmatrix}, \tag{1.12}$$

with

$$\sin\theta = \epsilon = \frac{\langle 1^3D_1|V_T|2^3S_1\rangle}{M(1^3D_1) - M(2^3S_1)}. \tag{1.13}$$

For a simple harmonic oscillator potential $V(r) = ar^2$, it is clear that $(V'' - V'/r) = 0$, and therefore no mixing could take place because of the tensor interaction. For the potential of the form $V(r) = -a/r + br + V_0$, the mixing is about 4% or the mixing angle θ is about $\sim 2^o$. [15]

The wave functions of the $\psi(3685)$ and $\psi(3770)$ are also coupled to the $|D\bar{D}\rangle$ and $|D^*\bar{D}^*\rangle$....:

$$\begin{aligned} |\psi(3685)\rangle = &\sum_n a_n|n^3S_1(c\bar{c})\rangle + b_n|n^3D_1(c\bar{c})\rangle \\ &+ \alpha|D\bar{D}; p-wave\rangle + \beta|D^*\bar{D}^*; f-wave\rangle + ... \end{aligned} \tag{1.14}$$

$$\begin{aligned} |\psi(3770)\rangle = &\sum_n a_n'|n^3S_1(c\bar{c})\rangle + b_n'|n^3D_1(c\bar{c})\rangle \\ &+ \alpha'|D\bar{D}; p-wave\rangle + \beta'|D^*\bar{D}^*; f-wave\rangle + ... \quad . \end{aligned} \tag{1.15}$$

This coupling introduces a mixing of 17%, which is much larger than the mixing that is due to the tensor interaction (Eq. 1.13)[21].

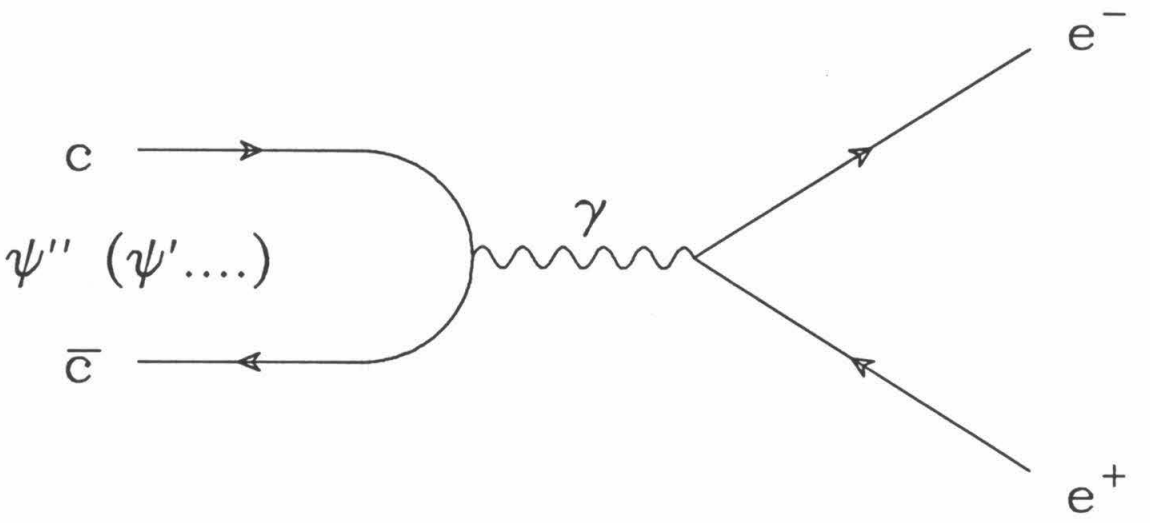

Figure 1.3.1: $c\bar{c}$ annihilating into two electrons.

That mixing between S and D wave is indeed taking place has been supported by experimental measurements on the electronic width of the $\psi(3770)$. The annihilation of the $c\bar{c}$ states into lepton pairs is shown in Fig. 1.3.1. The leptonic decay rates of the n^3S_1 states are given by[12]:

$$\begin{aligned}\Gamma(n^3S_1 \to l^+l^-) &= 16\pi\alpha^2 Q_c^2 \frac{|\psi_n(0)|^2}{M^2}\left(1+\frac{2m_l^2}{M^2}\right)\left(1-\frac{4m_l^2}{M^2}\right)^{\frac{1}{2}} \\ &\simeq 16\pi\alpha^2 Q_c^2 \frac{|\psi_n(0)|^2}{M^2}.\end{aligned} \tag{1.16}$$

The experimental results in Fig. 1.3.2 show that the $\psi(3770)$ is not a n^3S_1 state; the electronic width of the $\psi(3770)$ is much smaller than that for neighboring states. On the other hand, the electronic width of the $^3D_1$ based on the non-relativistic charmonium model is given by:[15]

$$\Gamma(^3D_1 \to e^+e^-) = \frac{200}{M^6}\alpha^2 Q_c^2 |R_D''(0)|^2. \tag{1.17}$$

The numerical estimate is 120 eV, which is less than half the experimental meas-

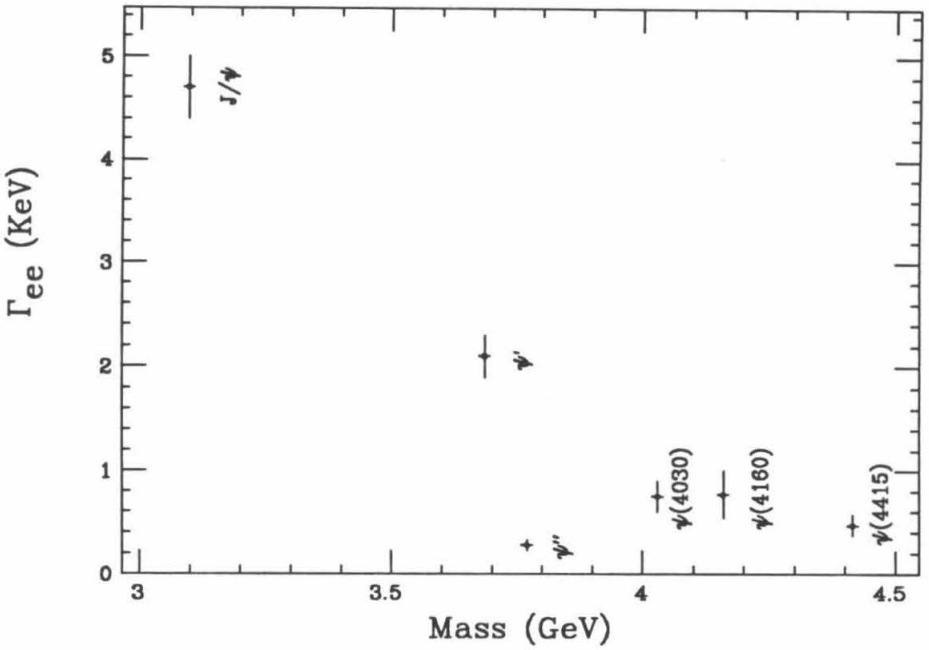

Figure 1.3.2: Electron partial widths of the $c\bar{c}$ resonances.

urement of 276±40 eV [37]. Thus, the $\psi(3770)$ cannot be a pure D wave. It can therefore be concluded that mixing of the 2^3S_1 and 1^3D_1 is indeed taking place.

Due to the existence of mixing, some characteristics of $\psi(3770)$ decays will be different from those of a pure $^3S_1$ or a pure $^3D_1$ state. The details will be discussed in the following sections.

1.4 Annihilation of the $\psi(3770)$

The annihilation processes contributing to the decays of the $\psi(3770)$ are shown in Fig. 1.4.1 and Fig. 1.4.2. At least three gluons or two gluons plus one photon are required in each process. The $c\bar{c}$ must annihilate into at least two gluons to conserve color. The processes must also conserve charge conjugation. Two gluons can only have one charge conjugation eigenstate with eigenvalue $+1$, while three gluons can have two eigenstates with eigenvalues ± 1. Therefore for the annihilation of the $\psi(3770)$, at least three gluons or two gluons plus one photon are required to conserve both color and charge conjugation.

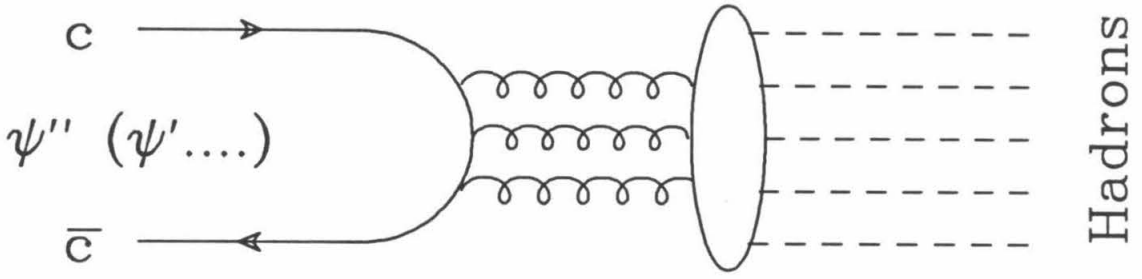

Figure 1.4.1: Three–gluon annihilation of the $c\bar{c}$.

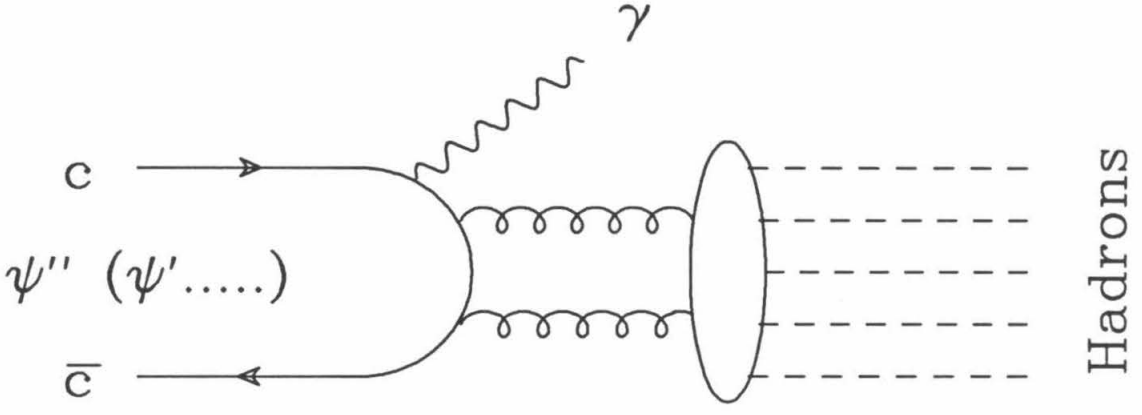

Figure 1.4.2: $c\bar{c}$ annihilating into one photon and two gluons.

From Eq. 1.12:

$$|\psi(3770)\rangle = \cos\theta|1^3D_1\rangle + \sin\theta|2^3S_1\rangle. \tag{1.18}$$

Thus, the amplitude for three–gluon annihilation is:

$$\langle 3g|V_{interaction}|\psi(3770)\rangle = \cos\theta\langle 3g|V_{interaction}|1^3D_1\rangle + \sin\theta\langle 3g|V_{interaction}|2^3S_1\rangle. \tag{1.19}$$

The three–gluon annihilation of quarkonium is very similar to the three–photon annihilation of positronium. In the lowest order QCD calculation, the 3–gluon coupling does not play a role. Therefore, the last term in the Lagrangian of QCD (Eq. 1.3) is neglected, making the QCD and QED calculations almost identical. The calculation of the positronium $^3S_1$ state had been performed in 1949[9,10], and the three–photon annihilation rate of the $c\bar{c}$ is obtained by multiplying by a factor of $3Q_c^6$. The factor 3 comes from a quark's having three colors and $Q_c = 2/3$ is the charge of the charm quark in a unit of electron charge. The rate becomes:

$$\Gamma(n^3S_1 \to 3\gamma) = \frac{2^{10}}{3^7\pi}(\pi^2 - 9)\frac{\alpha^3}{M^2}|R_{n,S}(0)|^2. \tag{1.20}$$

The ratios of the decay rates for gluons and photons can be calculated by the comparison of the interacting vertex. For three gluons and three photons, this ratio is:

$$\frac{\Gamma_{3g}}{\Gamma_{3\gamma}} = \frac{\alpha_s^3}{9\alpha^3Q_c^6}\sum_{a,b,c}|Tr(\frac{\lambda_a}{2}\{\frac{\lambda_b}{2},\frac{\lambda_c}{2}\})|^2 = (\frac{\alpha_s}{\alpha})^3(\frac{5\cdot 3^3}{2^7}). \tag{1.21}$$

For two gluons plus one photon and three photons, this ratio is:

$$\frac{\Gamma_{1\gamma 2g}}{\Gamma_{3\gamma}} = \frac{3(\sqrt{\alpha}Q_c)^2\frac{1}{3}\alpha_s^2\sum_{a,b}\left(Tr(\frac{\lambda_a}{2}\frac{\lambda_b}{2})\right)^2}{3\alpha^3Q_c^6} = (\frac{\alpha_s}{\alpha})^2(\frac{3}{2})^3. \tag{1.22}$$

Using Eq. 1.20 and Eq. 1.21, we can find the annihilation rate of the n^3S_1 charmonium into three gluons:

$$\Gamma(n^3S_1 \to 3g) = \frac{40}{81\pi}(\pi^2 - 9)\frac{\alpha_s^3}{M^2}|R_{n,S}(0)|^2. \tag{1.23}$$

Using Eq. 1.20 and Eq. 1.22, the annihilation rate of two gluons plus one photon

is:

$$\Gamma(n^3S_1 \to \gamma 2g) = \frac{128}{81\pi}(\pi^2 - 9)\frac{\alpha\alpha_s^2}{M^2}|R_{n,S}(0)|^2. \tag{1.24}$$

The three–photon and three-gluon annihilation rates of the D wave can also be calculated by using the QED method and Eq. 1.21.[11] The three–photon annihilation rate is:

$$\Gamma(1^3D_1 \to 3\gamma) = 3Q_c^6\frac{304}{9\pi}\frac{\alpha^3|R''_{1,D}(0)|^2}{m_c^6}ln\frac{m_c}{\omega_{3,min}}; \tag{1.25}$$

and the three–gluon annihilation rate is:

$$\Gamma(1^3D_1 \to 3g) = \frac{48640}{81\pi}\frac{\alpha_s^3|R''_{1,D}(0)|^2}{M^6}ln\frac{M}{\Delta}, \tag{1.26}$$

where the bound-state mass is approximated by $M \simeq 2m_c$ and the cutoff mass by $\Delta = 2\omega_{3,min} = \frac{2}{\langle r\rangle} \sim 1\ GeV$.[15]

The one-photon, two-gluon annihilation rate of the D wave can be calculated using Eq. 1.22 and Eq. 1.25:

$$\begin{aligned}\Gamma(^3D_1 \to \gamma 2g) &= \frac{\Gamma_{1\gamma 2g}}{\Gamma_{3\gamma}}\Gamma(^3D_1 \to 3\gamma) \\ &= (\frac{\alpha_s}{\alpha})^2(\frac{3}{2})^3\frac{57\times 2^{16}}{3^8\pi}\frac{\alpha^3|R''_{n,D}(0)|^2}{M^6}ln\frac{M}{\Delta} \\ &= \frac{19\cdot 2^{13}}{3^4\pi}\frac{\alpha\alpha_s^2|R''_{n,D}(0)|^2}{M^6}ln\frac{M}{\Delta}.\end{aligned} \tag{1.27}$$

These predictions are to lowest order in α_s. For higher orders in α_s, the decay rates are: $\Gamma = \Gamma_0[1 + B\alpha_s + O(\alpha_s^2)]$, where Γ_0 is from the lowest order α_s calculation and B is a constant. Some predictions based on higher order α_s calculations may be found in Ref.(34). According to Ref.(34), the sign of the B for gluon annihilation is positive for $^1S_0$, negative for $^3S_1$, and not known for $^3D_1$.

The three–gluon annihilation rates in lowest order can be estimated numerically using Eq. 1.23 and Eq. 1.26. Since these estimations do not include higher order α_s correction, large errors are expected when compared with experimental results. Using $|R_{1,S}(0)| = 0.67$ and[2] $\Gamma(J/\psi \to 3g) = 43$ keV as input[15], we obtain $\alpha_s = 0.19$. Using this α_s, $R_{2,S}(0)/R_{1,S}(0) = \sqrt{3/2}$, $|R''_{1,D}(0)| = 0.28$ and [15] $\Delta \simeq 1.$, the three–gluon annihilation rates are predicted to be $\Gamma(2^3S_1 \to 3g) = 46$ keV and $\Gamma(1^3D_1 \to 3g) = 44$ keV.

Following Eq. 1.16 and Eq. 1.17, the electronic widths of the S and D components in terms of radial wave functions are:

$$\Gamma(2^3S_1 \to e^+e^-) = 4\alpha^2 Q_c^2 \frac{|R_{2,S}(0)|^2}{M^2}, \tag{1.28}$$

$$\Gamma(1^3D_1 \to e^+e^-) = 200\alpha^2 Q_c^2 \frac{|R''_{1,D}(0)|^2}{M^6}. \tag{1.29}$$

The three–gluon annihilation widths of the S and D waves can also be calculated without an explicit model for the wave functions. The ratios of three-gluon and electronic widths for S and D wave components, following Eq. 1.23, Eq. 1.26, Eq. 1.28 and Eq. 1.29, are:

$$R_S^2 = \frac{\Gamma(^3S_1 \to 3g)}{\Gamma(^3S_1 \to e^+e^-)} = \frac{\alpha_s^3}{\alpha^2}\frac{5}{18\pi}(\pi^2 - 9), \tag{1.30}$$

$$R_D^2 = \frac{\Gamma(^3D_1 \to 3g)}{\Gamma(^3D_1 \to e^+e^-)} = \frac{\alpha_s^3}{\alpha^2}\frac{304}{45\pi} ln(\frac{M}{\Delta}). \tag{1.31}$$

Therefore, the three–gluon annihilation rate of the $\psi(3770)$ can be calculated based on the electronic widths of the $\psi(3685)$, $\psi(3770)$ and the mixing angle:

$$\begin{pmatrix} \sqrt{\Gamma(\psi(3685) \to 3g)} \\ \sqrt{\Gamma(\psi(3770) \to 3g)} \end{pmatrix}$$
$$= \begin{pmatrix} R_S cos^2\theta + R_D sin^2\theta & \cos\theta \sin\theta (R_S - R_D) \\ \cos\theta \sin\theta (R_S - R_D) & R_D cos^2\theta + R_S sin^2\theta \end{pmatrix} \begin{pmatrix} \sqrt{\Gamma(\psi(3685) \to e^+e^-)} \\ \sqrt{\Gamma(\psi(3770) \to e^+e^-)} \end{pmatrix}. \tag{1.32}$$

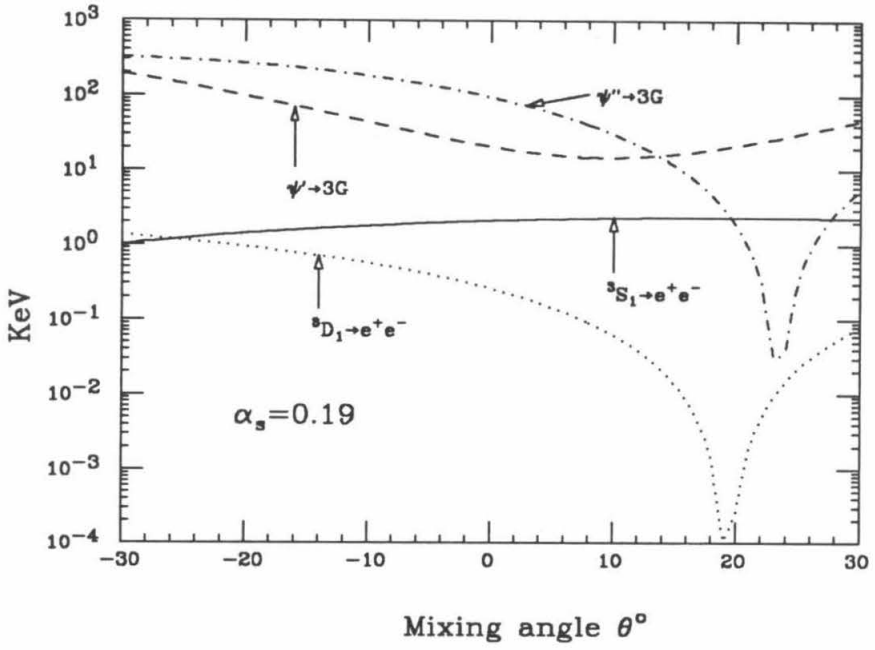

Figure 1.4.3: Predicted three–gluon annihilation widths. The predictions are based on the electron widths as functions of the mixing angles.

The electronic widths of the S, D wave components and the three-gluon annihilation widths of the $\psi(3685)$ and $\psi(3770)$ as functions of the mixing angles are summarized in Fig. 1.4.3. Both R_S and R_D are assumed to be positive. The region in the neighborhood of $\theta = 6.5^o$ is the physically interesting one. At this mixing angle, $\Gamma(^3D_1 \to e^+e^-) = 120\text{eV}$, $\Gamma(\psi(3685) \to 3g) = 16$ keV, and $\Gamma(\psi(3770) \to 3g) = 50$ keV

1.5 Hadronic transitions of the $\psi(3770)$

The hadronic transition processes, illustrated in Fig. 1.5.1, are particularly interesting. In these processes, the $Q\bar{Q}$ in the higher energy states radiate gluons, making a transition to a lower energy state, where gluons converted into hadrons[26,27], in analogy to nuclear transitions. We certainly would like know more about these transitions, just as we have learned a great deal about nuclear transitions. The most interesting finding is the possibility of fixing the matrix

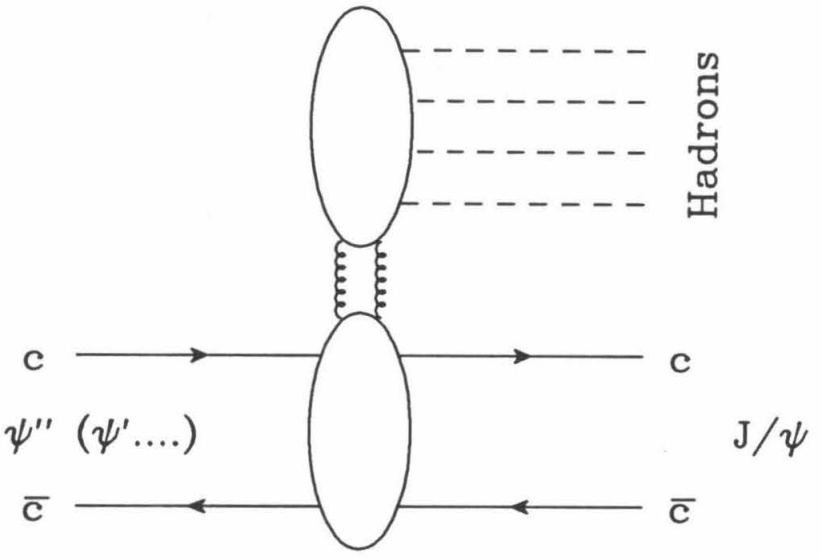

Figure 1.5.1: Hadronic transition in the $c\bar{c}$ system.

element $\langle \pi^+\pi^- | E_k O E_l | 0 \rangle$, which describes how gluons are converted into pions starting from first principles.[30]

Since quarks and gluons carry color charges, interactions between gluons and gluons, or between gluons and quarks can occur. The hadronic transitions in quarkonium are therefore very difficult to predict. The simplest case is that in which quarkonium is made of heavy quarks (charm or heavier), where $ka \leq 1$ is satisfied by the transitions between states, $k \sim \frac{1}{2}(\Phi_{initial} - \Phi_{final})$ and a is the size of the quarkonium. With this restriction, the predictions for the transitions can be made by the multipole expansion method[16,24,27,28].

Let us briefly review the multipole expansion method, following Yan.[16]

Beginning from the gauge-invariant effective Lagrangian:

$$\begin{aligned} L_Q = & \int d^3x \{ \bar{\psi}[i\gamma^\mu \partial_\mu - m]\psi - g\bar{\psi}\gamma^\mu A_\mu \psi \} \\ & - \frac{1}{2}\frac{g^2}{4\pi} \sum_a \int d^3x d^3y \rho_a(\vec{x},t) \frac{1}{|\vec{x}-\vec{y}|} \rho_a(\vec{y},t) \end{aligned} \tag{1.33}$$

with color charge density

$$\rho_a(\vec{x},t) = \Psi^\dagger(\vec{x},t)T_a\Psi(\vec{x},t), \tag{1.34}$$

where the quarks are represented by

$$\Psi = U^{-1}(\vec{x},t)\psi, \tag{1.35}$$

with

$$U(\vec{x},t) = Pexp\Big(ig\int_0^{\vec{x}} d\vec{x}'\cdot\vec{A}(\vec{x},t)\Big), \tag{1.36}$$

Yan showed that

$$\begin{aligned} L_Q = &\int d^3x\{\Psi^\dagger[i\gamma^\mu\partial_\mu - m]\Psi - g\Psi^\dagger\gamma^\mu A'_\mu\Psi\} \\ &- \frac{1}{2}\frac{g^2}{4\pi}\sum_a\int d^3xd^3y\rho_a(\vec{x},t)\frac{1}{|\vec{x}-\vec{y}|}\rho_a(\vec{y},t), \end{aligned} \tag{1.37}$$

where

$$A' = U^{-1}A_\mu U - \frac{i}{g}U^{-1}\partial_\mu U. \tag{1.38}$$

The term responsible for gluon radiation is:

$$L_I = -g\int d^3x\Psi^\dagger\gamma^\mu A'_\mu\Psi. \tag{1.39}$$

Now, $A'_\mu(\vec{x},t)$ can be written as[46]:

$$A'_0(\vec{x},t) = A_0(0,t) - \int_0^1 dsU^{-1}(s\vec{x},t)\vec{x}\cdot\vec{E}(s\vec{x},t)U(s\vec{x},t) \tag{1.40}$$

$$\vec{A}'(\vec{x},t) = -\int_0^1 dss U^{-1}(s\vec{x},t)\vec{x} \times \vec{B}(s\vec{x},t)U(s\vec{x},t), \tag{1.41}$$

where

$$E_k = T_a G^a_{k0}, \tag{1.42}$$

$$B_i = -T^a \epsilon_{ijk} G^{jk}_a, \tag{1.43}$$

and $G_{\mu\nu}$ is the field strength tensor defined in Eq. 1.6. Expanding A'_μ in powers of $\vec{x}$ and using Eq. 1.40, Eq. 1.41, the QCD multipole expansion is:

$$\begin{aligned} L_I &= -\int d^3x (g\Psi^\dagger \gamma^\mu A'_\mu \Psi) \\ &= \sum_a [-Q_a A_{0a}(0,t) + \vec{d}\cdot\vec{E}_a(0,t) + \vec{m}_a \cdot \vec{B}_a(0,t) + \ldots], \end{aligned} \tag{1.44}$$

where

$$Q_a = g\int d^3r \rho_a(\vec{r},t) \tag{1.45}$$

$$\vec{d}_a = g\int d^3r \vec{r}\rho_a(\vec{r},t) \tag{1.46}$$

$$\vec{m}_a = g\int d^3r \frac{1}{2}\vec{r}\times\vec{j}_a(\vec{r},t), \tag{1.47}$$

and

$$\vec{j}_a = \Psi\vec{\gamma}T_a\Psi. \tag{1.48}$$

In Hamiltonian form, the expansion can be written as:

$$H_I = Q_a A_{0a}(0,t) - \vec{d}_a\cdot\vec{E}_a(0,t) - \vec{m}_a\cdot\vec{B}_a(0,t) + \ldots, \tag{1.49}$$

where

$$Q_a = g(T_a + \bar{T}_a) \tag{1.50}$$

$$\vec{d}_a = \frac{1}{2} g \vec{x} (T_a - \bar{T}_a) \tag{1.51}$$

$$\vec{m}_a = \frac{g}{4m} (T_a - \bar{T}_a)(\vec{\sigma} - \vec{\sigma}'). \tag{1.52}$$

By analogy with the conventional QED multipole expansion, the first three terms are called monopole, electric dipole and magnetic dipole. The monopole term annihilates a color singlet; the hadronic transitions are caused by the other terms in H_I.

One immediate prediction of the multipole expansion formalism is the ratio of the rates for electric dipole and magnetic dipole transitions. The ratio of these rates is given by

$$\frac{\Gamma_{electric\ dipole}}{\Gamma_{magnetic\ dipole}} \sim (am)^2, \tag{1.53}$$

where a is the size of the quarkonium system and m is the mass of the quark. For the charmonium system, this ratio is about 20, compared with the experimental value of 19±3 at the $\psi(3685)$.

Another important prediction is the mass distribution of the two pions produced in the transitions. Incorporating PCAC (Partial Conservation of Axial-vector Current) into the multipole expansion method, Yan predicted the mass distribution of the two pions. Two particular cases are interesting here. The first is for the transition $l_f = l_i = 0$ or $J_f = J_i = 0$, while the second is for $l_f \neq l_i$ or $J_f \neq J_i$. Here, i and f denote the initial and final state, l and J represent orbital angular momentum and total angular momentum, respectively. For the $\psi(3770)$, we are interested in both cases because of the mixing of the S and D

wave states. The prediction for $2^3S_1 \rightarrow 1^3S_1 + \pi^+\pi^-$ is:

$$\frac{d\Gamma_0(2^3S_1 \rightarrow 1^3S_1 + \pi^+\pi^-)}{dM_{\pi\pi}} = K(M_{\pi\pi}^2 - 4m_\pi^2)^{1/2}(M_{\pi\pi}^2 - 2m_\pi^2)^2, \qquad (1.54)$$

where

$$K = \frac{1}{2M_i}[(M_i + M_f)^2 - M_{\pi\pi}^2]^{1/2}[(M_i - M_f)^2 - M_{\pi\pi}^2]^{1/2}. \qquad (1.55)$$

The prediction for $1^3D_1 \rightarrow 1^3S_1 + \pi^+\pi^-$ is:

$$\frac{d\Gamma_2(1^3D_1 \rightarrow 1^3S_1 + \pi^+\pi^-)}{dM_{\pi\pi}} = K(M_{\pi\pi}^2 - 4m_\pi^2)^{1/2}[(M_{\pi\pi}^2 - 4m_\pi^2)^2 \left(1 + \frac{2}{3}\frac{K^2}{M_{\pi\pi}^2}\right) + \frac{8}{15}\frac{K^4}{M_{\pi\pi}^4}(M_{\pi\pi}^4 + 2M_{\pi\pi}^2 m_\pi^2 + 6m_\pi^4)]. \qquad (1.56)$$

The angular distribution of the pion system with respect to the beam axis is also predicted for $1^3D_1 \rightarrow 1^3S_1 + \pi^+\pi^-$:

$$\begin{aligned}\frac{d\Gamma(1^3D_1 \rightarrow 1^3S_1 + 2\pi)}{dM_{\pi\pi}d\cos\theta} =& K(M_{\pi\pi}^2 - 4m_\pi^2)^{1/2}\{(M_{\pi\pi}^2 - 4m_\pi^2)^2\left(1 + \frac{47}{60}\frac{K^2}{M_{\pi\pi}^2}\right) \\ &+ \frac{2}{3}\frac{K^4}{M_{\pi\pi}^2}(M_{\pi\pi}^4 + 2m_\pi^2 M_{\pi\pi}^2 + 6m_\pi^4) \\ &- [\frac{7}{20}\frac{K^2}{M_{\pi\pi}^2}(M_{\pi\pi}^2 - 4m_\pi^2)^2 \\ &+ \frac{2}{5}\frac{K^4}{M_{\pi\pi}^4}(M_{\pi\pi}^4 + 2m_\pi^2 M_{\pi\pi}^2 + 6m_\pi^4)]\cos^2\theta\}.\end{aligned} \qquad (1.57)$$

Following Eq. 1.49, the electric dipole transition matrix element can be written as[16,17,24,29]:

$$M_{E1} = g^2\langle f|x_k G x_l|i\rangle\langle h|E_k O E_l|0\rangle, \qquad (1.58)$$

where G represents the intermediate states, and $E_k O E_l$ are the operators that produce hadrons h from the vacuum.

Kuang and Yan proposed that these intermediate states are the excited states of a vibrational string.[17] Therefore, the transition matrix element can be written as:

$$M_{E1} = i\frac{g^2}{6}\langle f|x_i G(e_i) x_l|i\rangle\langle h|E_k P E_l|0\rangle, \tag{1.59}$$

where

$$G(e_i) = \sum_{kl} \frac{|v,kl\rangle\langle v,kl|}{e_i - e_{v,kl}};$$

$|i\rangle$ and $|f\rangle$ represent the initial state and final states of quarkonium; e_i is the energy of the initial state; P is the projection operator for the sector of the lowest string excitation; $|v,kl\rangle$ are the intermediate states of the string of energy $e_{v,kl}$ and angular momentum l.

With this model for the intermediate states, the transition rates of the different wave components are predicted[17]:

$$\Gamma(2^3S_1 \to 1^3S_1 + \pi^+\pi^-) = G|c_1|^2|f^1_{S,if}|^2 \tag{1.60}$$

$$\Gamma(1^3D_1 \to 1^3S_1 + \pi^+\pi^-) = \frac{4}{15}H|c_2|^2|f^1_{D,if}|^2, \tag{1.61}$$

where

$$f^1_{L,if} = \sum_k \frac{1}{M_i - M_{k1}}\Big[\int dr\ r^3 R_f(r) R^v_{k1}(r)\Big]\Big[\int dr'\ r'^3 R^v_{k1}(r') R_i(r')\Big]; \tag{1.62}$$

$$G = \frac{3M_f}{2M_i}\pi^3 \int dM_{\pi\pi} \frac{d\Gamma_0(2^3S_1 \to 1^3S_1 + \pi^+\pi^-)}{dM_{\pi\pi}} \tag{1.63}$$

and $d\Gamma_0/dM_{\pi^+\pi^-}$ is defined by Eq. 1.54;

$$H = \frac{M_f}{10M_i}\pi^3 \int dM_{\pi\pi} \frac{d\Gamma_2(1^3D_1 \to 1^3S_1 + \pi^+\pi^-)}{dM_{\pi\pi}}, \tag{1.64}$$

and $d\Gamma_2/dM_{\pi^+\pi^-}$ is defined by Eq. 1.56; c_1 and c_2 are constants; $R_i(r)$, $R_f(r)$, $R^v_{k1}(r)$ and M_i, M_f, M_{kl} are the radial wave functions and masses of the initial, final, and intermediate states, respectively.

The constant c_1 is determined from the decay rate of the $\psi(3685)$. The relationship of c_1 and c_2 is determined from the two-gluon calculation; $|c_2| = 3|c_1|$.[17] The wave functions R^v_{k1} of the intermediate states are model–dependent, but numerical calculations show that the ratio of decay rates for S and D waves has a very small dependence on the specific model for the intermediate states.

The ratios of transition rates for the S and D wave components of the $\psi(3685)$ and $\psi(3770)$ from Eq. 1.60 and Eq. 1.61 can be written as:

$$R_H = \frac{\Gamma(2^3S_1 \to 1^3S_1 + \pi^+\pi^-)}{\Gamma(1^3D_1 \to 1^3S_1 + \pi^+\pi^-)} = \frac{G|c_1|^2|f^1_{S,if}|^2}{\frac{4}{15}H|c_2|^2|f^1_{D,if}|^2} \simeq \frac{15G|f^1_{S,if}|^2}{36H|f^1_{D,if}|^2} \simeq 1.0 \quad . \tag{1.65}$$

It can be proven that there is no interference between the S and D waves in this hadronic transition. Thus, using R_H and the mixing angle, the hadronic transition rate of the $\psi(3770)$ is:

$$\begin{aligned}
&\Gamma(\psi(3770) \to J/\psi + \pi^+\pi^-) \\
&\quad = \cos^2\theta\Gamma(1^3D_1 \to 1^3S_1 + \pi^+\pi^-) + \sin^2\theta\Gamma(2^3S_1 \to 1^3S_1 + \pi^+\pi^-) \\
&\quad = \Gamma(\psi(3685) \to J/\psi + \pi^+\pi^-)\Big(\frac{\cos^2\theta + R_H\sin^2\theta}{R_H\cos^2\theta + \sin^2\theta}\Big) \\
&\quad \simeq \Gamma(\psi(3685) \to J/\psi + \pi^+\pi^-) = 71\ keV.
\end{aligned} \tag{1.66}$$

There are other predictions of the decay rates that are quite different (see Ref.(25) and Ref.(29)). The major differences of these approaches from the calculation discussed above is in the determination of the factor $\langle h|E_kOE_l|0\rangle$, which converts gluons $E_i = T_aG^a_{i0}$ into hadrons.

Billoire, *et al.* [25] predict $\Gamma^{0+} = 0.73\alpha_s^2$ keV, using the two–gluon intermediate state with $J^P = 0^+$. For $\alpha_s \simeq 1.0$, the width is:

$$\Gamma(1^3D_1 \to 1^3S_1 + \pi^+\pi^-) \sim 0.7\ keV, \tag{1.67}$$

and $R'_H \simeq 100$.

With additional low energy QCD theorems, Moxhay[29] predicts:

$$\Gamma(2^3S_1 \to 1^3S_1 + \pi^+\pi^-) \simeq \frac{\pi |I_{S,S'}|^2 \Delta^7_{S,S'}}{3^9}, \tag{1.68}$$

$$\Gamma(1^3D_1 \to 1^3S_1 + \pi^+\pi^-) \simeq \frac{(\alpha_s \rho^G)^2 |I_{D,S'}|^2 \Delta^7_{D,S'}}{2^4 \cdot 3^5 \cdot 5^2 \pi}, \tag{1.69}$$

where

$$I_{i,f} \simeq G_0 \langle f | r^2 | i \rangle. \tag{1.70}$$

G_0 can be approximated by a constant to be determined from experimental data; $\rho^G \simeq 0.5$; $\alpha_s(J/\psi) \simeq 0.7$; $\Delta_{i,f}$ is the mass difference between the initial state and the final state. The ratio of Eq. 1.68 to Eq. 1.69 is:

$$R''_H \simeq 156 \frac{|I_{S,S'}|^2}{|I_{D,S'}|^2} \simeq 156 \frac{\langle 2^3S_1 | r^2 | 1^3S_1 \rangle^2}{\langle 1^3D_1 | r^2 | 1^3S_1 \rangle^2}. \tag{1.71}$$

A numerical estimate for the $c\bar{c}$ system gives the $R''_H \sim 83$. This corresponds to a decay rate $\Gamma(1^3D_1 \to 1^3S_1 + \pi^+\pi^-) \simeq 0.9$ keV, using $\Gamma(2^3S_1 \to J/\psi + \pi^+\pi^-) \sim \Gamma(\psi(3685) \to J/\psi + \pi^+\pi^-) = 71$ keV.

The predicted hadronic transition rates of $\psi(3770)$ for Billoire, *et al.*[25] and Moxhay[29] calculations as functions of the mixing angle are shown in Fig. 1.5.2.

The predictions of the multipole expansion method and the intermediate string model are consistent with the experimental measurements in the $b\bar{b}$ system[18,19] except for mass distribution of the two pions, which has been only partially successful. For the transition $2^3S_1 \to 1^3S_1 + \pi^+\pi^-$, the predictions are consistent with the experimental results, but this is not true[16] for the transitions $3^3S_1 \to 1^3S_1 + \pi^+\pi^-$ and $3^3S_1 \to 2^3S_1 + \pi^+\pi^-$. The mass distribution of the two pions from the $\psi(3685)$ is also predicted by this calculation; it is consistent with the measurements.

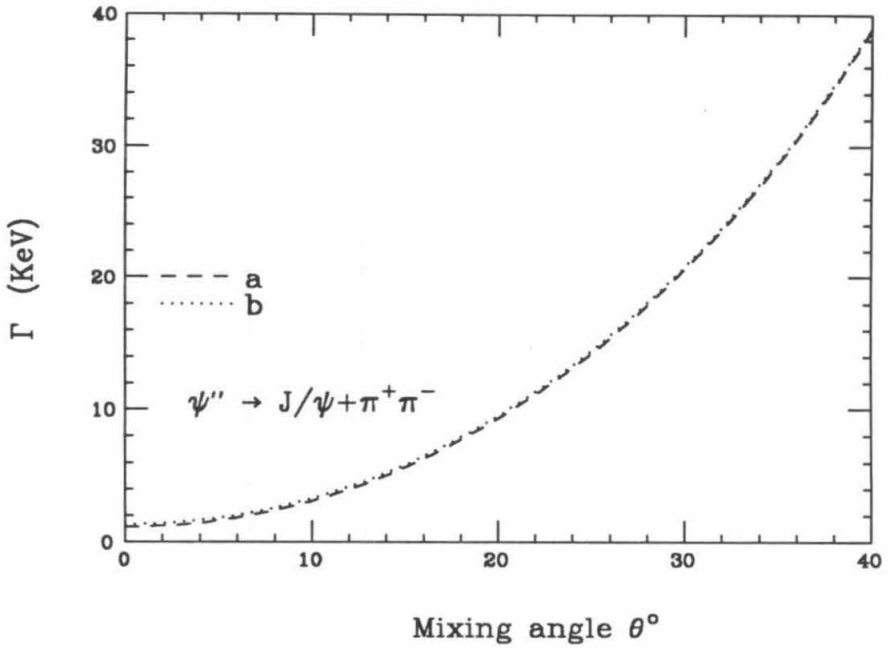

Figure 1.5.2: Predicted hadronic transition widths. *a*). is from Ref. (25), and *b*). is from Ref. (29).

Taking into account the mixing, following Eq. 1.54 and Eq. 1.56, the mass distribution of the two pions for the $\psi(3770)$ transition is:

$$\begin{aligned}&\frac{d\Gamma}{dM_{\pi^+\pi^-}}\\ &=A\cos^2\theta\frac{d\Gamma(1^3D_1\to 1^3S_1+\pi^+\pi^-)}{dM_{\pi^+\pi^-}}+B\sin^2\theta\frac{d\Gamma(^2S_1\to^1 S_1+\pi^+\pi^-)}{dM_{\pi^+\pi^-}},\end{aligned}\tag{1.72}$$

where

$$A=\frac{\Gamma(1^3D_1\to 1^3S_1+\pi^+\pi^-)}{\int dM_{\pi^+\pi^-}\frac{d\Gamma_2(1^3D_1\to 1^3S_1+\pi^+\pi^-)}{dM_{\pi^+\pi^-}}}\tag{1.73}$$

$$B=\frac{\Gamma(2^3S_1\to 1^3S_1+\pi^+\pi^-)}{\int dM_{\pi^+\pi^-}\frac{d\Gamma_0(2^3S_1\to 1^3S_1+\pi^+\pi^-)}{dM_{\pi^+\pi^-}}};\tag{1.74}$$

$d\Gamma_2/dM_{\pi^+\pi^-}$ is defined by Eq. 1.56 and $d\Gamma_0/dM_{\pi^+\pi^-}$ is defined by Eq. 1.54.

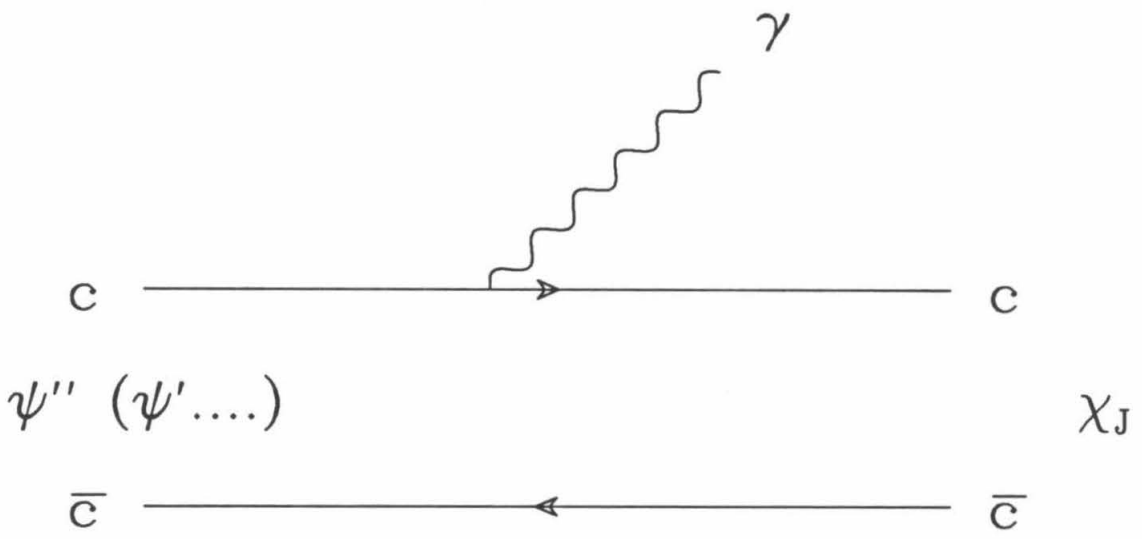

Figure 1.6.1: Electromagnetic transition in the $c\bar{c}$ system.

1.6 Electromagnetic transitions of the $\psi(3770)$

The electromagnetic decay of the $\psi(3685)$ or $\psi(3770)$ is shown in Fig. 1.6.1. This transition is calculable in QED, if the wave functions of the $q\bar{q}$ system are determined.

Two basic approaches are used to predict the transition rate: one is based on the non–relativistic quarkonium model; the other incorporates additional relativistic corrections.

The electromagnetic transition probability is given by:

$$dw = |\langle f|H_{em}|i\rangle|^2 2\pi\delta(E_i - E_f - \omega)\frac{d^3\vec{k}}{(2\pi)^3 2\omega.} \tag{1.75}$$

For the electric dipole transition, this is:[21]

$$\Gamma_{E1} = \frac{4}{27}Q_c^2\alpha\frac{a^2}{(m_c a)^{2/3}}k^3|E_{if}|^2(2J_f+1)S_{if}, \tag{1.76}$$

Decay	Grotch[6] (keV)	Daghighian[22] (keV)	Li[13] (keV)	Yamamoto[31] (keV)[c]	Lane[40] (keV)	Exp. (keV)
$2^3S_1 \to \gamma\chi_0$	23				46	
$2^3S_1 \to \gamma\chi_1$	28				41	
$2^3S_1 \to \gamma\chi_2$	24				29	
$1^3D_1 \to \gamma\chi_0$	204	155[d]		260	301	
$1^3D_1 \to \gamma\chi_1$	324	66.1[d]		82	98	
$1^3D_1 \to \gamma\chi_2$	354	2.9[d]		3.3	3.82	
$\psi(3685) \to \gamma\chi_0$		12			11[a](3.78)[b]	20±4
$\psi(3685) \to \gamma\chi_1$		23	46		22[a](15)[b]	19±4
$\psi(3685) \to \gamma\chi_2$		24			24[a](22)[b]	17±4
$\psi(3770) \to \gamma\chi_0$				0.2-133	371[a](386)[b]	
$\psi(3770) \to \gamma\chi_1$				0.2-57	155[a](175)[b]	
$\psi(3770) \to \gamma\chi_2$				9-21	22[a](33)[b]	

Table 1.II. Predicted electric dipole transition widths. *a*). with mixing angle 15^o and *b*). 21^o; *c*). Predicted with a harmonic oscillator potential. Yamamoto also predicted $\Gamma(\psi(3770) \to \gamma\chi_0) : \Gamma(\psi(3770) \to \gamma\chi_1) : \Gamma(\psi(3770) \to \gamma\chi_2) = 81 : 25 : 1$. *d*). See Ref.(47).

where k is the momentum of the radiated photon, and

$$\begin{aligned} E_{if} =& \frac{3}{2k}\int_0^\infty dr\Big[\Big(1+\frac{k}{4m_c}\Big)u_f(r)[Krj_0(Kr)-j_1(Kr)]u_i(r) \\ &+\frac{k}{4m_c}[J(J+1)-4]u_f(r)u_i(r)j_1(Kr) \\ &+\frac{k}{2m_c}u_f(r)r[\partial u_i(r)/\partial r]j_1(Kr)\Big], \end{aligned} \tag{1.77}$$

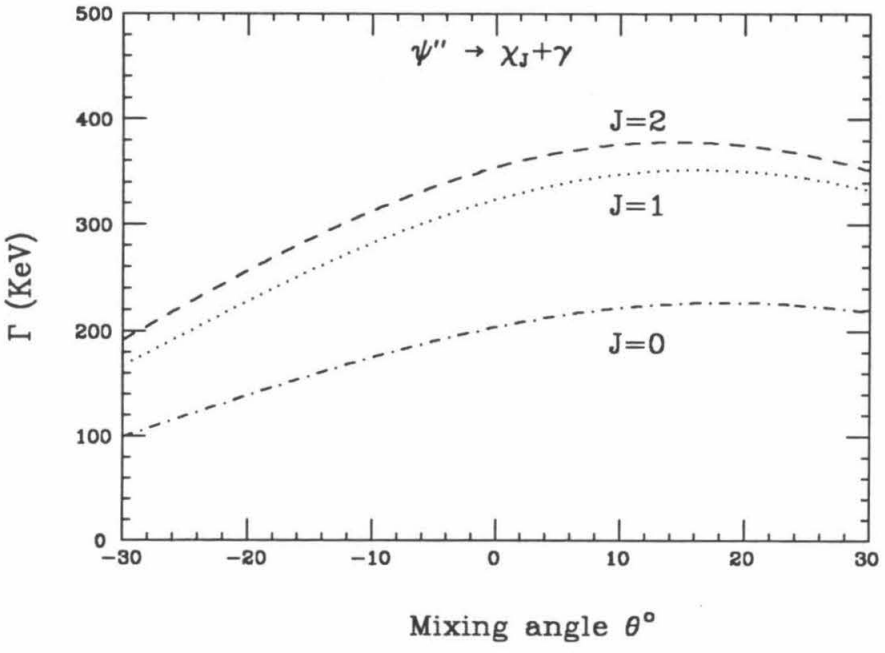

Figure 1.6.2: Predicted electromagnetic transition widths[6].

S_{if} is a statistical factor; $K = \frac{1}{2}ka(m_c a)^{-1/3}$. For the magnetic dipole transition, this is:

$$\Gamma_{M1} = (\frac{Q_q}{2m_q})^2 \alpha k^3 |M_{if}|^2 (2J_f + 1), \tag{1.78}$$

where

$$M_{if} = \int_0^\infty dr u_i(r) u_f(r) j_0(Kr). \tag{1.79}$$

There are large discrepancies between the non–relativistic calculations and the experimental measurements for $\psi(3685) \rightarrow \chi_J + \gamma$. The predictions are a factor of 2 to 4 larger than the experimental measurements.[21]

Two methods are used to resolve these discrepancies. The first is to take into account mixing: the amplitude of S and D waves thus cancel in the $\psi(3685)$ and enhance each other in the $\psi(3770)$.[40] The second employs additional relativistic corrections[6,22].

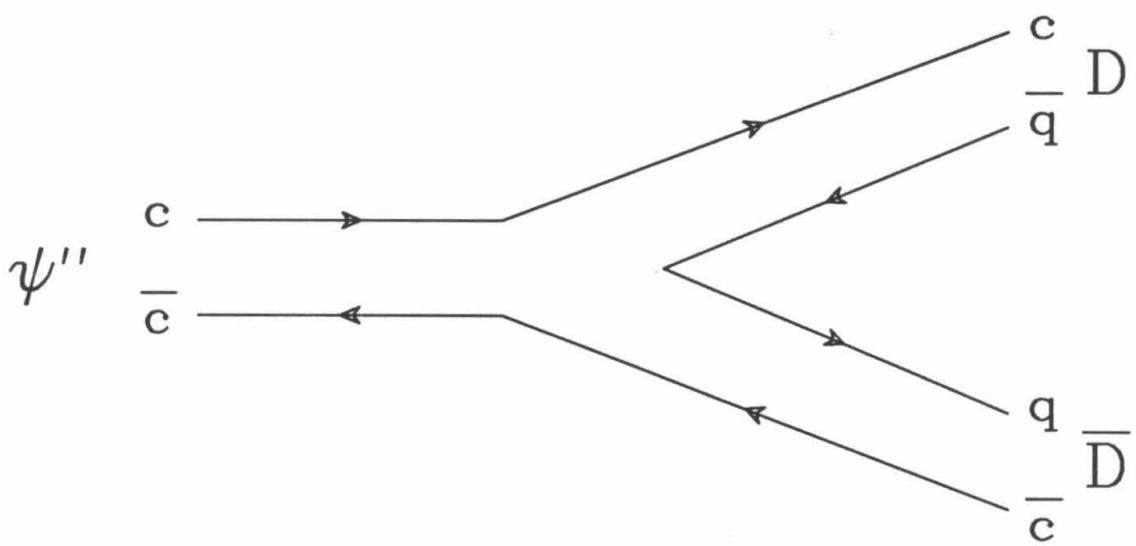

Figure 1.7.1: $\psi(3770)$ decays into two D mesons.

Table 1.II lists the different predictions of electric dipole transition rates for the 2^3S_1, and 1^3D_1, states, as well as for the physical $\psi(3685)$ and $\psi(3770)$.

The most realistic estimates of the $\psi(3770)$ and $\psi(3685)$ electric dipole transition rates employ relativistically corrected transition rates of the S and D wave component and a mixing angle. The correlation of the rates and the mixing angle are shown in Fig. 1.6.2, with predicted S and D component from Ref.(6). The S and D waves are assumed to enhance each other at $\psi(3770)$.

1.7 THE $D\bar{D}$ DECAY OF THE $\psi(3770)$

The $D\bar{D}$ decay of the $\psi(3770)$ is illustrated by Fig. 1.7.1. This process is sometimes referred to as an OZI–allowed [33] decay. "A realistic description of such interactions, rooted in the foundations of QCD, is not yet in sight." [21]

One model used to describe this $D\bar{D}$ decay is the coupled-channel model.[21] This model assumes "that the instantaneous interaction which causes the binding of the $c\bar{c}$ and $q\bar{q}$ states is also responsible for the decay". The interaction

Hamiltonian takes the form:

$$H_I = \frac{3}{8}\sum_{a=1}^{8}\int : \rho_a(\vec{r})V_0(\vec{r}-\vec{r'})\rho_a(\vec{r'}) : d^3r d^3r', \tag{1.80}$$

with the octet color density $\rho_a(\vec{r}) = \psi^\dagger(\vec{r})T_a\psi(\vec{r})$, and quark field ψ. The decay amplitude is:

$$\langle c\bar{c}, \psi(3770)|U|c\bar{q}, \alpha; \bar{c}q, \bar{\beta}; \vec{p}\rangle, \tag{1.81}$$

where α, $\bar{\beta}$ are spin-parities, and $\vec{p}$ is the relative momentum of the D mesons. $U = P_{c\bar{c}}H_I P_{D\bar{D}}$, $P_{c\bar{c}}$ and $P_{D\bar{D}}$ are the projection operators onto $c\bar{c}$ and $c\bar{q}$, $\bar{c}q$ subspaces.

The total width of the $\psi(3770)$ is predicted from the coupled-channel model to be 30 MeV.

Another prediction is based on a "Field-theoretic model of composite hadrons".[32] This model gives the coupling between $\psi(3770)$ and $D\bar{D}$ as:

$$\begin{aligned}&\langle D^+(\vec{p'})D^-(-\vec{p'})|V_{Q^\dagger\bar{Q}}(0)|\psi''_m(0)\rangle \\ &\simeq \frac{1}{8\sqrt{6}}\pi^{-15/4}(R_\psi^2)^{3/4}(R_D^2)^{3/2}\beta^{-3/2}p'_m\alpha_{\psi(3770)}exp(-\frac{R_D^2R_\psi^2}{2\beta}\lambda_1^2\vec{p'}^2),\end{aligned} \tag{1.82}$$

where

$$\begin{aligned}\alpha_{\psi(3770)} =&\Big(\frac{2}{15}\Big)^{1/2}(R_\psi^2/\beta^2)\{5g(b/2-\lambda_2 g) \\ &-\frac{5}{4}(g^2/\beta)[7bg-3\lambda_1(-R_\psi^2+5R_D^2)]+\frac{35}{32}\lambda_1(g^4/\beta^2)(2R_\psi^2-5R_D^2)\}.\end{aligned} \tag{1.83}$$

R_ψ, R_D are the "size" of the J/ψ and D mesons, $\frac{\lambda_1}{\lambda_2} = \frac{m_c}{m_{u(d)}}$, $\lambda_1+\lambda_2 = 1$, $b = \frac{1}{m_{D^+}}$, $\beta = \frac{1}{2}R_\psi^2 + R_D^2$.

With $g = 1.67 GeV^{-1}$, and $R_D^2 = 6 GeV^{-2}$, the $\psi(3770)$ partial width to D meson pairs are predicted to be:

$$\Gamma(\psi(3770) \rightarrow D^+D^-) = 12.1\ MeV \tag{1.84}$$

and

$$\Gamma(\psi(3770) \rightarrow D^0\bar{D}^0) = 16.8\ MeV. \tag{1.85}$$

The sum of above two gives 28.9 MeV. With $R_D^2 = 9 GeV^{-2}$, this width becomes 21.3 MeV. These predictions can be compared with the measurement: $\Gamma_{total}(\psi(3770)) = 25 \pm 3$ MeV^2.

1.8 The Related Topics of The non–$D\bar{D}$ Decays of the $\psi(3770)$

There are several other issues related to the non–$D\bar{D}$ decays of the $\psi(3770)$. One is the rescattering process shown in Fig. 1.8.1. Another is the anomalous vector-peudoscalar decays of the J/ψ and $\psi(3685)$.

The $D\bar{D}$ decays are often called "OZI–allowed decays", as mentioned earlier; annihilation decays and hadronic transitions are often called "OZI–suppressed decays".[33] In previous sections, we have already seen that based on QCD, the OZI–suppressed decays should have much smaller branching ratios compared with the OZI–allowed decays. In the $\psi(3770)$ case, the ratio of the branching ratios of the OZI suppressed to those of the OZI–allowed should be of order of 2×10^{-3}, which is based on predictions in Fig. 1.4.3 and the measured total width of the $\psi(3770)$.

However, the rescattering process as in Fig. 1.8.1 could result in a large branching ratio for the OZI–suppressed decays of the $\psi(3770)$. In this process, each step is OZI–allowed, even though the entire decay is OZI–suppressed. Because of this rescattering, the total OZI–suppressed decay could have a large branching ratio[7].

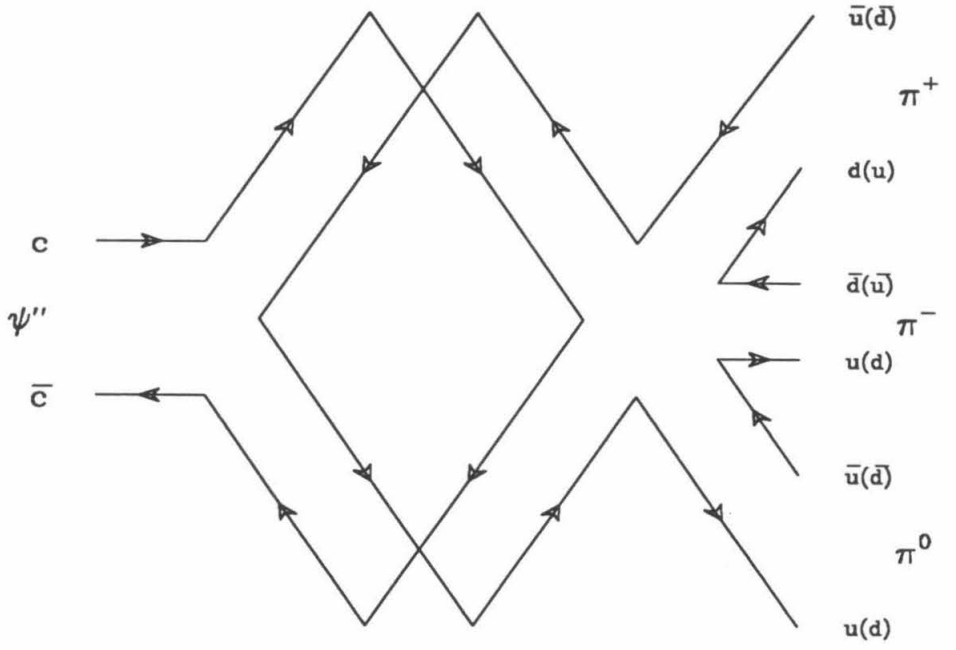

Figure 1.8.1: The rescattering process.

The other issue is related to the ratios of the branching ratios of the vector-peudoscalar decays of the J/ψ and $\psi(3685)$. This ratio is predicted to be[8]:

$$Q = \frac{\Gamma(\psi(3685) \to e^+e^-)\Gamma_{tot}(J/\psi)}{\Gamma(J\psi \to e^+e^-)\Gamma_{tot}(\psi(3685))} = 0.135 \pm 0.023, \tag{1.86}$$

based on perturbative QCD. This prediction agrees very well with experimental results, except for the case of vector–peudoscalar decays. The measured results for the final states $\rho\pi$ and $K^{*\pm}K^{\mp}$ are:

$$Q(\rho\pi) \leq 0.63 \times 10^{-2}. \tag{1.87}$$

$$Q(K^{*\pm}K^{\mp}) \leq 2.03 \times 10^{-2}, \tag{1.88}$$

far below the QCD prediction. A number of explanations have been advanced[23]. Measurements of the OZI–suppressed decays of the $\psi(3770)$ may help us understand more about this unusual behavior.

2. MARK-III EXPERIMENT

2.1 MARK-III HISTORY

Design of the detector started in 1978 using as a shell the flux return steel of Mark I, the original SPEAR magnetic detector. Construction was completed in the spring of 1981 and the detector was installed at SPEAR that summer. Check out started during the fall and the first data were taken in the spring of 1982.

Time	$E_{c.m.}$	Luminosity or Events
1982 Spring	$J/\psi(3097)$	~0.9 M J/ψ produced
1982 Fall	$\psi(3684)$	~150 K hadronic events produced
	$\psi(3770)$	~1800 nb^{-1}
1983 Spring	$J/\psi(3097)$	~1.8 M J/ψ produced
	$\psi(3770)$	~3800 nb^{-1}
1984 Winter	$\psi(3770)$	~3400 nb^{-1}
1985 Spring	$J/\psi(3097)$	~3.1 M J/ψ produced
1986 Winter	4.14 GeV	~6300 nb^{-1}

Table 2.I: Mark–III data taking history.

2.2 OVERVIEW

Physical Layout of the Detector

Axial and side views of the Mark-III detector are shown in Fig. 2.2.1 and Fig. 2.2.2.

The electron and positron beams collide at the center of the detector, inside the Be vacuum beam pipe. Encircling the beam pipe is the inner trigger drift

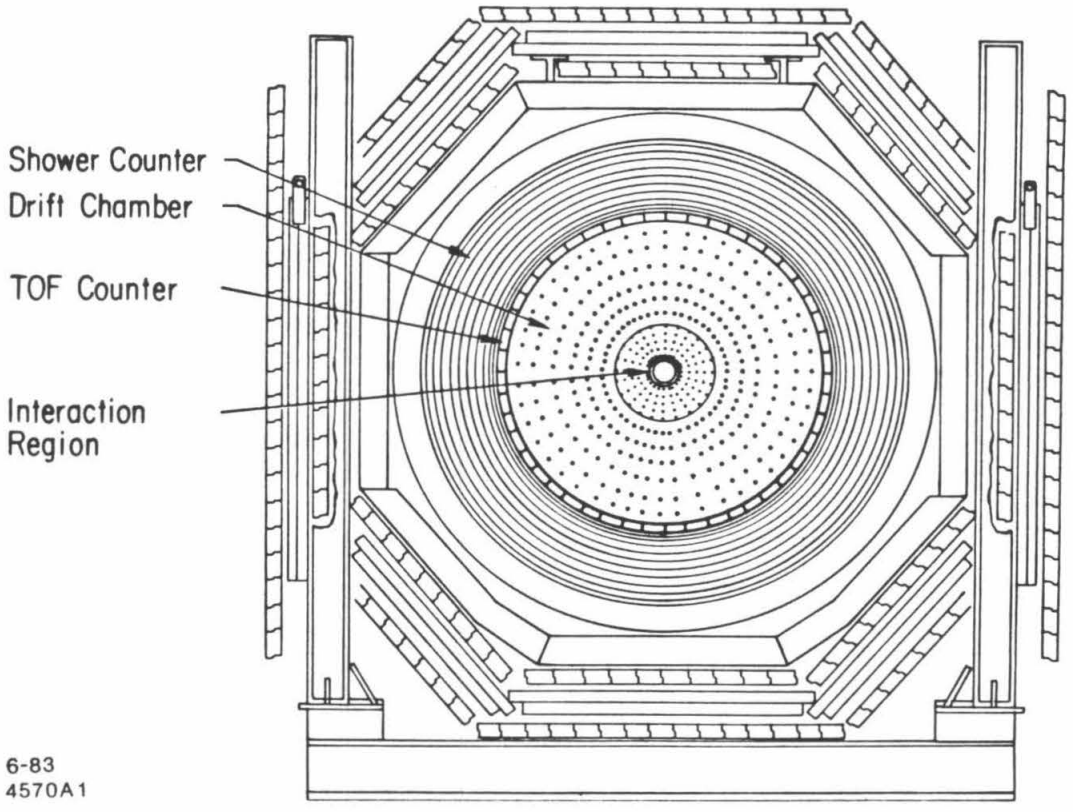

Figure 2.2.1: Axial view of MARK–III detector.

chamber ($L1$), which provides both trigger information and part of the position measurements of the charged tracks. Surrounding the inner trigger chamber is the main drift chamber layer 2 to layer 8 ($L2$ to $L8$). $L2$ has a higher density of sense wires than $L3$ to $L8$ for additional dE/dx measurements and more accurate position measurements used to reconstruct the vertex. $L3$ to $L8$ give the position measurements of the charged tracks only.

Surrounding the main drift chamber is the Time of Flight (ToF) counter, which measures the time of the flight of the particles for particle identification. It is also used in the trigger system and for rejecting cosmic-rays.

The electromagnetic shower counters enclose all detector subunits described

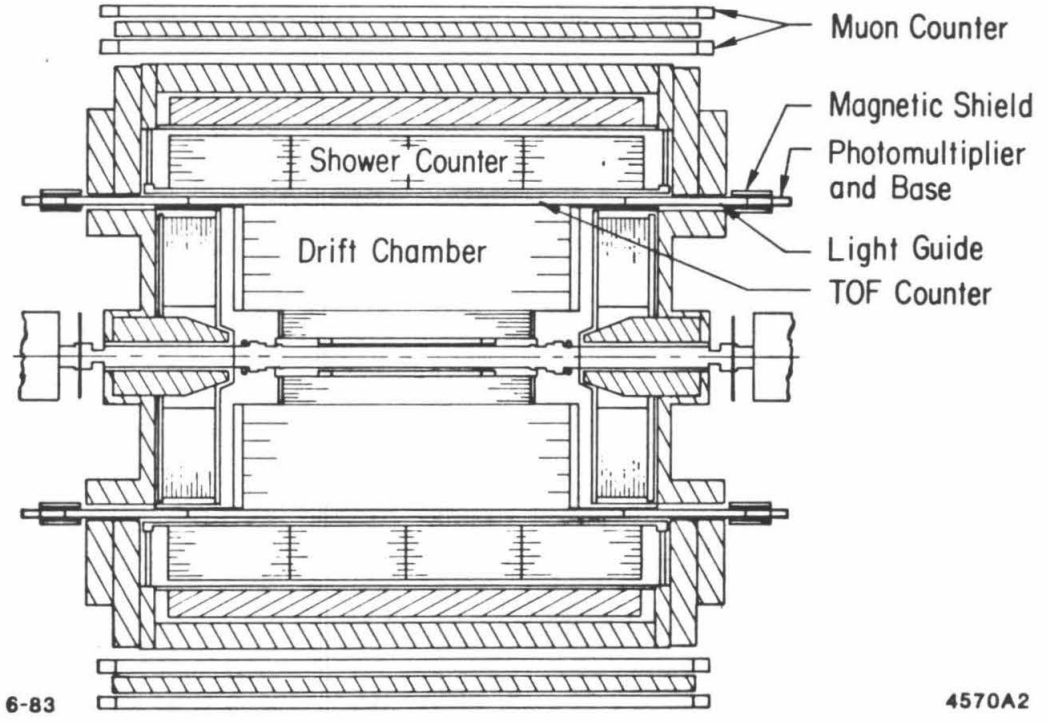

Figure 2.2.2: Side view of the MARK–III detector.

above. The part encircling the Time of Flight counter is called the Barrel shower counter, and the parts located at the two ends of the central drift chamber are called the End Cap shower counters. The shower counters provide the energy and position measurements for both neutral and charged particles.

All of the above detector units are inside a magnetic field provided by a solenoid surrounding the barrel shower counter and flux return steel covering the solenoid and supporting the End Caps.

Finally, outside the solenoid and the steel shell is a set of muon counters for muon detection.

The main parameters of the detector are listed in the Appendix, Table A.I

to Table A.V.

What can be Measured?

In order to understand a reaction completely, we need to investigate what caused the reaction, how the reaction took place and what the final products are. Fig. 2.2.3 illustrates a reaction: an e^+ and e^- annihilated into a photon; the photon produced a $\psi(3770)$ resonance; the $\psi(3770)$ radiated a pair of pions and decayed into a J/ψ ; the J/ψ annihilated into a photon again and the photon produced an e^+e^- pair.

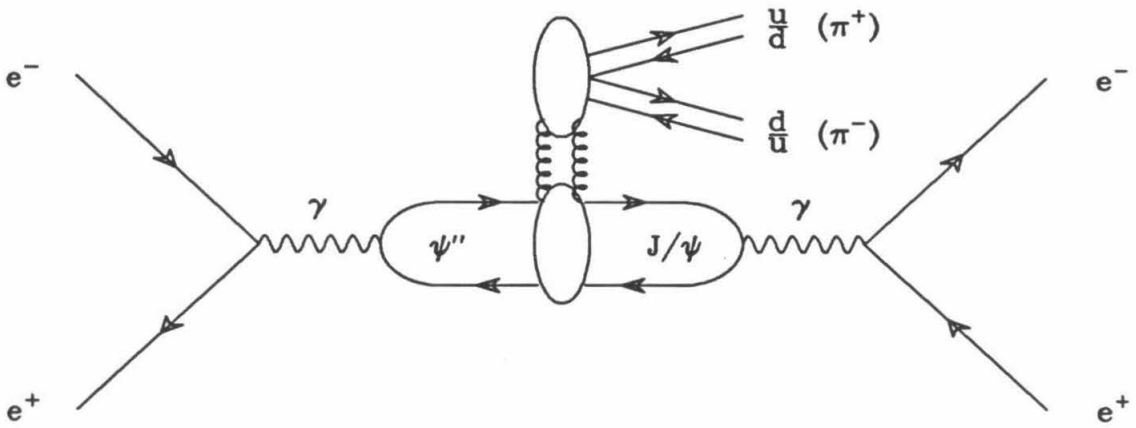

Figure 2.2.3: Illustration of a reaction: $e^+e^- \rightarrow \psi(3770) \rightarrow J/\psi + \pi^+\pi^- \rightarrow e^+e^-\pi^+\pi^-$.

In the Mark-III experiment, the initial reactions are caused by collisions of electrons and positrons. The center–of–mass energy of the reaction is determined from the magnetic field of the storage ring and the orbit of the beam. The reaction rates are found using luminosity, which is determined from luminosity monitors or from radiative Bhabha events during off–line analysis.

Unless an intermediate state has a long enough lifetime to have a measurable track, the detector will not be able to measure it, but information about the intermediate state can still be obtained from its final products. In the energy region of the Mark–III experiment, most intermediate states are bound states of a charm quark and a light antiquark (or an anticharm quark and a light quark). The final state contains photons, neutrinos, electrons, muons, pions, kaons, protons and neutrons. Except for neutrinos, most of the final products are detectable by at least parts of the detector. We can therefore find information about the intermediate states by looking at the properties of their final products.

A complete particle description must include the four–momentum vector, charge and the production coordinates. Therefore, the detector is required to perform good measurements of the momentum and the energy of the particles and the initial vertices of the particles. For a charged particle, the momentum and initial vertex are measured by the central drift chambers, and the energy can be determined from the momentum and the particle type. For a neutral particle, the four–momentum vector can sometimes be determined from the shower counter measurements.

The particle identification is another major part of the measurements. Besides being interesting in itself, it is required for determining the energy of a charged particle. Charged particles are identified by dE/dx , ToF, muon counter measurement, the combination of the central drift chamber and shower counters, and shower counters. Some neutral tracks can be identified by the shower counters.

The Design Concerns

The detector is designed for investigation of the production and decay of particles at a center of mass energy of 3 to 5 GeV. Since the average momentum of final particles in this region is about 600 MeV/c to 900 MeV/c, multiple Coulomb scattering is a major source of error of the momentum measurement. Multiple scattering can be reduced by minimizing the number of radiation lengths of ma-

terial traversed by particles. Table A.I of Appendix A gives a list of the material thickness traversed by particles. The total, 0.0214 radiation lengths, contributes 1.5% to the momentum measurement error, $\Delta p/p$, of the drift chamber.

Since π^0 's play a very important role in physics at 3 to 5 GeV, it is very important to have very good, low–energy photon detection efficiency. Efficiency for low–energy photons is increased by locating the shower counter inside of the solenoid and the steel shell to avoid having a large amount of material in front of it.

2.3 The Trigger System

The function of the trigger is to select most efficiently events produced by the collision of the electron and positron while rejecting backgrounds such as cosmic–rays, beam–gas interactions and noise. The trigger system first looks to see if there is any track produced during the beam crossing. If there is, then the trigger system searches for any possible track inside the central drift chamber and any ToF hit. If all trigger criteria are satisfied, the trigger system will tell the computer to record all data.

The detector efficiency is at a maximum for the trigger decision time less the time between a two–bunch collision, 780 ns at SPEAR. To achieve this maximum efficiency, the trigger system is divided into several levels: level 0, level 1, and level 2, where each higher level will be started only if the lower level is satisfied. Level 0, the lowest level, can be started by the inner drift chamber and ToF, and is designed to make a decision faster than is required to achieve maximum efficiency.

The First Level of the Trigger (level 0)

The level 0 trigger relies on the inner trigger chamber and the time of flight counter information. There are up to six configurations possible for the level 0 trigger. During the $\psi(3770)$ running, the trigger simultaneously looked for two

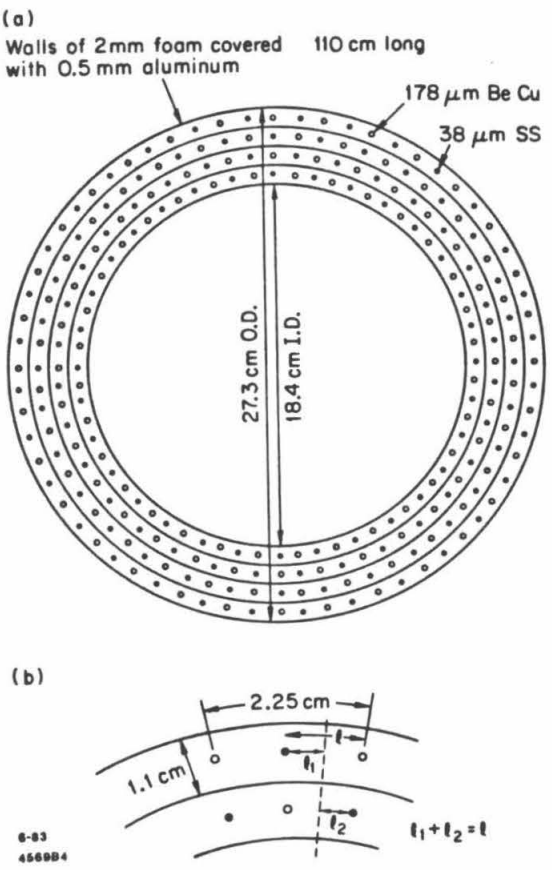

Figure 2.3.1: Axial view of layer 1 (a) and a cell in layer 1 (b).

different event configurations called "two–track" and "one–track". If either one of them was satisfied, a level 1 trigger process would be started.

"Two–track" requires at the least two chronotron outputs. This can occur only if two charged tracks are found by the inner trigger chamber. "One–track" requires at least one chronotron output and one time of flight hit.

The inner drift chamber is described in detail in Section 2.4. The drift time of an ionization track in a cell is in the range of 0 to 250 ns; however, the sum of the drift times of two nearby layers is constant because of the half–cell offset of the sublayers. Fig. 2.3.2 shows the distribution of this constant for hadronic events and the cosmic-ray background.

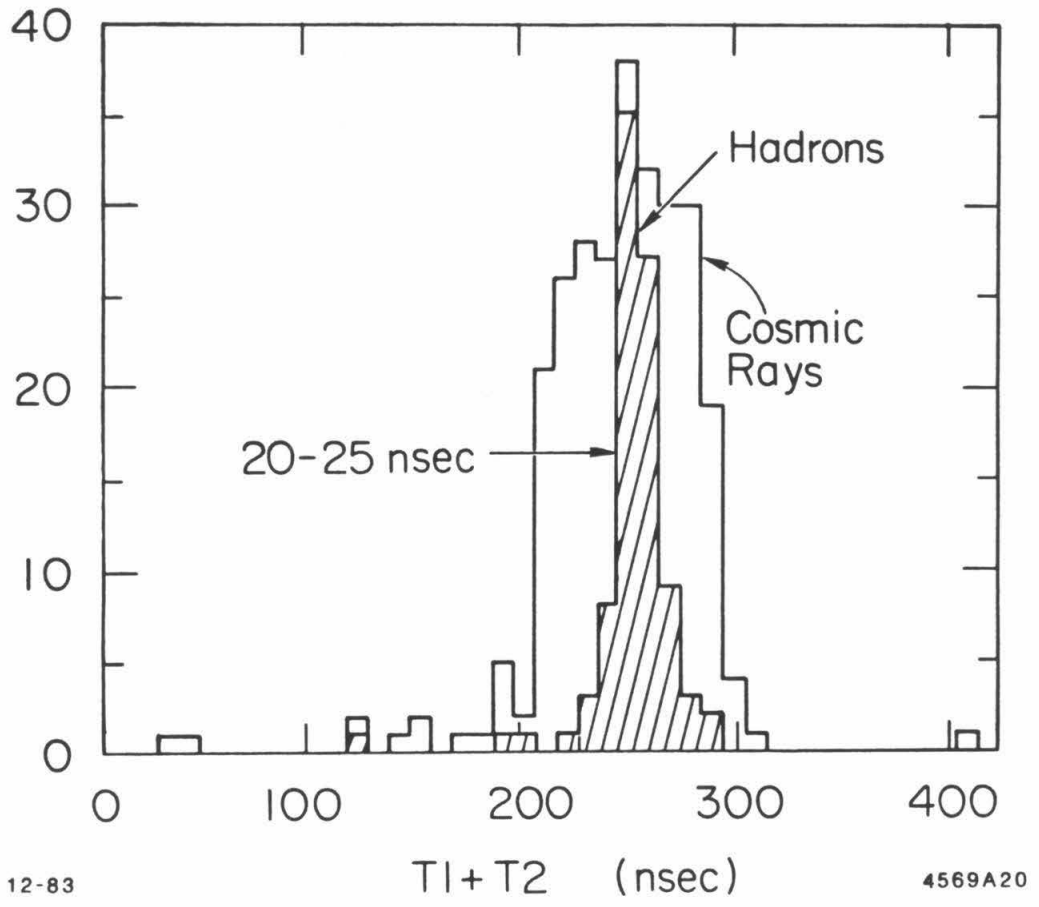

Figure 2.3.2: Chronotron resolution for hadrons. T1 and T2 are the times for sublayer 1a and 1b of layer 1.

Outputs of both ends of each inner drift chamber wire are discriminated and are sent to an "OR" gate to remove the effects of the large pulse–height variations caused by the resistive wire. The output of the "OR" gate is then connected to one end of a tapped chronotron delay line. The other end of the chronotron delay line is connected to the "OR" gate output of an adjacent wire. The time delay of the delay line between the two ends is designed to equal the maximum drift time of the cell (250 ns). The pulses of a track produced by colliding beams from two adjacent wires will therefore meet each other in the delay line. When the two pulses overlap each other on the delay line, the pulse height on the delay line

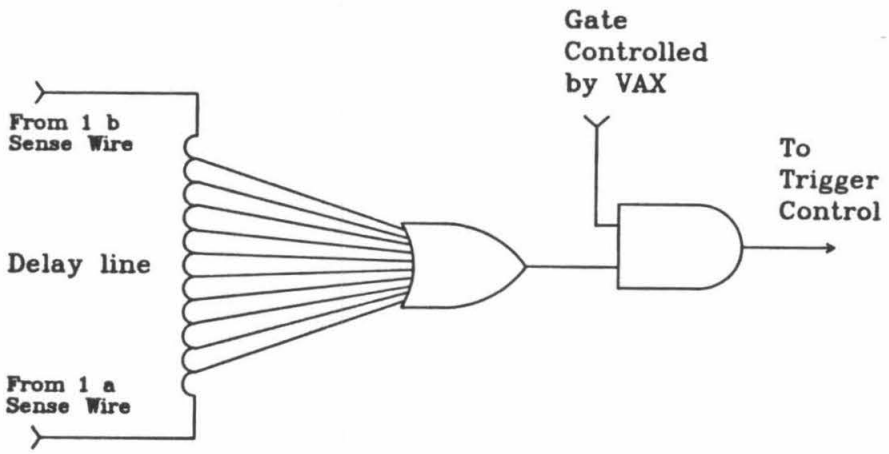

Figure 2.3.3: Chronotron and control logic.

will be doubled and will be above the threshold of the discriminators connected to points along the delay line. Firing a discriminator generates a candidate for a level 0 trigger required to come in coincidence with a window, 100 ns in width, associated with beam crossing and controlled by a VAX computer (Fig. 2.3.3).

Since a beam crossing at SPEAR occurs every 780 ns, the 100 ns window reduces the cosmic-ray trigger by a factor of 7.8. Using the cosmic-ray rate ($\sim 2 \times 10^2 m^{-2} s^{-1}$), the total area of the inner trigger chamber ($\sim 10^{-1} m^2$) and the reducing factor 7.8 that is due to the 100 ns window described above, the cosmic–ray trigger rate is estimated to be about 1 Hz. This is small compared with the total level 0 trigger rate(4-10 KHz at $\psi(3770)$) that is due to beam gas scattering.

Second Level (level 1)

The level 1 trigger relies on the information from layers 1, 3 and 5 of the drift chamber. It also has "two-track" and "one-track" configuration corresponding to those of level 0. The difference here is that level 1 uses programmable logic arrays to implement a rudimentary track-finding algorithm.

The "one–track" trigger covers 80% of the 4π solid angle, while the "two–

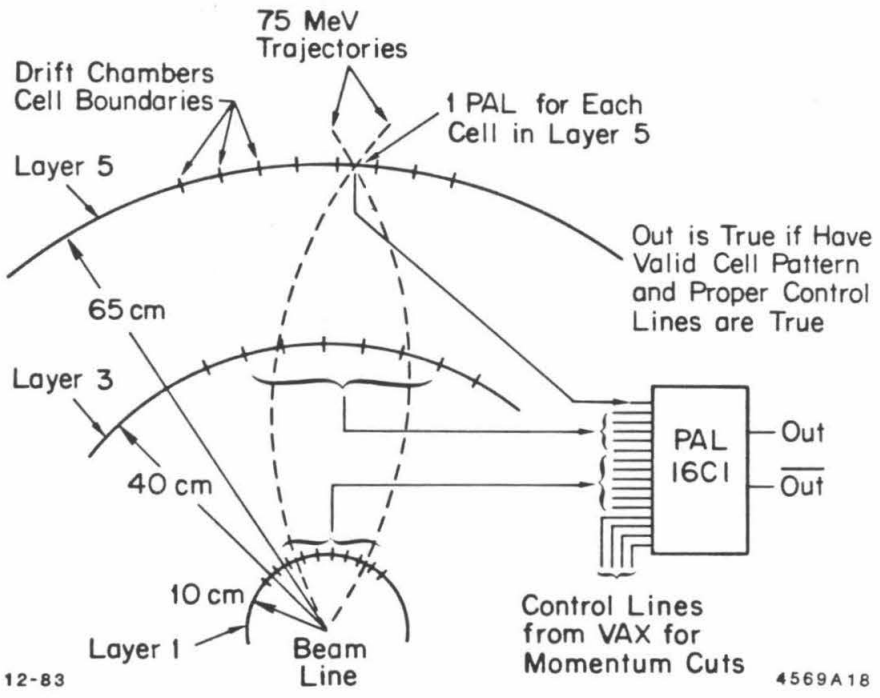

Figure 2.3.4: Circle fit track–finding schematic.

track" trigger covers 88% , which is the coverage of the layer 5.

Each cell in layer 5 is fed to a programmable logical array IC, along with the appropriate cells from layer 1 and 3 (see Fig. 2.3.4). The logical arrays recognize triple coincidences of cells. The minimum transverse momentum of the track that can produce a "TRUE" output is adjustable by the online computer through the programmable logical arrays from 50 to 250 MeV/c.

The total time required for a level 1 decision is 550 ns of the drift time plus the delays of the TTL logical circuits about 1μs.

For the $\psi(3770)$ run when the luminosity was $2.5\times10^{30}/\mathrm{cm}^2\mathrm{sec}$, the total level 1 event rate was 3.5 Hz, 0.25 Hz from real e^+ e^- interactions, 1.5 Hz

from cosmic–rays, and 1.75 Hz from beam–gas. A level 1 trigger will generate a computer interrupt, causing the event to be written onto tape. Since 30 ms are needed to complete this writing procedure, an event rate of 3.5 Hz results in 10% dead time at this level.

Third Level (level 2)

Level 2 uses the Z measurements of the tracks. Since the electronics for the Z measurements is slow, 100 μs are required to make a decision at this level. Off-line studies of the data indicate that the trigger rate could be reduced by a factor of 3 or 4 if level 2 were implemented. However, at $\psi(3770)$ running, because of the need to balance between the reliability of the system and the dead time caused by the background, this level was not used.

2.4 The Drift Chambers

Inner trigger chamber ($L1$)

The inner trigger chamber (layer 1) consists of four sublayers, each of 32 drift cells, forming concentric cylinders of 18.4 cm to 27.3 cm in diameter and 100 cm long. The sense wires are offset by half a cell in alternate layers (Fig. 2.3.1.) Two of the four layers are incorporated in the trigger; the other two are used for tracking only. The 4×32 sense wires of 38 μm stainless steel are maintained at about +2100 volts. The 4×32 guard wires of 178 μm BeCu are maintained at about -200 volts.

The sense wires, made of 38 μm resistive stainless steel, allow determination of Z from charge division. The wires are terminated with amplifiers at both ends. When a charged track passes a cell, a pulse will be generated on the sense wire near the track. Since the wire has non–zero resistance, the relative amplitude of the pulses at two ends will reflect the location of the track in the Z direction.

The average transverse resolution for each wire at $\psi(3770)$ running is about 400 μm. The Z information obtained from the charge division of the sense wires has a resolution about 1% of the total length of the wire, about 1 cm.

Over View of the Main Drift Chamber

The main drift chamber encircles the inner trigger chamber with 7 layers, $L2$ to $L8$. There are two portions of the chamber, the inner part $L2$, and the outer part $L3$ to $L8$. $L2$ is designed with a high density of 13 sense wires in each cell and a total of 32 cells in the layer, allowing the measurement of $d\mathrm{E}/dx$, vertices, and kinks. $L3$ to $L8$ are designed with the total number of cells N, in a layer given by the relationship: $N = 16 \times j$. All cells in $L3$ to $L8$ have three sense wires and are designed to be nearly identical in geometry and dimension except that the Z information is obtained in $L3$, $L5$, $L7$ by the charge division method discussed above, whereas in $L4$ and $L6$, it is obtained by putting wires at slight angles to each other in ϕ and by using the difference of the drift time to calculate Z.

Layer 2 ($L2$)

$L2$ covers 93% of 4π solid angle of the detector. Each of the 32 azimuthal cells consist of 13 sense wires of 20 μm diameter tungsten and 2 guard wires of 57 μm stainless steel. The cells are equally separated by 32 groups of 15 field wires of 175 μm diameter BeCu (see Fig. 2.4.1). The 15 sense and guard wires in a cell are spaced radially in steps of about 1 cm. An equal amount of charge is therefore collected by each sense wire, for later use in the $d\mathrm{E}/dx$ measurements. Alternate sense wires are staggered in ϕ by $\pm 150\mu$m to aid in resolving the left-right ambiguity. The central sense wire is not read out during operation, and therefore the total number of sense wires readout is 12. Pulses of about 20% the height of the neighbor sense wires are induced on the guard wires. These are used by the charge division method to obtain the Z position. A set of resistors are connected between sense wires at the read–out to compensate for the opposite polarity signals. The properties of $L2$ are summarized in Table A.II of Appendix A.

The sense wires are operated at the proportional region with a low gas gain ($\approx 2 \times 10^4$) to provide $d\mathrm{E}/dx$ measurements and to avoid saturation.

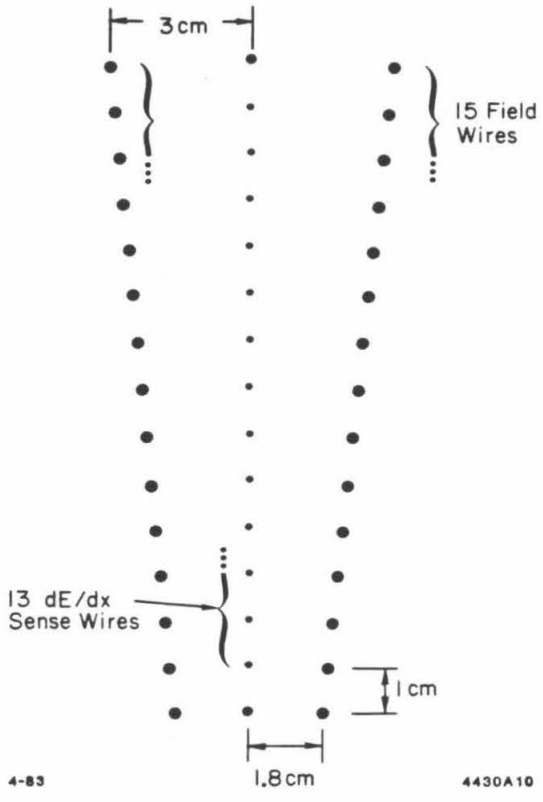

Figure 2.4.1: A cell in layer two.

Layer 3-8 ($L3 - L8$)

The $16 \times j$ cells in each layer Lj contain three sense wires and two guard wires at either side of each sense wire. The sense wires are offset $\pm 400 \mu$m with respect to the guard wires to allow resolution of left-right ambiguity. Layers 4 and 6 are stereo layers with stereo angles of 7.7° and –9.0°, respectively. Fig. 2.4.2 shows the cell structure of $L2$ to $L8$.

The radius of layer Lj is $j \times 13.45$ cm, giving all cells from $L3$ to $L8$ approximately equal size of 5.28 cm full width and 4 cm height. This gives a reasonable similarity of electrical characteristics for later operation and analysis.

The voltages on the field wires are set to be radially increasing to create a

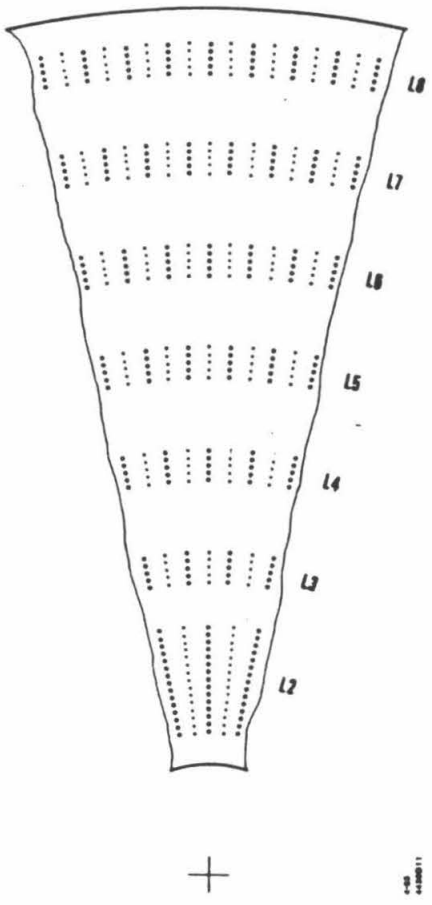

Figure 2.4.2: The cells from layer 2 to layer 8.

uniform field in each cell. The voltage on the central field wires is 4,300 volts for all cells. All sense wires are set at ground potential. With this voltage setup and with the gas mixture of 89% Argon, 10% CO_2, and 1% Methane, a gas gain of approximately 2×10^5 is achieved.

The inner surfaces of the chamber are maintained at voltages of about half that of the field wires of the respective layer, to prevent the deterioration of the field close to these surfaces.

Calculation shows that the field is remarkably uniform over approximately 90% of the cell volume, with a value of 800 volts/cm. With this field and the gas mixture mentioned above, the drift velocity of the electrons is about 5.2 cm/μs;

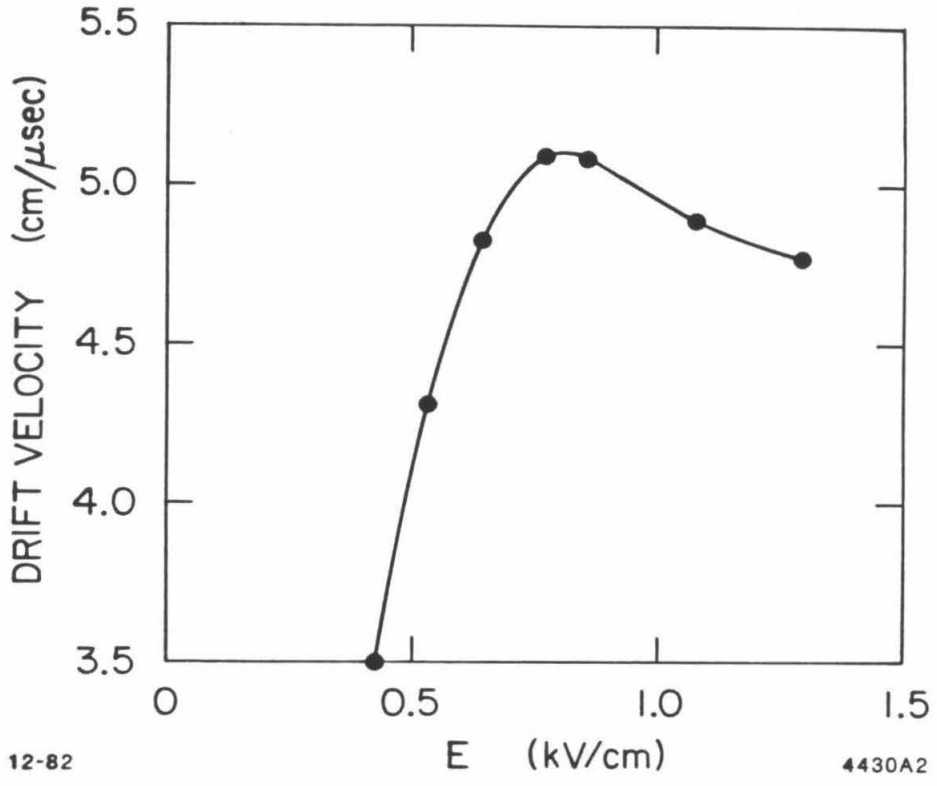

Figure 2.4.3: Drift velocity vs. electrical field.

see Fig. 2.4.3. The cells have a width of about 5.28 cm, resulting in a maximum drift time of about 510 ns.

Chamber operation

A cell in *L2* could give 12 measurements of the track location in the ϕ direction. The pulse–height corrections are made for these position measurements. The left-right ambiguity is resolved by comparing the χ^2 of the fits, assuming the track to be left or right.

A cell in *L3* to *L8* gives 3 measurements of the location of the track. With these measurements, the left-right ambiguity can be resolved, and the resolution of a wire and the amount electrostatic deflection of wires can also be found.

Assuming that a track in a cell is a straight line, then one can define a quantity:

$$\Delta = V_{drift}[(T_1 + T_3)/2 - T_2], \tag{2.1}$$

where, T_1 to T_3 represent the arrival time in wires 1 to 3, and V_{drift} represents the drift velocity of the electron in the gas mixture. Fig. 2.4.4 shows the distribution of Δ for layer 5. There are two clear peaks that represent left and right tracks. Since $\sigma_\Delta = \sqrt{3/2}\sigma_i$ with σ_Δ the error of the Δ and σ_i the error of each T_i measurement, and using the resolution of 220 μm of each wire, one gets σ_Δ=250 μm. The distance between two peaks is much greater than 4σ, giving excellent separation of left and right tracks. The distance between the two peaks is also larger than the four times offset (twice the nominal distance between the central wire and the other two), because of electrostatic repulsion that further separates the wires.

The performance of the chamber is tested by using the J/ψ data sample. The resolution achieved is approximately 250 μm for layer 2 with pulse–height correction and 220 μm per wire for layer 3 to layer 8. The final resolution of the chamber is:

$$\Delta p/p = 0.015\sqrt{1 + p^2} \tag{2.2}$$

$$\Delta\phi = 0.002 \tag{2.3}$$

$$\Delta tan\lambda = 0.011, \tag{2.4}$$

where, p is momentum measured in GeV/c, ϕ is the azimuthal angle in radians and λ is the dip angle.

Fig. 2.4.5 shows the momentum distribution of the $\psi(3770)$ di-muon events from several selected runs. The momentum resolution is 77$\pm$3 MeV/c, which is larger than the 60 MeV/c predicted by Eq.2.2. The major reasons for this discrepancy are that part of layer 2 had not been operating properly and that the drift chamber was not ideally calibrated.

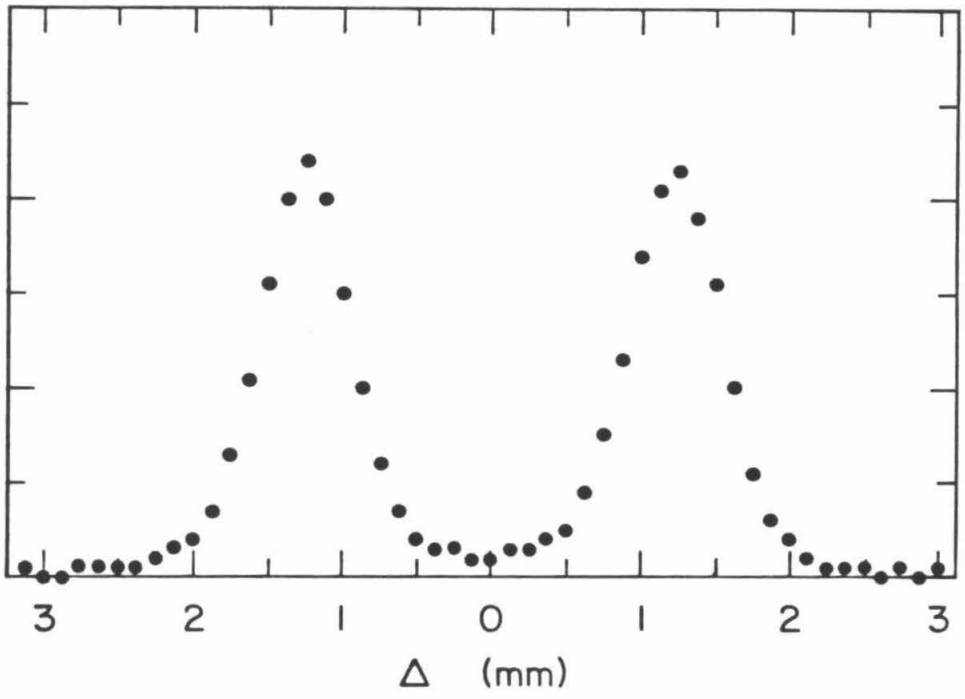

Figure 2.4.4: Resolutions of a cell. Distribution of $\Delta = V_{drift}[(T_1 + T_3)/2 - T_2]$, T_1, T_2, T_3 represents the drift times of a track respect sense wire 1 to 3. Two peaks correspond to the track passing on the left and right of a cell.

2.5 dE/dX SYSTEM

The dE/dx measurements are performed by layer 2 with 12 sense wires out of 13. When a charged particle passes through layer 2, an ionization track is left in the layer, and each read–out sense wire collects a 1 cm sample of the track. These measurements are used to calculate the total dE/dx loss of the particle.

The height of a pulse represents an integral of the current on a sense wire

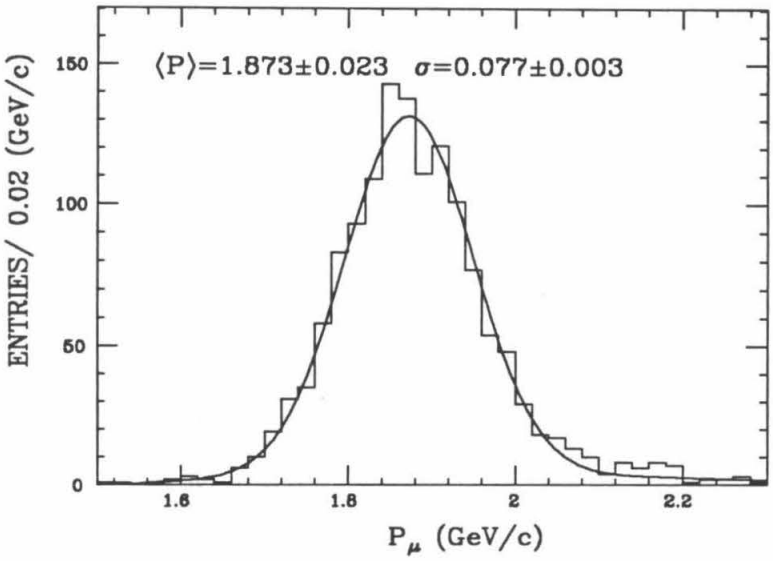

Figure 2.4.5: Momentum resolution in the $\psi(3770)$ run.

over a microsecond period. For each charged track, there are a total of 12 pulse heights that could be found.

The dE/dx system is tested by using data on the decay $J/\psi \to \mu\mu$ from the J/ψ data sample. The pulse height distribution is shown in Fig. 2.5.1. Because the distribution has a long tail on the higher side, the 12 measurements of a track are truncated to insure the best performance. The truncation consists of using only the lowest 9 values of the 12 measurements to obtain the mean value of the pulse height. The truncated mean pulse–height distribution is shown in Fig. 2.5.2. The test indicates that the system gives good $K - \pi$ separation up to 500 GeV/c (see Fig. 2.5.3 and Fig. 2.5.4).

2.6 Time of Flight

Once the time of the flight, the distance of the flight, and the momentum of a particle track are measured, the mass of the particle can be determined. The relationship between the mass M and the momentum p, speed β, track length l

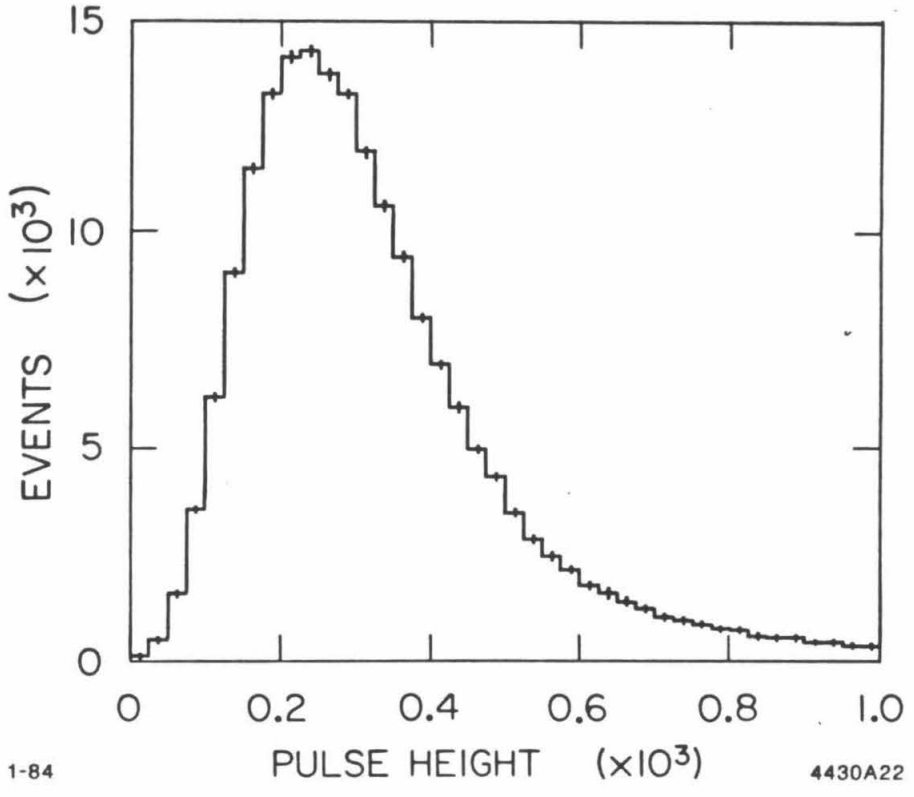

Figure 2.5.1: Single pulse–height distribution of dE/dx .

and the time of flight t is:

$$M = \frac{pc\sqrt{1-\beta^2}}{\beta} = \frac{ptc^2}{l}\sqrt{1-(\frac{l}{tc})^2}. \tag{2.5}$$

The major components of the time of flight system include the scintillation counters, light guides, photomultiplier tubes, read–out electronics and calibration systems.

The particles interact with the scintillator, which then emits photons. Photons pass through the light guide and are received by the photomultiplier tubes. The pulses coming out of the tubes are sent to the DISCO in which the pulses are discriminated and the time to analog conversion is made.

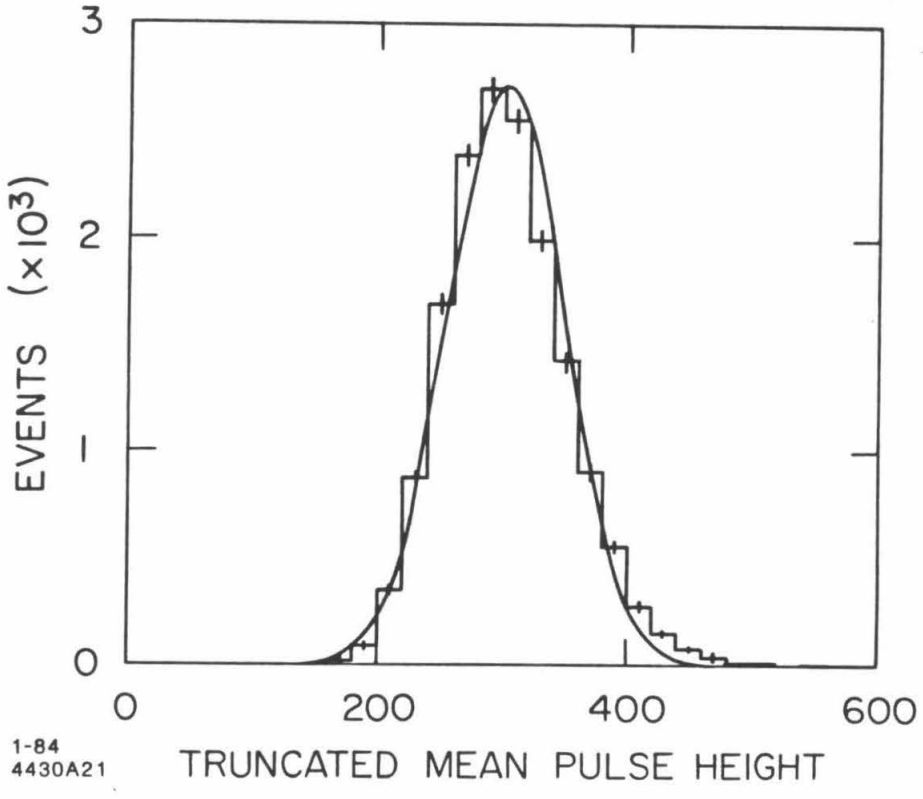

Figure 2.5.2: Truncated mean pulse–height distribution.

The scintillator is 5.1 cm thick, 15.6 cm wide and 317.5 cm long, and is made of Nuclear Enterprises Pilot F plastic scintillator. The edges are angled in order to minimize the gap between neighboring counters. The scintillator is chosen to be as thick as possible and to still fit within the space allowed between the drift chamber and the shower counter in order to produce the maximum possible number of photons. The guides are made of ultraviolet-transmitting (uvt) plexiglass and are bonded to the scintillator by NE581 epoxy. The guides are shaped to fit the holes in the iron yoke of the magnet. They are shown in Fig. 2.6.1.

The scintillators are read at both ends by Amperex XP2020 photomultipliers,

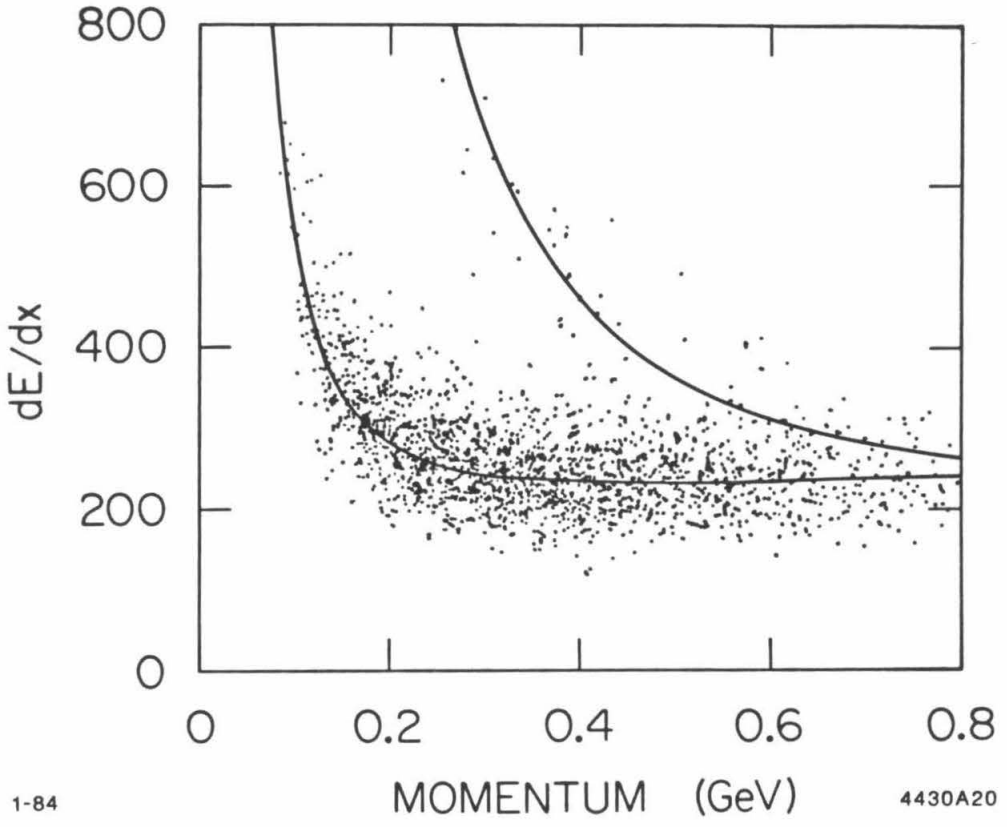

Figure 2.5.3: K-π separation from dE/dx . Solid curves are calculated from Landau form for the most probable energy loss.

which are protected magnetically by two concentric mu-metal cylinders. With the shielding in place, the magnetic field measured at the position of the photocathode was about 0.1G. The voltages on the photomultipliers range between 1.8 kV and 2.5 kV, and the pulses are in the range of 0-2000 pC. The output of the photomultipliers are sent to a DISCO, which is a four–channel discriminator and TAC as well as a charge sampling holder. The two thresholds of the discriminators are computer–controlled and are generally set at 50 mV and 200 mV, while the typical photomultiplier pulse varies around a mean of about 1 V.

Using the J/ψ data sample, the measured time resolution is about 171 ps

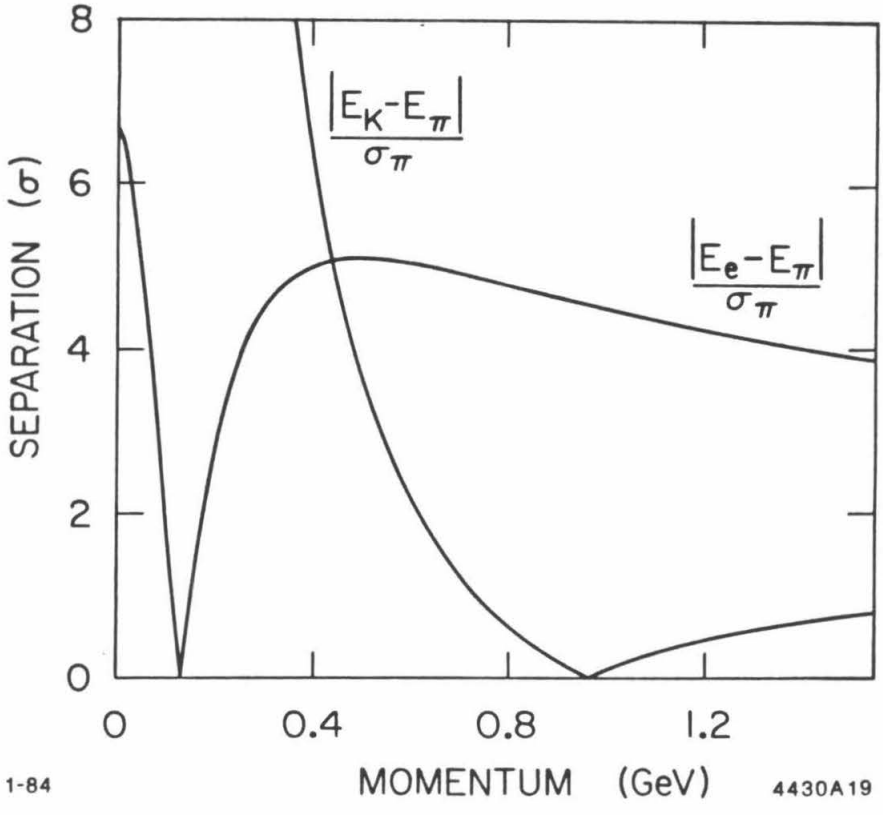

Figure 2.5.4: Calculated K-π and e-π separation in unit of σ_π.

for Bhabha events , is about 175 ps for di-muon events, and is about 189 ps for $J/\psi \to \rho\pi^0 \to \pi^+\pi^-\pi^0$ events.

A measure of the resolution of the ToF system, M^2 vs p for hadronic events at $\psi(3770)$, is shown in Fig. 2.6.2. Note that charged particles must have a minimum momentum of 75 MeV to reach the ToF because of the magnetic field.

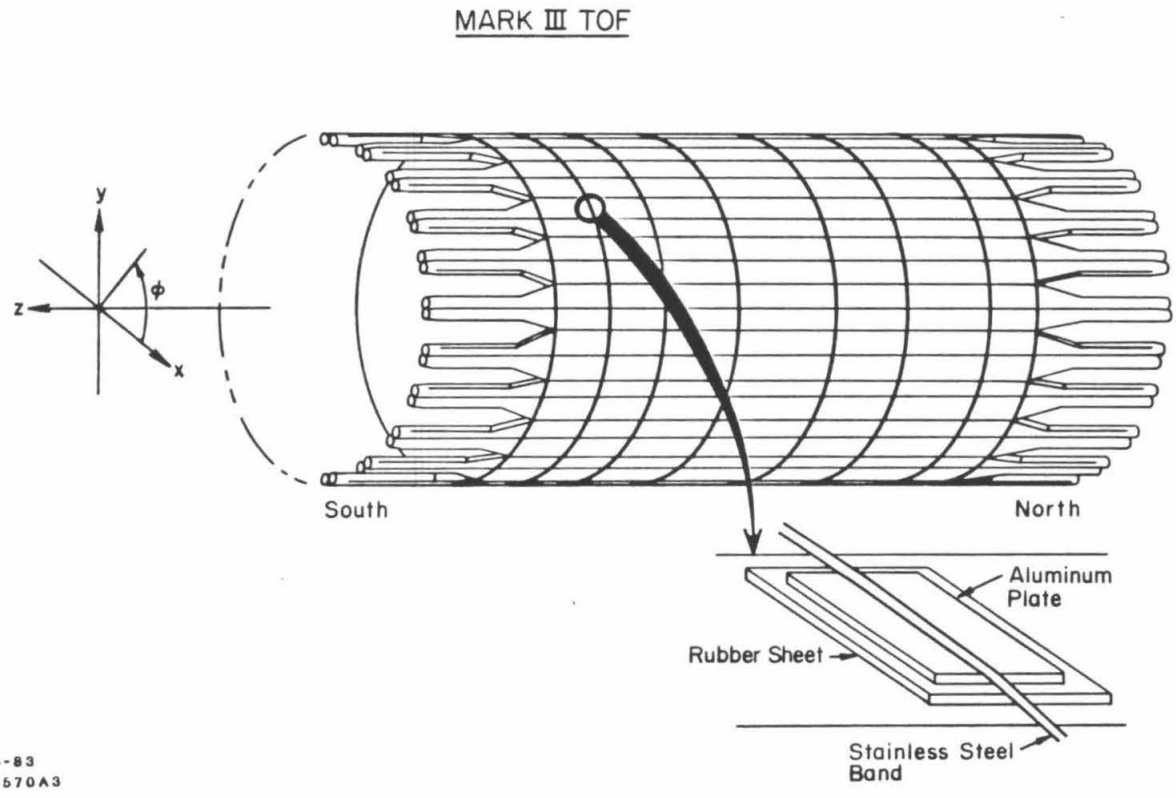

Figure 2.6.1: An assembled ToF counter.

2.7 Shower Counter

The shower counters are used to measure the energy and the direction of particles and can also provide particle identification. They are the only places that the photon information can be efficiently collected.

The shower counters consist of two sections, the barrel and the end cap shower counters. The barrel shower counter is a cylinder encircling the drift chamber. The end cap shower counters are mounted on removable steel doors at the two end sides of the main drift chamber. They are inside the iron to allow a good low energy photon detection efficiency and consist of 24 layers of proportional drift chamber separated by 0.5 radiation length aluminum clad lead sheets to achieve

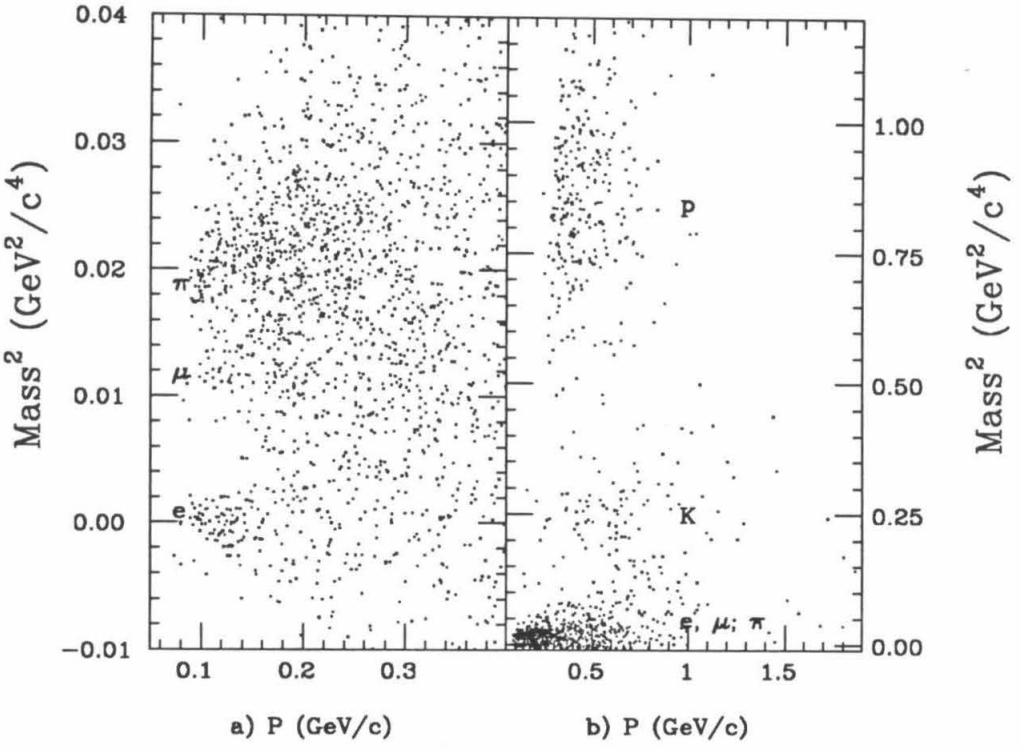

Figure 2.6.2: ToF resolution at $\psi(3770)$. Scatter plot of mass-squared versus momentum of the tracks at $\psi(3770)$ energy. (a) at low momentum showing $e-\pi$, $\mu-\pi$ separation, and (b) the full momentum range.

good energy and position resolution.

A layer of barrel shower counter is made on a lead sheet of 0.28 cm thickness (the first layer is on the 2.3 cm aluminum spool) and consists of 320 cells with widths ranging from 2.4 to 3.2 cm from the inner layer to the outer layer and a height of 1.24 cm. The cells are separated by aluminum I-beams. In the center of each cell, there is a sense wire of 46 μm stainless steel with resistance of about 2600 ohms which allows use of the charge division method to determine the Z position of the shower.

A layer of end cap shower counter also consists of a lead sheet 0.28 cm thick and aluminum tubes of 2.71 width and 1.17 cm height. In the center of each tube

is a stainless steel resistive sense wire for longitudinal position measurements.

The gas mixture used for both barrel and end cap shower counters is 20% methane 80% argon, flowing through the counter at a rate of one volume per day.

Specifications of the barrel and end cap shower counters are given in Tables A.III and A.IV in Appendix A.

Each wire of the first 6 layers of the shower counter is read out at both ends, while the next 18 layers are read in groups of three radially. The wires are operated at 2100 volts with a gas gain of approximately 5×10^4.

The performance of the shower system is studied by using Bhabha and constrained $J/\psi \to \pi^+\pi^-\pi^0$ events. Fig. 2.7.1 shows the energy scale from Bhabha events. Fig. 2.7.2 shows the linearity of the shower system by using constrained $\pi^+\pi^-\pi^0$ events. Fig. 2.7.3 shows the efficiency for photons by using constrained $\pi^+\pi^-\pi^0$ events. The conclusion of these studies is that the energy resolution is given by $\Delta E/E = 17\%/\sqrt{E}$, the photon detection efficiency is 70% at 70 MeV and is higher than 98% at 100 MeV. The resolution in the Z direction is 0.8% of the wire length or about 2 cm.

2.8 MAGNET

The magnetic field is essential for the momentum measurement of charged tracks. The magnet provides a magnetic field of 0.4 Tesla at the center of the spectrometer. The coil is located behind the electromagnetic shower detector. The coil consists of four layers of 5 cm by 5 cm aluminum conductor with a 2.5 cm diameter hole through, flowing with cooling water. The power consumption of the coil is 1 MW.

Two compensators are built into the end cap flux return iron to compensate for the effect of the axial magnetic field on the beam.

The magnetic field inside the spectrometer was measured before the drift chamber and the shower counters were installed. The measured field was fitted

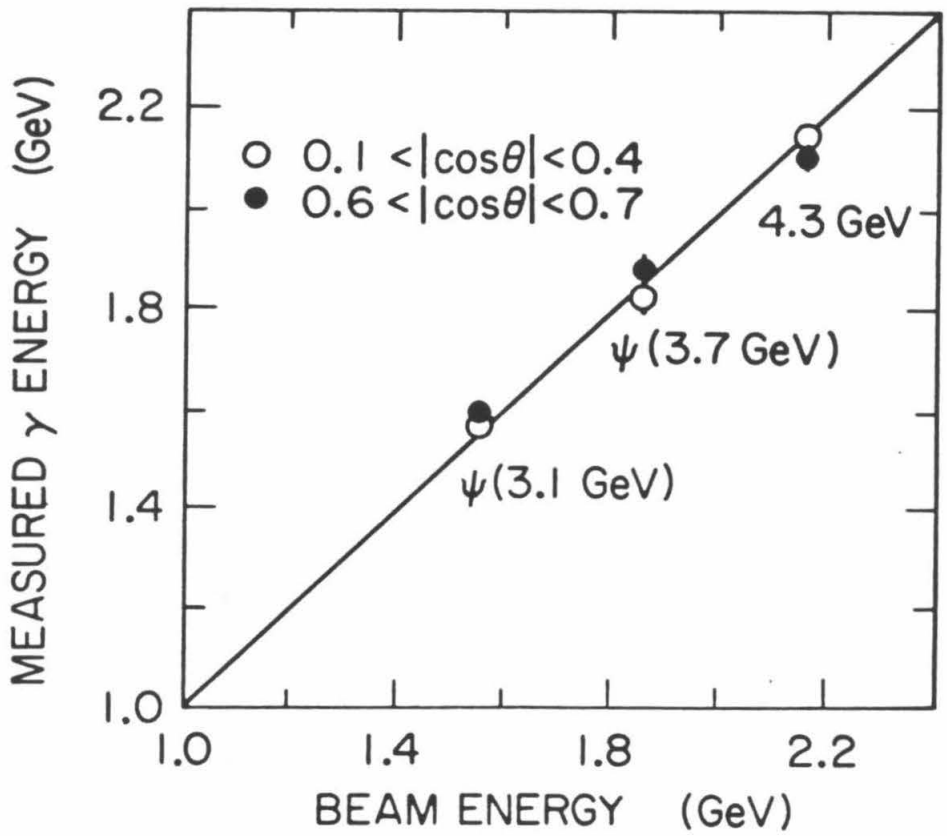

Figure 2.7.1: Measured shower energy of Bhabha events. Data are shown for two different regions of $cos\theta$.

with a polynomial expression. A total of 17 parameters was required to describe the field to an accuracy of about 0.2% over the volume of the tracking chamber.

2.9 The Muon Detection System

Since the masses of pions and muons are very close to one another, it is almost impossible to separate them by ToF (see Fig. 2.6.2). However, the cross sections for interacting with material of the pions and muons are different, pions having a larger cross section. Using this difference of cross sections, the muon detector can separate muons from pions.

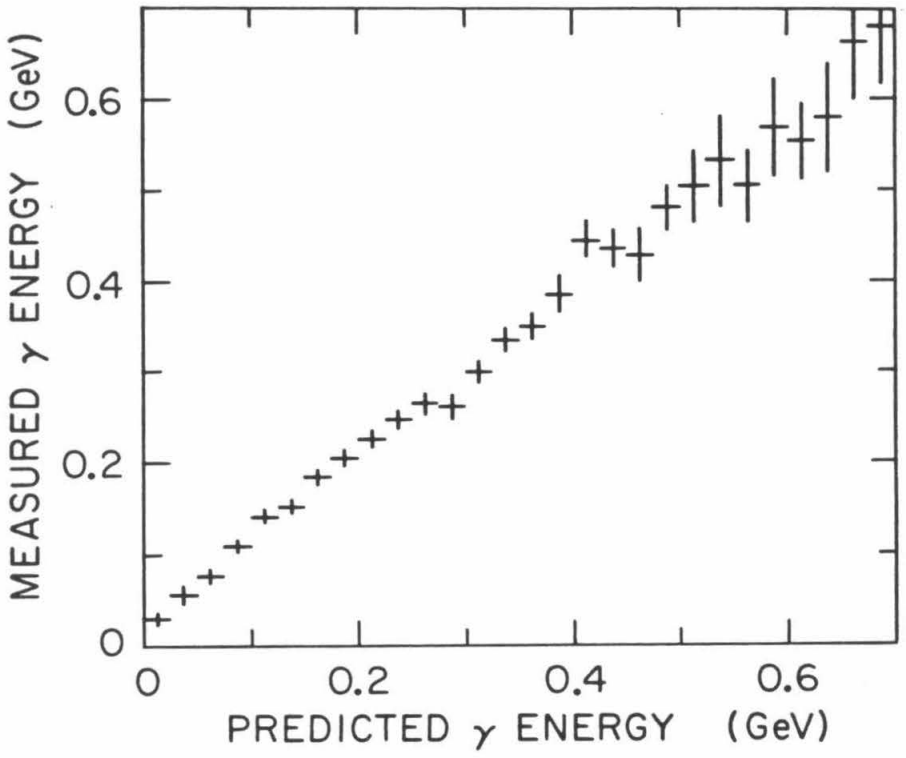

Figure 2.7.2: Measured γ energy vs. predicted γ energy, where the predicted energy comes from the fitted photon energy in the 5C fit of events $J/\psi \to \pi^+\pi^-\pi^0$.

The muon detector is located outside the magnet flux return steel. The detector consists of two layers of counters separated by 13 cm steel plates, covering a total of 65% of 4π solid angle. Each layer is constructed by overlapping proportional tubes of radius 2.5 cm and length 420 cm. The sense wires located at the center of the tubes are 50 μm with resistance 380 ohms/m to allow charge division to determine the Z position of the hits. The magnet flux return steel and the separating steel plates are used to stop pions.

The sense wires operate at 2700 V with a gas mixture of 20% methane and

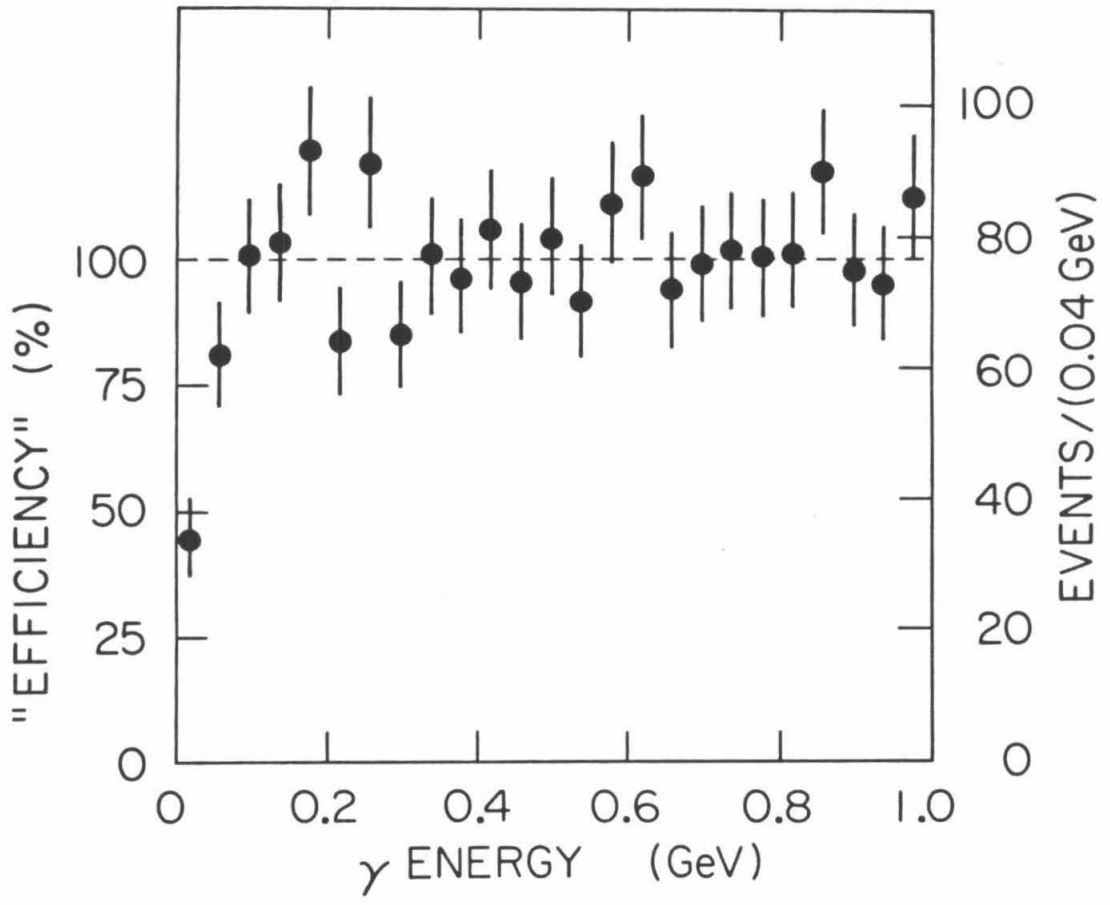

Figure 2.7.3: γ **detection efficiency vs.** γ **energy, where the energy of the** γ **is determined from the 5C fit of the events** $J/\psi \rightarrow \pi^+\pi^-\pi^0$.

80% argon. The efficiency of the counter has been measured to be 99% or better for a muon momentum larger than 800 MeV with the gas flowing at a rate of one volume every 36 hours.

Using the data sample of the decay $J/\psi \rightarrow \rho\pi \rightarrow \pi^+\pi^-\pi^0$, the fraction of pions or their decay products that reach the muon detector inner layer and outer layer is shown in Fig. 2.9.1. For a pion momentum range of 1 GeV/c to 1.5 GeV/c, the fraction of the pions reaching the inner layer is about 14% and of those reaching the outer layer, about 4.5% .

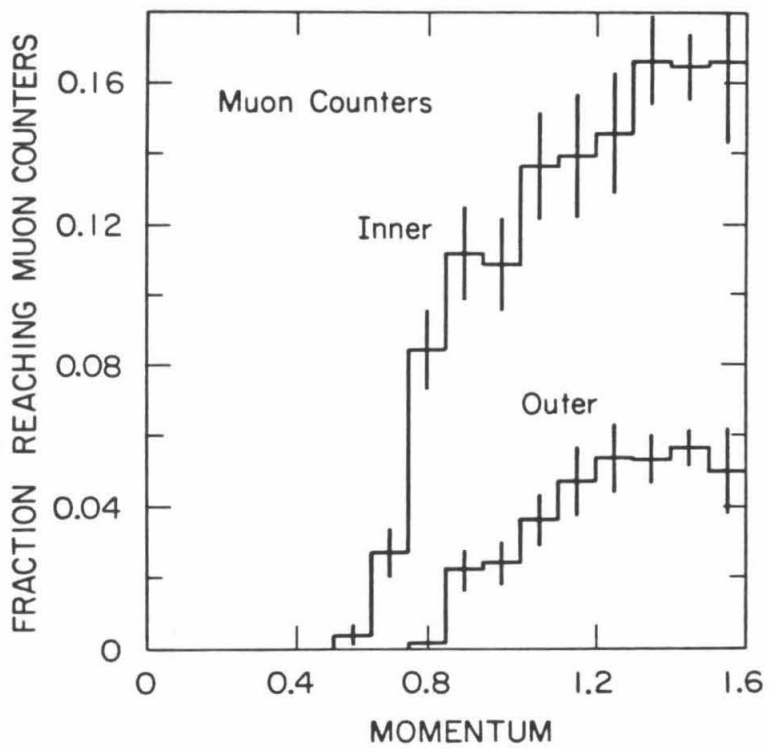

Figure 2.9.1: Pions or their decay products reach the muon detector. The upper data are for the inner layer and the lower are for the outer layer.

3. PARTICLE IDENTIFICATION

3.1 INTRODUCTION

Particle identifications played a very important role throughout the analysis. In this chapter, the definitions of "track type" and of "possible track type" are given. The "good photons" and "good charged tracks" are defined. The efficiencies of the identifications and some comparisons between the real and Monte Carlo data are also made.

A track is said to be of a given type if and only if a parameter (*i.e.*, ToF, E/P, *etc.*) has been measured, indicating that this type is the most likely explanation. For example, a track is said to be a proton track based on ToF, if this track has ToF weight of proton greater than 1.1% and weight of other particles less than 1.1% .

A track is said to be a possible type if there is more than one explanation for all the measured parameters. For example, if a track has only ToF, and the weights of kaon and pion are greater than 1.1% and the weights of others are less than 1.1% , then this track is called a possible kaon and a possible pion track.

A particle may be directly identified by any one of the following methods:

1. dE/dx .
2. Time of Flight (ToF).
3. E/P or E, where E is the energy measured by shower counters and P is the momentum measured by the central drift chamber.
4. Muon counters.

For charged tracks with momentum greater than 80 MeV, the ToF counters can be reached. Electrons and pions can be separated by ToF when their momentum is below 200 MeV/c (see Fig. 2.6.2). Kaons can be separated from other particles for a momentum below 800 MeV/c. Protons can be separated from other particles in the entire momentum range of this experiment.

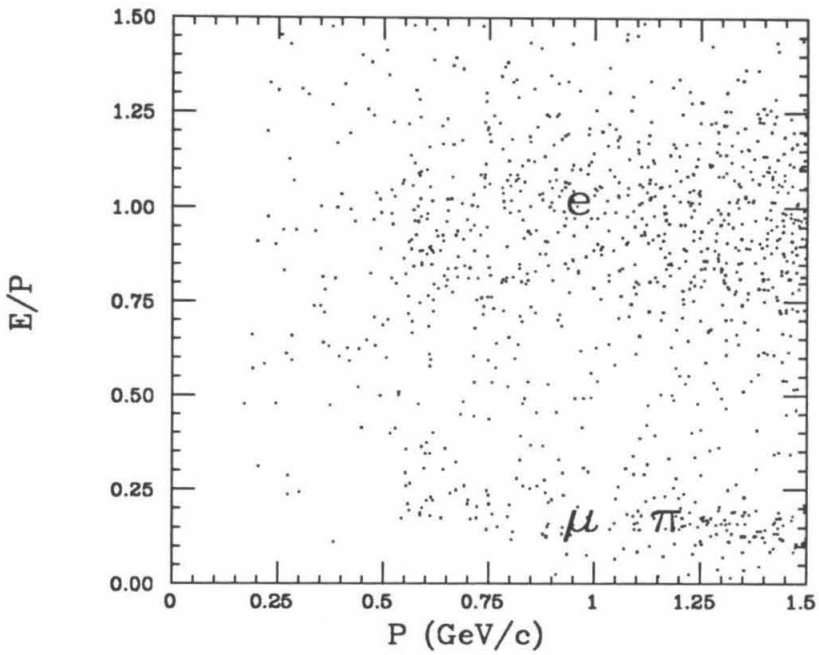

Figure 3.1.1: P vs. E/P for e, μ *and* π.

Since muons and pions are very close in mass, it is very difficult to distinguish between them. Muons can be identified by muon counters if they are in the direction covered by the counter and have a momentum greater than 800 MeV/c.

Electrons and heavier mass particles can be partially separated by using the E/P method. The measured momentum vs. the E/P is shown in Fig. 3.1.1. The electrons have E/P centered at 1 at all momenta. For $P \geq 500$ MeV/c, the E/P method gives very good separation between electrons and muons or pions. For $P \leq 500$ MeV/c, E/P distributions of electrons, muons and pions start intersecting, since the E/P of the muons and pions approaches 1 because of energy loss in the shower counter which is comparable to the total particle kinetic energy. Therefore, the E/P method can find all electrons in the full momentum range but a large contamination of heavier particles is expected for momentum of the tracks less than 500 MeV/c.

The E/P method is efficient and simple for selecting electrons. This is not true for selecting muons or pions, since their E/P distribution is not a straight

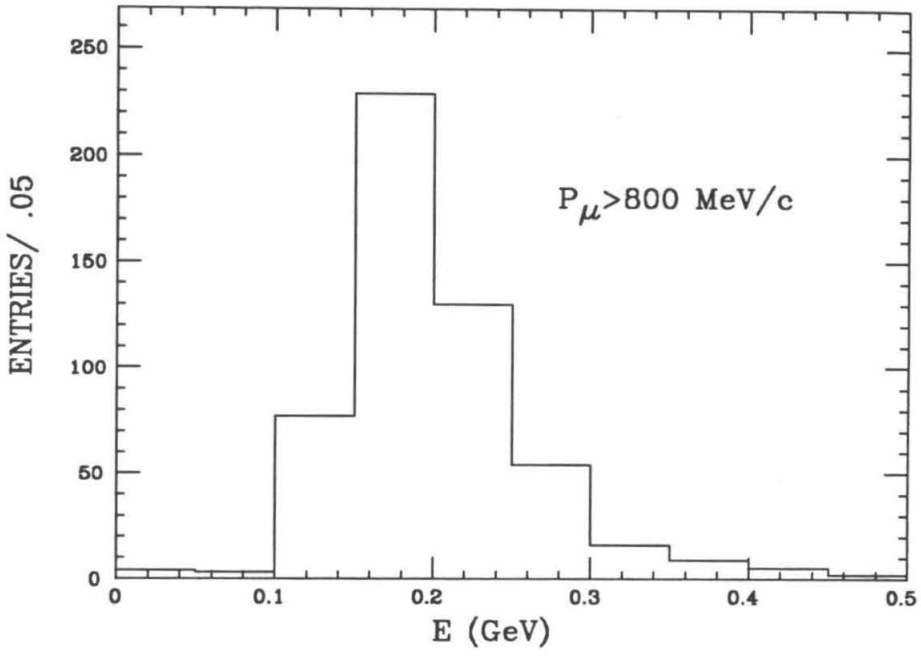

Figure 3.1.2: Shower energy of muon tracks.

line.

Pions and muons can be identified by the total energy deposit in the shower counter. For muons with momentum greater than 800 MeV/c, the energy distribution of the showers is shown in Fig. 3.1.2. For pions, the correlation between the momentum and the shower energy is shown in Fig. 3.1.3.

In the following sections, the details of how each particle type has been identified are discussed.

3.2 ELECTRONS

Electrons are identified by E/P and ToF.

An electron is defined as a track with E/P greater than 0.6 c and at least a possible electron from ToF. If a track does not have a shower, then it must be identified as an electron from ToF.

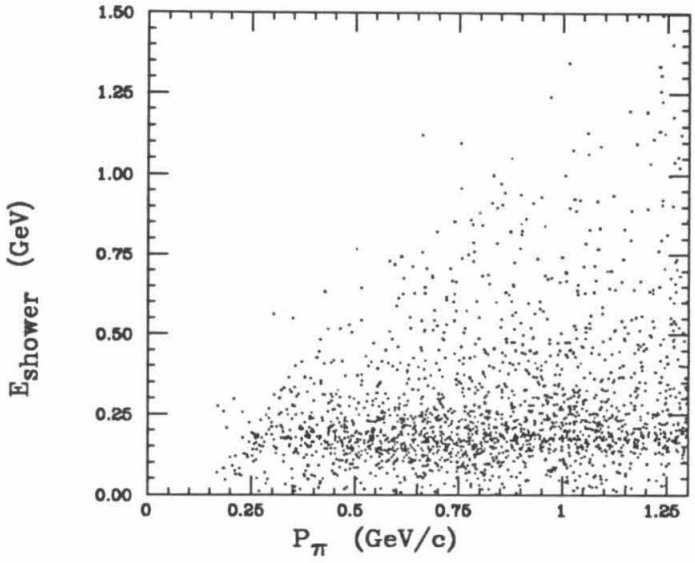

Figure 3.1.3: P vs. E for pions. The pions are from $\rho\pi$ events in J/ψ data sample.

A possible electron track is a track without a shower with a ToF identification as a possible electron.

As mentioned earlier, the E/P method gives very good separation for track momenta greater than 500 MeV/c, and ToF gives good separation below 200 MeV/c. There is a region from 200 MeV/c to 500 MeV/c in which none of the simple methods can give good separation. A more complex binary tree algorithm can give reasonable separation in this region[36]. For simplicity, only E/P and ToF are used in this analysis since the poor separation from 200 MeV/c to 500 MeV/c has not been found to be crucial to the analysis.

The efficiency of electron identification is tested by a Monte Carlo simulation; see Fig. 3.2.1 for the efficiency distribution. In this and in following figures, efficiency for a type of identification (type, possible type, or not type) is defined as the number of tracks with this identification divided by the total number of the tracks in the sample. The efficiencies are better than 90% and the distribution is flat for momenta greater than 300 MeV/c.

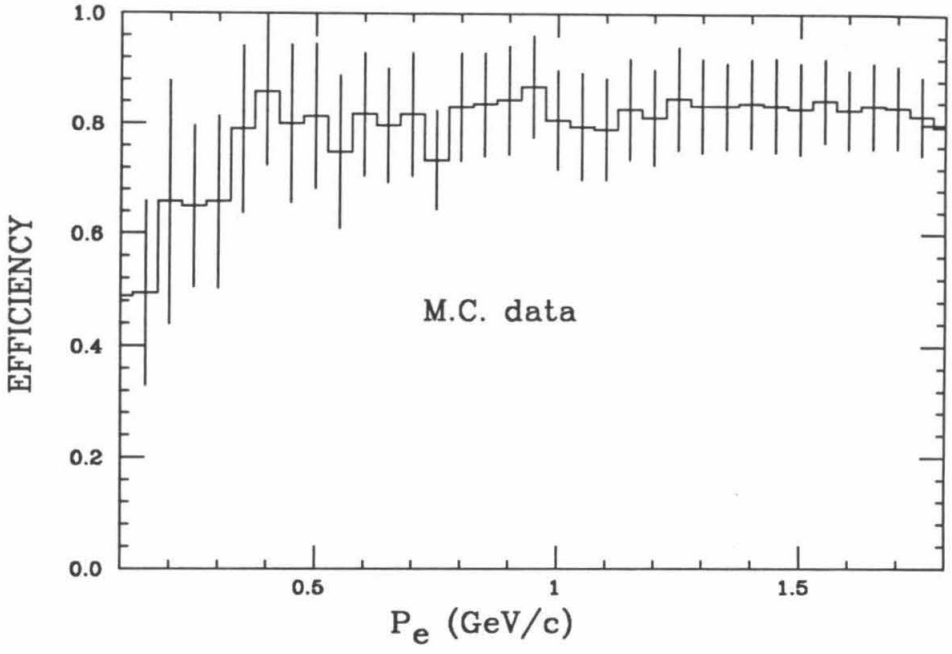

Figure 3.2.1: Electron identification efficiencies.

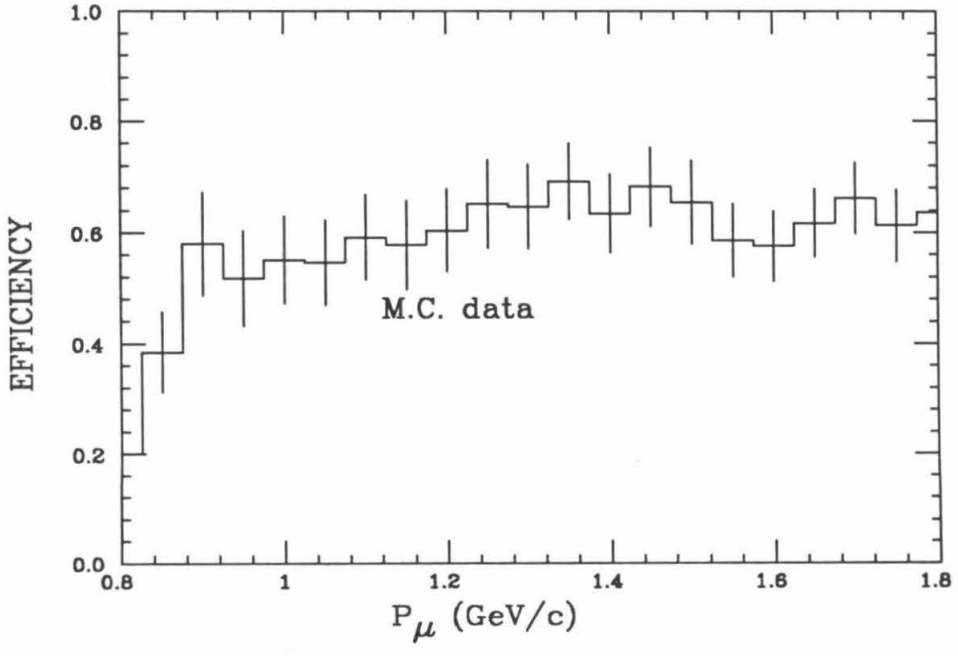

Figure 3.3.1: Muon identification efficiencies.

3.3 MUONS

The momentum of muons in this analysis is greater than 1 GeV; therefore, the muon tracks have a momentum large enough to reach the muon counters.

A muon track is defined as a track having two layer hits in the muon counter.

A possible muon track is one with total shower energy less than 300 MeV but in a region not covered by muon counters. The shower energy distribution of muons is shown in Fig. 3.1.2. It can be seen that more than 90 % of the tracks have shower energy less than 300 MeV/c.

The efficiency of the muon identification is tested by using a Monte Carlo simulation (Fig. 3.3.1).

3.4 PIONS

The masses of a pion and a muon are very close to one another; therefore, it is very difficult to distinguish between them unless they hit the muon counters. In this analysis, a muon track maybe called a pion track unless a two–layer muon counter hit has been associated with the track.

A pion (or a possible pion) track is one with:

1. shower energy in the shower counters less than 500 MeV (see Fig. 3.1.3),
2. no associated two–layer muon counter hits, and
3. ToF indicating that it is a pion (or a possible pion) track.

Fig. 3.4.1 shows the efficiency distributions determined from real J/ψ and Monte Carlo data; both are for process $J/\psi \rightarrow \rho\pi \rightarrow \pi^+\pi^-\pi^0$. The Monte Carlo data show a slightly higher efficiency than the real data. Pions have been misidentified as muons or kaons less than 5% of the time.

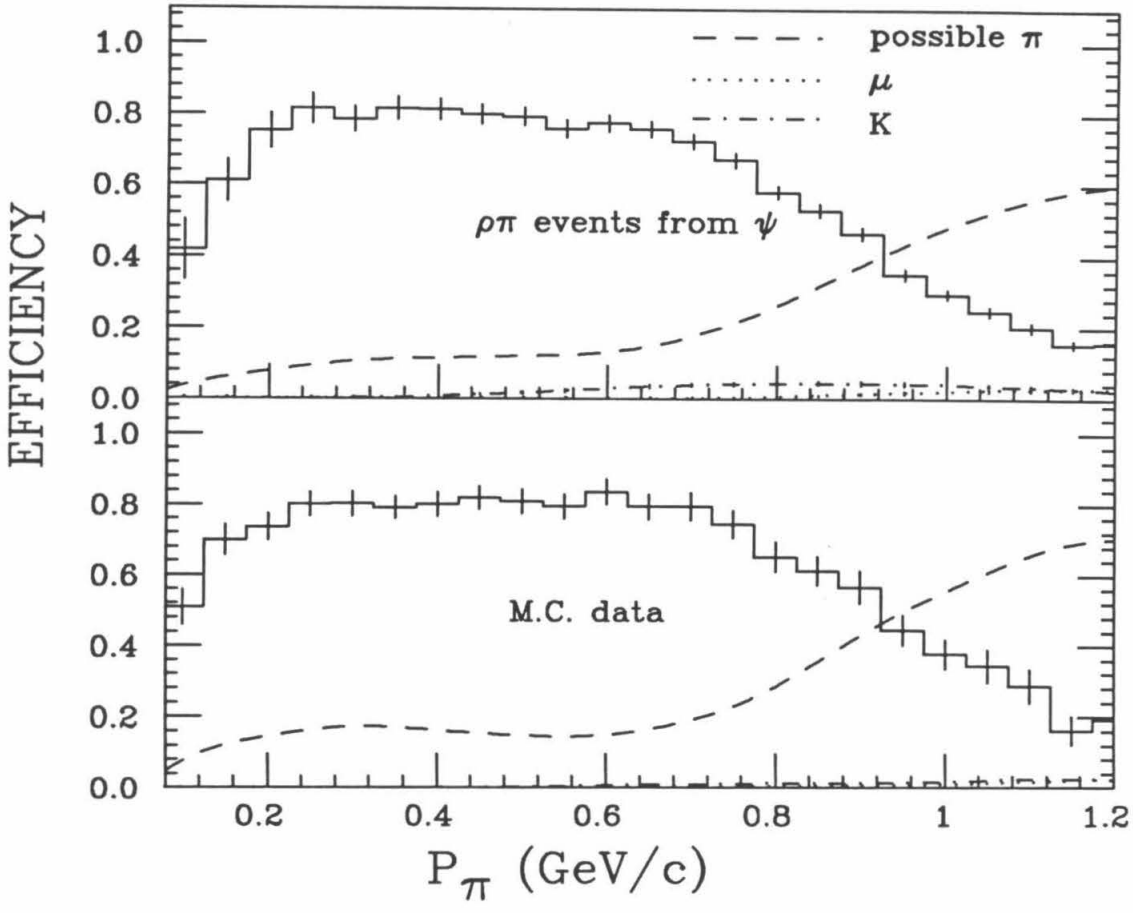

Figure 3.4.1: Pion identification efficiencies.

3.5 KAONS

Kaon tracks are identified by ToF only. A (possible) kaon track is: a (possible) kaon from ToF.

Fig. 3.5.1 shows the efficiency of kaon identification. A large fraction of the kaons are misidentified as non–kaon tracks at low momentum because of decays of the kaons. At about 1 GeV, the distributions ToF of the pions and kaons start to overlap, and the efficiency of the identification starts decreasing.

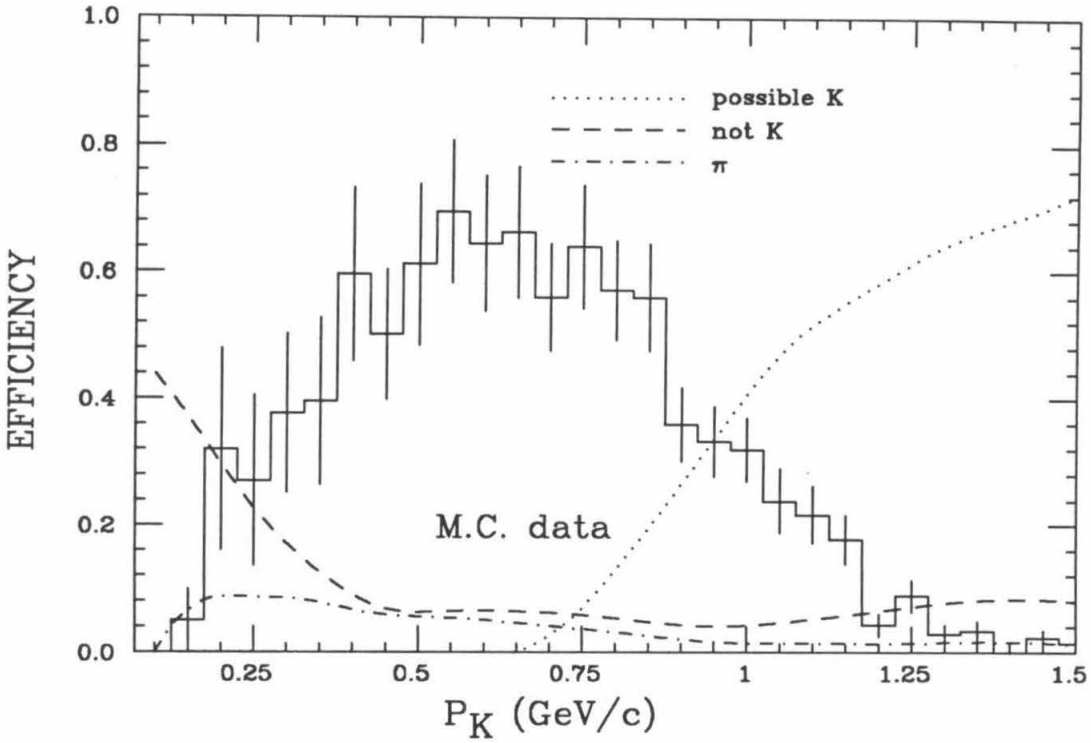

Figure 3.5.1: Kaon identification efficiencies.

3.6 PROTONS

A (possible) proton is defined as a track that is a (possible) proton from ToF.

Fig. 3.6.1 shows the efficiency for proton identification. At very low momenta, the efficiency is low because of the large cross section for proton nuclear scattering.

3.7 GOOD PHOTON

In each event, many photons may be found; some of which are real photons and some fake photons from noise or cosmic–rays. The fake photons are a major source of the background.

A "good photon" is a track found in the shower counters, which is very likely to be a real photon. A "good photon" is defined as one for which the following

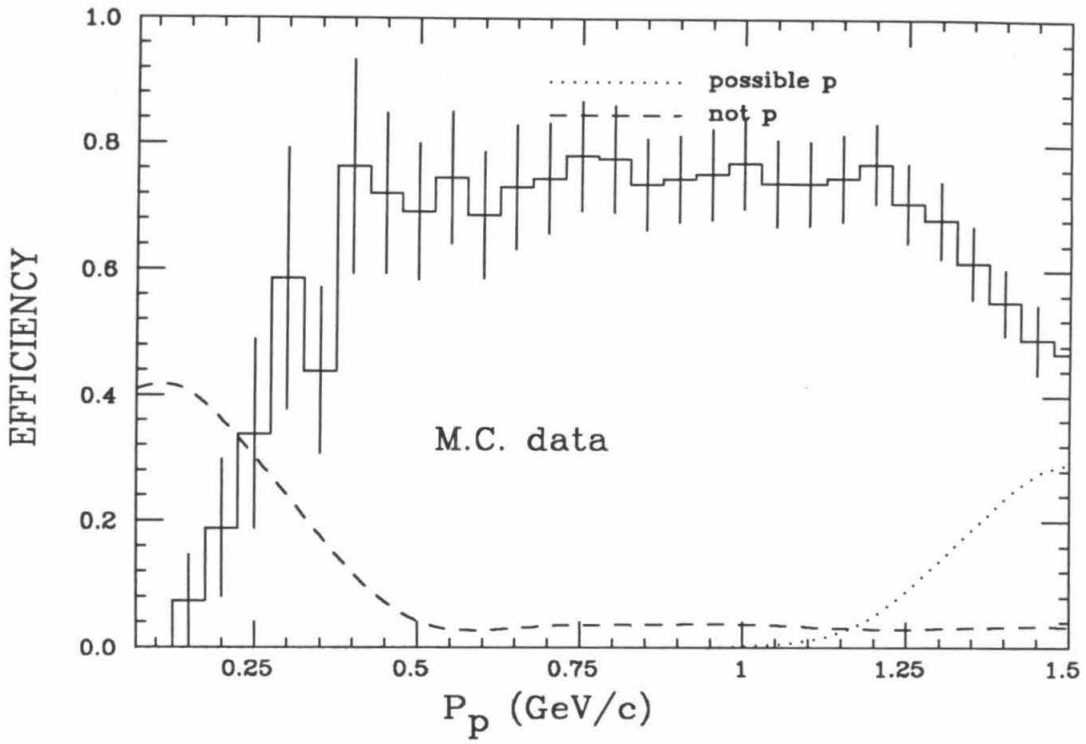

Figure 3.6.1: Proton identification efficiencies.

requirements are satisfied:

1. The shower length is at the least 2 layers deep. The purpose of this cut is to reduce the noise background. In general, the noise is most likely to appear in a single layer; the probability that two layers have noise hits close to each other is very small. Fig. 3.7.1 is the distribution of the lengths of the photon shower from real events of the type $J/\psi \rightarrow \rho\pi^0$. The "true" energy of the photon is determined by a 5-C fit of the events. The true energies of the tracks are 500 ± 5 MeV, 100 ± 5 MeV and 50 ± 5 MeV.

2. The shower should start before layer 8. This cut reduces background from both noise and cosmic-rays. For a photon we have:

$$P(x) = e^{-\frac{7x}{9x_0}} \quad , \tag{3.1}$$

where $P(x)$ is the probability of finding a photon at distance x inside a

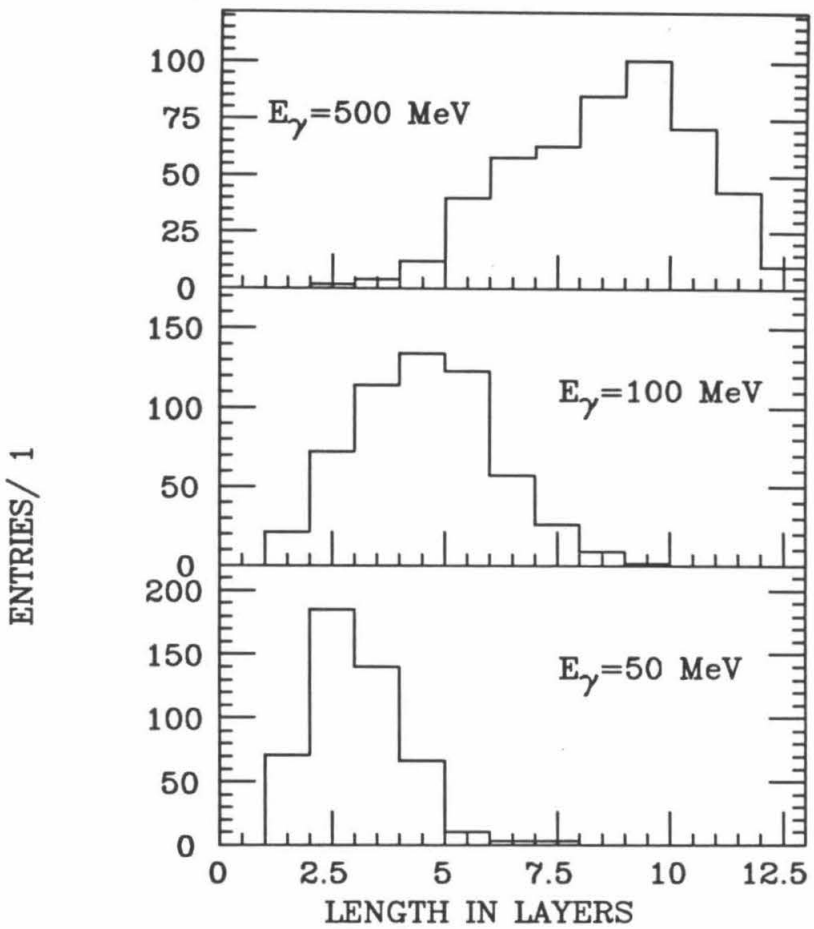

Figure 3.7.1: Shower lengths.

material having radiation length x_0. The first six layers are 0.5 radiation length each. Each of the remaining(from layer 7 to layer 12) layers is 1.5 r.l. The total material in front of the first layer of the shower system is about 0.5 radiation length. Therefore, the efficiency of this cut for good photons can be estimated as:

$$\epsilon = 1. - e^{-\frac{7\times 4.5}{9}} = 0.97 \quad . \tag{3.2}$$

Using real data of type $J/\psi \rightarrow \rho\pi^0$, the distribution of starting layers for the showers is shown in Fig. 3.7.2. The "true energies " of the photons is defined as the same as for the previous point.

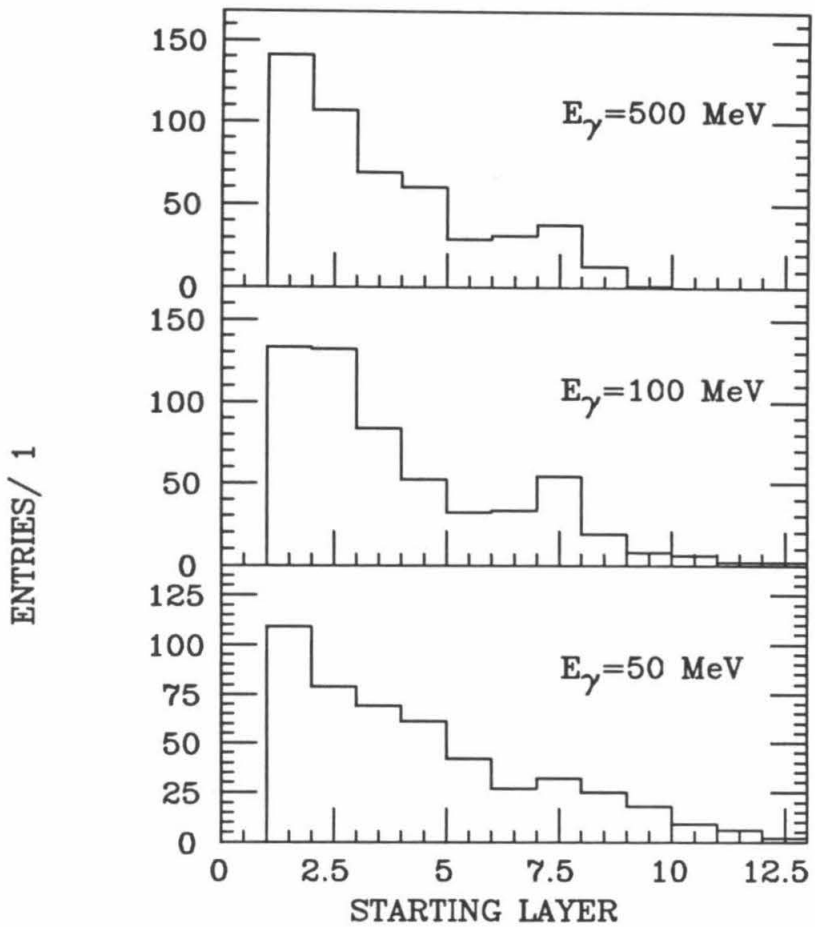

Figure 3.7.2: The layers where showers started.

3. There is no charged track entering the shower counter near the photon with a cosine of the direction angle respect to the photon greater than 0.95. This requirement is also referred to as a cone cut. This requirement is applied to reduce the misidentification of a shower from a charged track. Fig. 3.7.3 shows the distribution of $\cos\theta$ for the six prong events in the $\psi(3770)$ data. The fraction of the good photons that are lost by this requirement can be estimated as follows: for an event that has six charged tracks and one photon; five charged tracks may have direction independent of that of the photon. Therefore, the probability of a charged track's falling into the rejective region is then given by

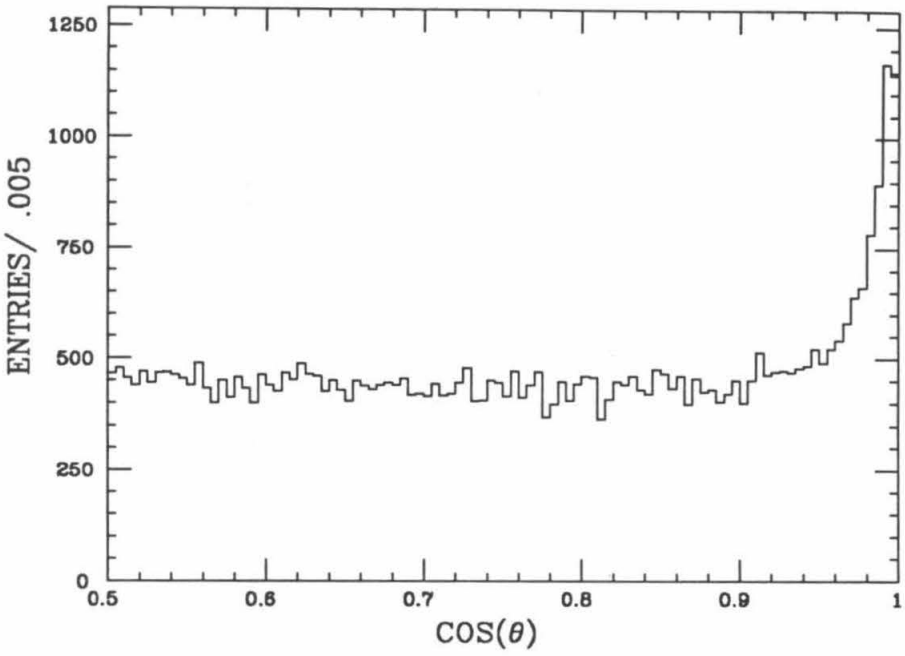

Figure 3.7.3: Misidentification of charged tracks as photons. cosθ is the *cos* of the angle between the charged track and the photon. There is a peak at 1 from the misidentification of charged tracks as photons.

$$P_{lost} \simeq 5 \times \frac{\Delta\Omega}{4\pi} \simeq 13.\% \quad . \tag{3.3}$$

A Monte Carlo test indicates that about 88% of the photons pass this requirement, consistent with this estimate.

4. The cosine of the angle between the shower axis and the direction of the photon should not be less than 0.8, or $\theta = 37^o$. The distribution of the cosine angle of photons from real $J/\psi \rightarrow \rho\pi^0$ events is shown in Fig. 3.7.4. The energy of the photons is defined in the same way as in the previous points. From Fig. 3.7.4, we can see the alignment of the shower axis, and the direction of the photon gets better with increasing energy.

5. The photon does not hit the joining parts of the end caps and barrel shower counters or the edge of the end caps. And finally,

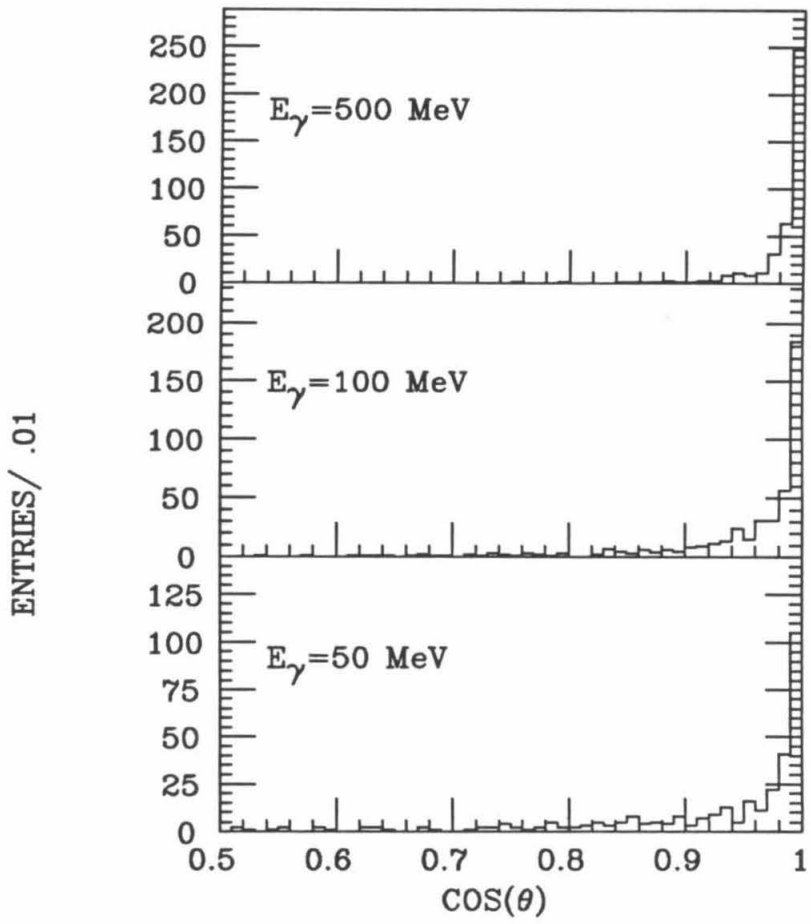

Figure 3.7.4: Alignment of the shower and momentum of photons. $\cos\theta$ is the *cos* of the angle between the direction of the photon and the direction of the shower axis.

6. the energy of the shower is also required to be greater than a minimum, the value of which depends on the nature of each analysis.

The efficiency of good photon identification is tested by using $J/\psi \rightarrow \rho\pi \rightarrow \pi^+\pi^-\pi^0$ events. Again, the true photon energy of the photons is determined from a 5C fit. The minimum energy of the photons is set at 30 MeV. Fig. 3.7.5 shows good photon detection efficiency.

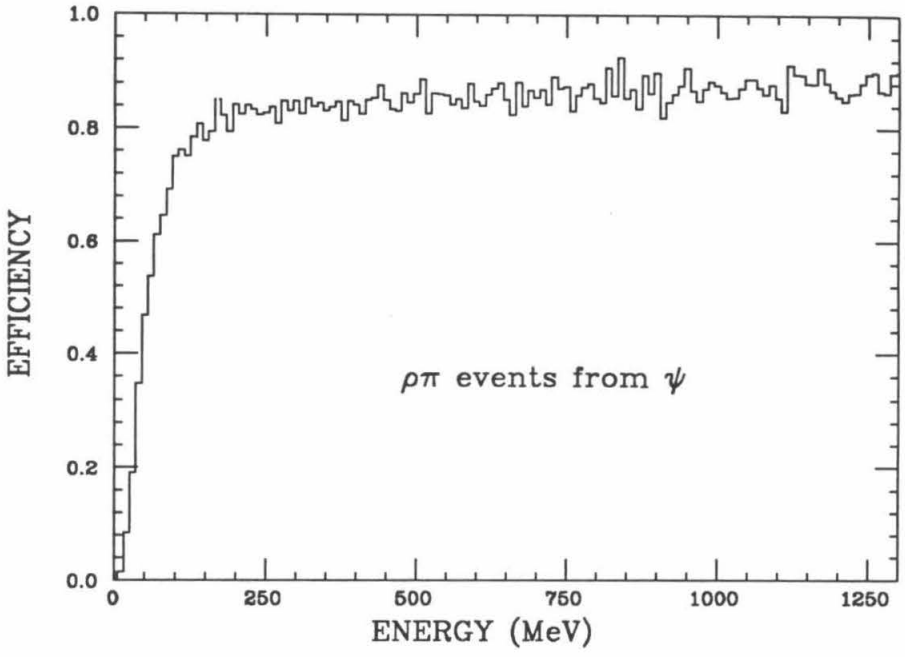

Figure 3.7.5: Good photon identification efficiency.

3.8 GOOD CHARGED TRACKS

Each event is required to have equal numbers of positive and negative charged tracks. A good charged track is a track originating in a cylinder centered at the beam interaction point with a radius of 2 cm and a length of 16 cm. A good charged track is required to have Z information and to have been "helix" fit.

4. HADRONIC TRANSITION $\psi(3770) \rightarrow J/\psi + \pi^+\pi^-$

4.1 Event Selection

Events that are candidates for reconstruction as $\psi(3770) \rightarrow J/\psi + \pi^+\pi^-$ and $J/\psi \rightarrow e^+e^-$ or $\mu^+\mu^-$ must meet several criteria. First, events must contain only good, charged tracks, two positive and two negative. Second, the events may contain no good photon with shower energy greater than 50 MeV. The events are then fitted to the hypothesis $\psi(3770) \rightarrow \pi^+\pi^-e^+e^-$ and $\psi(3770) \rightarrow \pi^+\pi^-\mu^+\mu^-$.

Each event may be fitted many times, because of the different hypotheses for decay processes and for the tracks. Momentum range restrictions and particle identification requirements are imposed on fitted tracks to further reduce the background levels and to guarantee the correct use of the tracks.

The tracks used as pions are required to have a momentum less than 900 MeV/c, since for signal, the pion momentum is less than 514 MeV/c. This cut affects only the events that the invariant mass of the two leptons is less than 2.7 GeV/c^2; therefore, it will be no bias on determining the continuum background.

The tracks used as leptons by the fitter must also be identified by a combination of E/P methods and muon counters. E here refers to the unfitted energy of the shower and P to the unfitted momentum of the tracks measured by the drift chamber. For the $\psi(3770) \rightarrow \pi^+\pi^-\mu^+\mu^-$ mode, each track used as a muon is required to satisfy $E \leq 0.4$ GeV and to have a two layer hit in muon counters if it is in the range of the muon system. For the $\psi(3770) \rightarrow \pi^+\pi^-e^+e^-$ mode, each track used as an electron is required to satisfy $E/P \geq 0.5c$. These cuts are looser than those used in Chapter 3, because the background that is due to misidentifications in this channel are low, while it is necessary to have higher efficiency.

The fourth requirement is that the total energy of the two pions be greater than 608 MeV, to reduce the initial state radiated $\psi(3685)$ background.

The major difference between this $\psi(3685)$ background and the signal we are seeking is in the sum of the total energy of the pions. The energy of the pions from signal reaction is greater than 623 MeV, while from initial state radiated $\psi(3685)$ events it is less than 588 MeV. There is thus at least 35 MeV energy difference between the signal and initial state radiated $\psi(3685)$ background. The energy resolution for the pions is the same as or better than the momentum resolution. The energy resolution can be estimated as:

$$\Delta p = p \times 0.015 \times \sqrt{1+p^2} \leq 10\ MeV/c \tag{4.1}$$

with $p = 600\ MeV/c$ or:

$$\Delta E \leq 10\ MeV\ . \tag{4.2}$$

Taking advantage of the energy difference and the resolution of the energy measurement, by requiring the total energy of the two pions to be greater than 608 MeV, we can achieve a clear separation (better than 2σ cut on rejecting initial state radiated $\psi(3685)$ background) between the initial state radiated $\psi(3685)$ background and the signal with little loss in efficiency.

The total energy of the two pions is shown in Fig. 4.1.1. The dotted line is the $\psi(3685)$ background distribution calculated by Monte Carlo with the pions uniform by distributed in phase space. The solid line is the Monte Carlo signal with the two pions also having a uniform phase space distribution. The histogram is the real data. Fig. 4.1.1 shows a clear separation between the signal and the background from initial state radiation from $\psi(3685)$.

The fifth step is to reject background from radiative Bhabha scattering, which arises when the photon converts into an electron positron pair and is then misidentified as pions. We require that the two lowest momentum tracks have an invariant mass greater than 50 MeV/c^2, when they are assumed to be electron positron pairs, thereby eliminating this source of background.

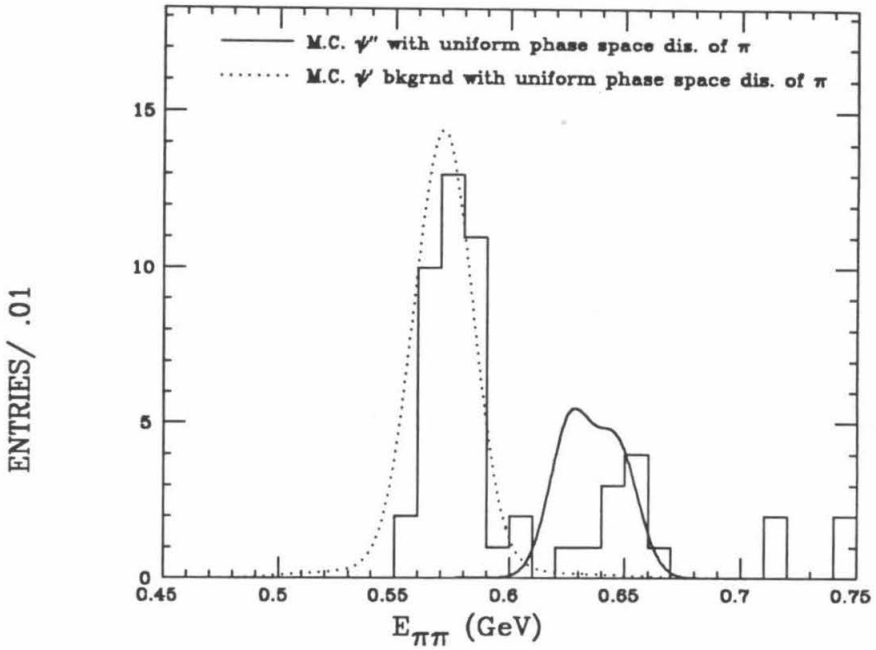

Figure 4.1.1: $E_{\pi^+\pi^-}$ from hadronic transition.

The last step requires the minimum χ^2−probability of the 4C fit to be greater than 1 % .

Finally, the invariant masses of the two leptons is shown in 4.1.2, and the correlation of the invariant masses and the χ^2−probability is shown in Fig. 4.1.3. Nine events are good signal candidates; five of these contain $J/\psi \to \mu^+\mu^-$; four contain $J/\psi \to e^+e^-$.

Before making the cut on total energy of the two pions, we can use the information on the two pions to calculate the mass of the initial state:

$$\begin{aligned} M_{initial\ state} &= \sqrt{(E_{\pi^+\pi^-} + E_{J/\psi})^2 - (\vec{P}_{\pi^+\pi^-} + \vec{P}_{J/\psi})^2} \\ &\simeq E_{\pi^+\pi^-} + E'_{J/\psi} + O(10\ MeV)\ (for\ \psi(3685)\ and\ \psi(3770)). \end{aligned} \tag{4.3}$$

Here, $E'_{J/\psi} = \sqrt{M^2_{J/\psi} + P^2_{\pi^+\pi^-}}$, and $P_{\pi^+\pi^-}$ is the momentum of the two-pion system. Fig. 4.1.4 shows the initial state mass distribution. We can clearly see the separation between the $\psi(3685)$ and $\psi(3770)$ events.

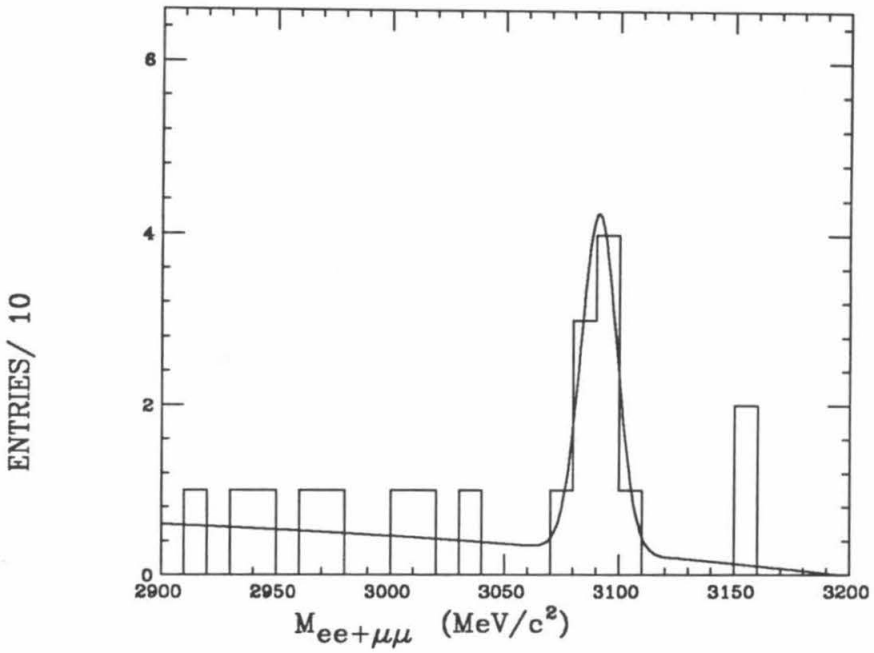

Figure 4.1.2: $M_{l^+l^-}$ in hadronic transition.

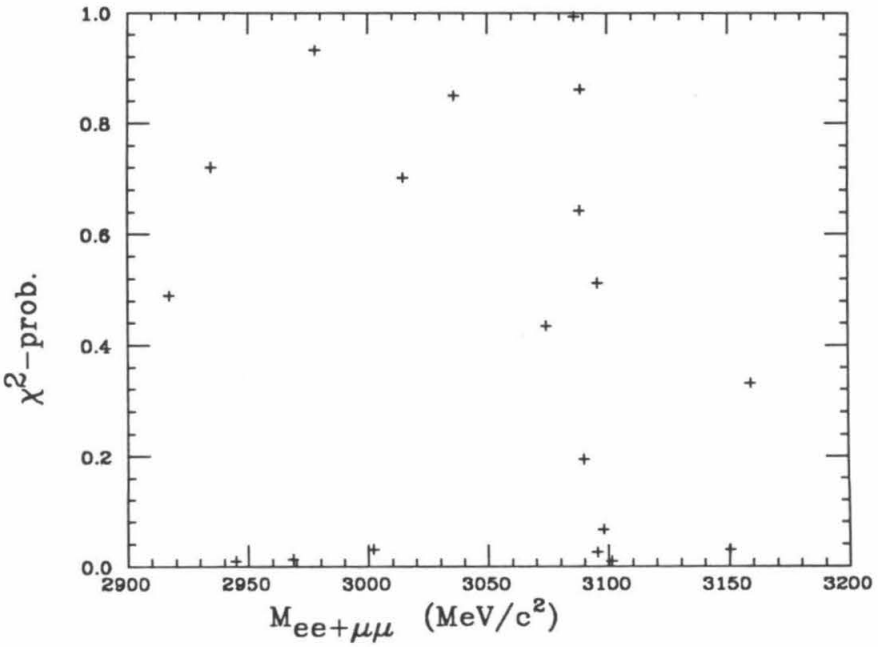

Figure 4.1.3: $M_{l^+l^-}$ vs. χ^2−probability .

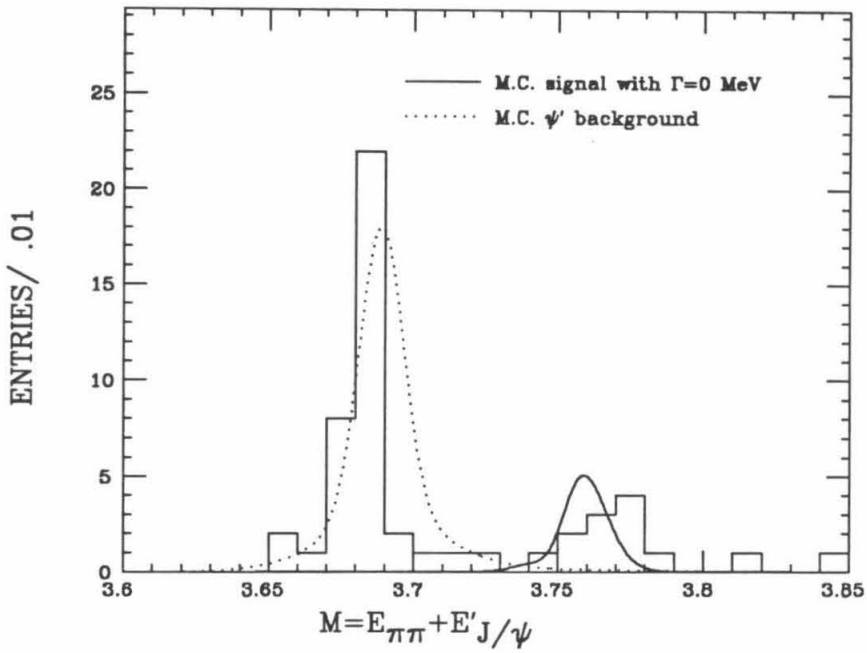

Figure 4.1.4: Initial state masses from the information of the two pions.

The shape of the Monte Carlo-predicted curves are different from the measured data for a number of reasons: a) For the $\psi(3770)$, the Monte Carlo events are generated with $\Gamma_{\psi(3770)} = 0$, while the real $\psi(3770)$ has a full width of 25 MeV. In fact, in this data sample, the shape of the $\psi(3770)$ resonance is determined by the energy at which the data were taken; b) For the $\psi(3685)$, the Monte Carlo events are generated with two pions uniformly distributed in phase space. The data, however appear more like a two–body decay distribution with $M_{\pi^+\pi^-}$ peaked at high mass. The energy of the J/ψ is approximated by

$$\begin{aligned} E'_{J/\psi} &= \sqrt{M^2_{J/\psi} + (\vec{P}_{\pi^+\pi^-} + \vec{P}_\gamma)^2} \\ &\simeq \sqrt{M^2_{J/\psi} + (\vec{P}_{\pi^+\pi^-})^2}, \end{aligned} \tag{4.4}$$

and will be smaller if $P_{\pi^+\pi^-}$ is peaked lower than that given by a uniform distribution.

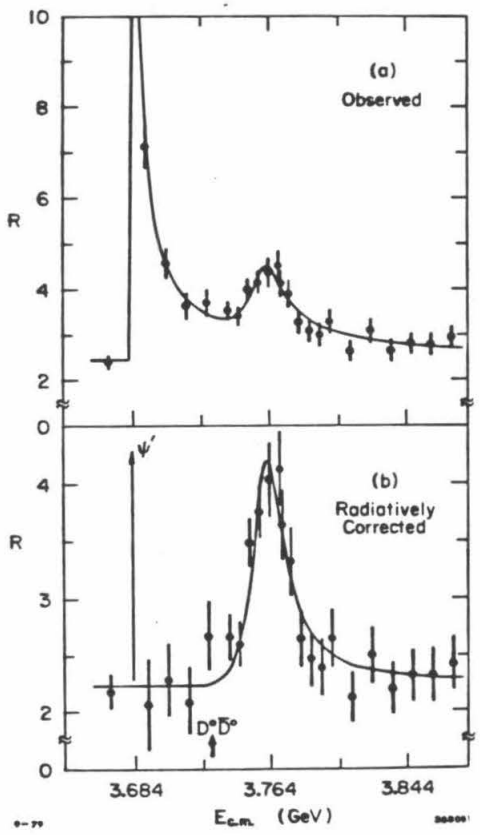

Figure 4.2.1: $R = \frac{\sigma(Hadrons)^{87}}{\sigma(\mu^+\mu^-)}$.

4.2 NUMBER OF $\psi(3685)$ EVENTS IN THIS DATA SAMPLE

The ratio R, the total hadronic cross section scaled to the muon pair cross section, has been measured by a number of groups. Fig. 4.2.1 shows the measured R at different center of the mass energies. We can see that the $\psi(3770)$ sits on the radiative tail of the $\psi(3685)$; the $\psi(3685)$ is therefore a major source of background. In this section, the determination of the total number of $\psi(3685)$ background events in this data sample is summarized.

The $\psi(3685)$ events are reconstructed from the decay $\psi(3685) \rightarrow \pi^+\pi^- J/\psi$; $J/\psi \rightarrow l^+l^-$. The reconstruction is the same as for the $\psi(3770) \rightarrow \pi^+\pi^- J/\psi$;

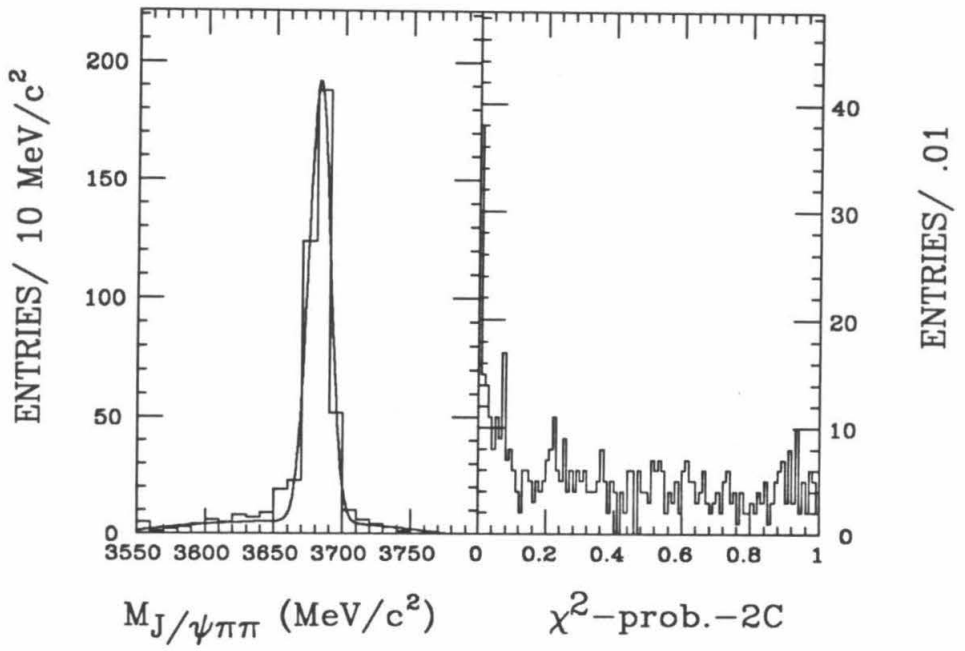

Figure 4.2.2: Reconstruction of the $\psi(3685)$.

$J/\psi \to l^+l^-$ except that:

1. Good photons are allowed in each event;
2. The fit is to the hypothesis $e^+e^- \to (missing-\gamma)\pi^+\pi^- J/\psi; J/\psi \to l^+l^-$;
3. There is no requirement on the total energy of the pions;
4. This is a 2C fit instead of a 4C fit. One constraint comes from the mass constraint of the J/ψ , and another comes from requiring the missing energy to be equal to the missing momentum in order to ensure that it is a missing photon.

Fig. 4.2.2 shows the invariant mass of the $J/\psi\pi^+\pi^-$ system and the χ^2-probability distribution. The $\psi(3685)$ resonance is clear and has a small background.

The efficiency $\epsilon_{\psi(3685)}$ of the reconstruction for the $\psi(3685)$ events is deter-

mined from Monte Carlo:

$$\epsilon_{\psi(3685)} = 0.50 \pm 0.05. \tag{4.5}$$

There are a total of 361 ± 21 $\psi(3685)$ events observed. The total number of the $\psi(3685)$ events are:

$$\begin{aligned} N_{\psi(3685)} &= \frac{361 \pm 21}{\epsilon_{\psi(3685)} \times Br(\psi(3770) \to \pi^+\pi^- J/\psi) \times Br(J/\psi \to l^+l^-)} \\ &= (16.0 \pm 0.9 \pm 2.1) \times 10^3 \ . \end{aligned} \tag{4.6}$$

The large systematic error is dominated by the uncertainty in $B(J/\psi \to l^+l^-)$.

4.3 BACKGROUND

As mentioned earlier, the major source of the background is from $\psi(3685)$:

$$e^+e^- \to \gamma\psi(3685); \quad \psi(3685) \to J/\psi\pi^+\pi^-. \tag{4.7}$$

In this process, an electron (a positron) radiates a photon of 84 MeV and annihilates with a positron (an electron) to form a $\psi(3685)$. The $\psi(3685)$ then radiates two pions, becoming a J/ψ, and the J/ψ decays into lepton pairs.

Most $\psi(3685)$ background can be rejected by the 4C SQUAW fit and by requiring no good photon to be found. Some events are not rejected by the fit because of poor track measurements and because of having a large fraction of the radiated photons pointing along the beam direction.[42]

The additional cut on the total raw energy of the two pions rejects almost all $\psi(3685)$ events; the combination of the fit and the cut on the total raw pion energy leaves essentially no $\psi(3685)$ background in the final results. This is confirmed by a Monte Carlo calculation (see Fig. 4.3.1). In the Monte Carlo test, the radiated photon is generated following the predicted distribution[42]. 5,000 events

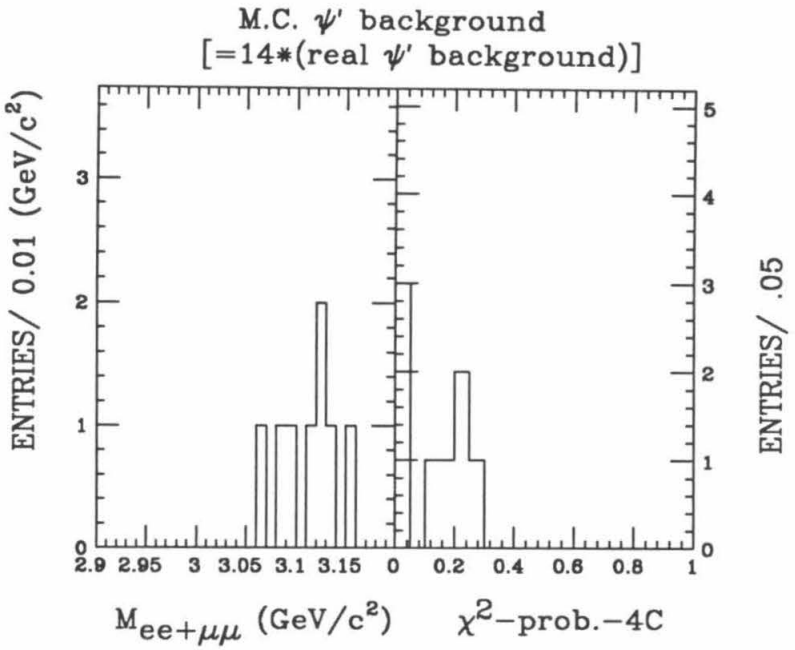

Figure 4.3.1: M.C. tests for rejecting initial state radiated $\psi(3685)$

are generated in the electron mode and 5,000 in the muon mode. This is 14 times the number of expected background events. Four events fall into the signal region. The $\psi(3685)$ background contribution is thus 0.29 ± 0.15 events. The continuum background determined from Fig. 4.1.2 is about 1.4 events. The total background contribution is therefore about 1.7 events.

4.4 Efficiency and Resolution

The mass resolution for lepton pairs, calculated by Monte Carlo, is 7 MeV shown by the solid curve in Fig. 4.4.1. Since, as mentioned earlier, a number of kinematic cuts are made to reduce the background level, it is important to determine the effects of these cuts on the efficiency as a function of the invariant mass of the lepton pairs. The histogram in Fig. 4.4.1 shows this efficiency. There, the events of the type

$$e^+e^- \rightarrow \pi^+\pi^- X; X \rightarrow \mu^+\mu^- \tag{4.8}$$

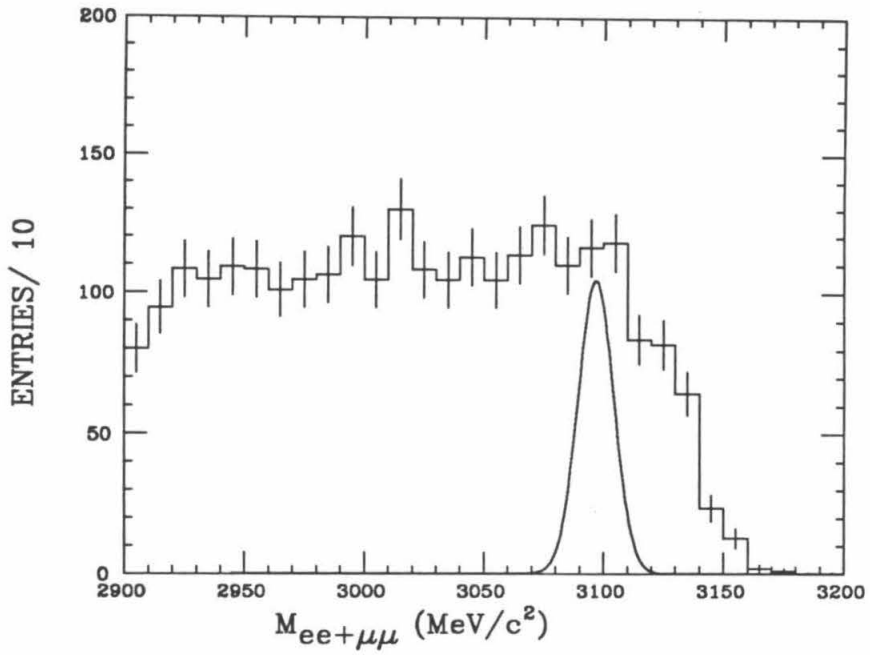

Figure 4.4.1: Resolution and efficiency from Monte Carlo tests.

are generated with masses X from 2.8 to 3.4 GeV/c^2 with a spacing of 5 MeV/$c^2$and 100 events per entry. The histogram in Fig. 4.4.1 indicates that the efficiency for X with mass 2.9 to 3.1 GeV/c^2 is flat. The muon detection efficiencies are determined from di–muon events in this data sample. The fact that the efficiencies are close to two constants for muons with momentum greater than 1 GeV is used. The muon identification efficiencies are 96% in the muon counter covered region and 98% outside the muon counter covered region. The over all reconstruction efficiency is $\epsilon = 0.51 \pm 0.03$.

4.5 Systematic Errors

Systematic errors arise from a number of sources:

1. The mass distribution of the two pions is assumed to be uniform for the Monte Carlo. The actual distribution is unknown. For a uniform phase space distribution, $\epsilon = 0.51$, while for the distribution predicted by Yan[16], $\epsilon = 0.52$.

2. Monte Carlo simulation is not accurate for large angle charged tracks (10%).
3. How the background is determined (10%).
4. There is about a 13% error on the measured branching ratios of $J/\psi \rightarrow l^+l^-$.

The total systematic error is estimated to be 20%.

4.6 BRANCHING RATIO

We are now ready to determine the branching ratio. The efficiency of the reconstruction is $\epsilon_{program} = 0.51 \pm 0.03$. The number of signal events N_s is 9 and the number of background events N_b is 1.7. The total luminosity $L = 9300 \pm 150\ nb^{-1}$. Therefore,

$$\begin{aligned}\sigma_{\psi''} \times Br(\psi'' \rightarrow \pi^+\pi^- J/\psi) &= \frac{N_s - N_b}{L \times \epsilon_{reconstruction} \times Br(J/\psi \rightarrow l^+l^-)} \\ &= (1.1 \pm 0.5 \pm 0.2) \times 10^{-2}.\end{aligned} \tag{4.9}$$

Table 4.I lists the partial width for different total cross sections of the $\psi(3770)$.

$\sigma_{\psi(3770)}$ (nb)	$\Gamma(\psi(3770) \rightarrow \pi^+\pi^- J/\psi)$ (keV)	$Br(\psi(3770) \rightarrow \pi^+\pi^- J/\psi)$ $(\times 10^{-3})$
5.00^{5}	55. $\pm$23. $\pm$11.	2.2 $\pm$0.9 $\pm$0.4
6.75^{39}	41. $\pm$17. $\pm$8.	1.6 $\pm$0.7 $\pm$0.3
9.3^{37}	30. $\pm$12. $\pm$6.	1.2 $\pm$0.5 $\pm$0.2

Table 4.I. Partial widths and branching ratios of $\psi(3770) \rightarrow J/\psi\pi^+\pi^-$.

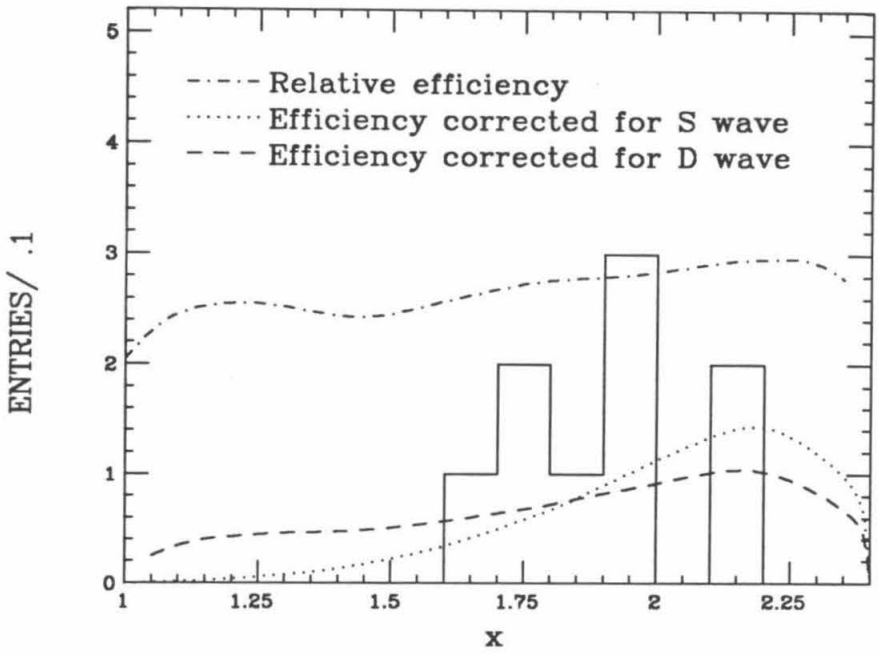

Figure 4.7.1: The distribution of $x = \frac{M_{\pi^+\pi^-}}{2M_{\pi^\pm}}$.

4.7 THE MASS AND ANGULAR DISTRIBUTIONS OF $\pi^+ - \pi^-$ SYSTEM

The mass distribution of the two pions is given by Eq. 1.54, Eq. 1.56 and Eq. 1.72. The angular distribution of the two–pion system is given by Eq. 1.57.

Comparisons between the predicted and measured mass distribution of the two pions are shown in Fig. 4.7.1.

Fig. 4.7.2 shows the distribution of the momentum of the two-pion system with respect to the beam direction. Dotted line represents the reconstruction efficiency determined by the Monte Carlo. According to Eq. 1.57, the expected distribution should be almost flat and therefore parallel to the dotted line.

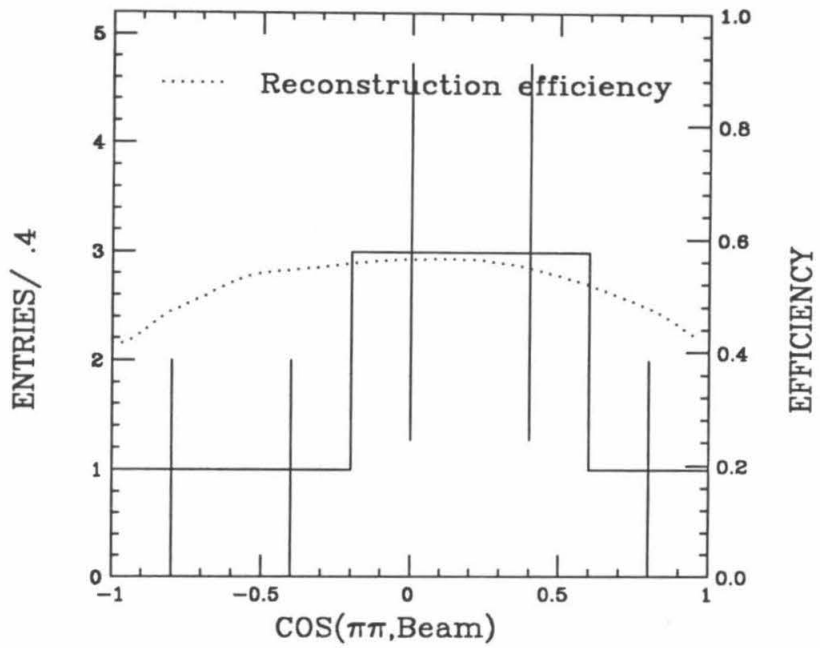

Figure 4.7.2: The cosine of the angle between the momentum of the two pion system and the beam direction.

4.8 CONCLUSION

The decay $\psi(3770) \rightarrow J/\psi\pi^+\pi^-$ has been observed. The cross section times the branching ratio is found to be:

$$\sigma_{\psi(3770)} \times Br(\psi(3770) \rightarrow \psi\pi^+\pi^-) = (1.1 \pm 0.5 \pm 0.2) \times 10^{-2}\ nb. \qquad (4.10)$$

The branching ratio is in the range from 1×10^{-3} to 2×10^{-3}, and the partial width is in the range from 30 to 55 keV, depending on the value used for $\sigma_{\psi(3770)}$. For more details, see table 4.I.

It is also found that there are $(16.0 \pm 0.9 \pm 2.1) \times 10^3$ $\psi(3685)$ events in this $\psi(3770)$ sample. The production cross section is therefore:

$$\sigma_{\psi(3685)}(at\ 3.77\ GeV) = 1.7 \pm 0.1 \pm 0.2\ nb. \qquad (4.11)$$

Within statistical errors, the predictions for the angular distribution (Eq.

1.57) are consistent with these measurements. The limited statistics made it difficult to distinguish between the two–pion mass distribution predicted by Eq. 1.54 and 1.56.

5. ELECTROMAGNETIC TRANSITIONS

5.1 INTRODUCTION

The $\psi(3770)$ can also radiate a photon and decay into the χ_J states. The branching ratios for the four major decays of the χ_J states are listed in Table 5.I. In this analysis, the χ_J states are reconstructed in three modes:

1. $\chi_J \to \gamma J/\psi;\ \ J/\psi \to \mu^+\mu^-$
2. $\pi^+\pi^-\pi^+\pi^-$
3. $\pi^+\pi^-\pi^+\pi^-\pi^+\pi^-$.

Decay processes	Branching ratio (%)
$\chi_0 \to \pi^+\pi^-\pi^+\pi^-$	3.8±0.8
$\chi_0 \to \pi^+\pi^- K^+K^-$	2.9±0.8
$\chi_0 \to \pi^+\pi^-\pi^+\pi^-\pi^+\pi^-$	1.5±0.5
$\chi_0 \to \gamma J/\psi(3097)$	0.7±0.2
$\chi_1 \to \gamma J/\psi(3097)$	25.8±2.5
$\chi_1 \to \pi^+\pi^-\pi^+\pi^-\pi^+\pi^-$	2.2±0.9
$\chi_1 \to \pi^+\pi^-\pi^+\pi^-$	1.7±0.5
$\chi_1 \to \pi^+\pi^- K^+K^-$	0.9±0.4
$\chi_2 \to \gamma J/\psi(3097)$	14.8±1.7
$\chi_2 \to \pi^+\pi^-\pi^+\pi^-$	2.2±0.5
$\chi_2 \to \pi^+\pi^- K^+K^-$	1.9±0.5
$\chi_2 \to \pi^+\pi^-\pi^+\pi^-\pi^+\pi^-$	1.1±0.8

Table 5.I. The major decays of the χ_J [2].

The decay mode $\chi_J \to K^+K^-\pi^+\pi^-$ is not reconstructed here because of the

large D meson background .

5.2 KINEMATICS OF THE DECAY PROCESSES

Table 5.II shows the predicted angular distributions of the γ and the velocities of the χ_J in laboratory frame. The angular distributions of the γ from the decay $\psi(3770) \rightarrow \gamma\chi_J$ are the same as those for $\psi(3685)$ [41,20].

Decay Process	$J^{PC}(\chi_J)$	Pred. dis. (γ)	E_γ(MeV)	β_{χ_J}
$\psi(3770) \rightarrow \gamma\chi_0(3415)$	0^{++}	$1+\cos^2\theta$	338.4	0.0986
$\psi(3770) \rightarrow \gamma\chi_1(3510)$	1^{++}	$1-\frac{1}{3}\cos^2\theta$	250.4	0.0711
$\psi(3770) \rightarrow \gamma\chi_2(3555)$	2^{++}	$1+\frac{1}{13}\cos^2\theta$	207.6	0.0583

Table 5.II. The predicted angular distributions[41].

5.3 ANALYSIS OF $\chi_J \rightarrow \gamma J/\psi$; $J/\psi \rightarrow \mu^+\mu^-$

Events selection

In this analysis, the J/ψ is reconstructed from muon pairs. The decay $J/\psi \rightarrow e^+e^-$ is not used, because of the large radiative Bhabha background.

Two good charged tracks with opposite signs are required in each event. They are required to satisfy E $\leq$0.3 GeV, which is tighter than in the earlier analysis in order to more effectively reject radiative Bhabha background. Each charged track is also required to have at least one layer hit in the muon counter if it is in the direction covered by the muon counter.

Two "good photons" are required in each event, each with measured shower energy greater than 50 MeV. A "good photon" is a shower measurement that satisfies a set of criteria, given in Chapter 3. The requirement of two and only two "good photons" is necessary to achieve a good signal–to–noise ratio.

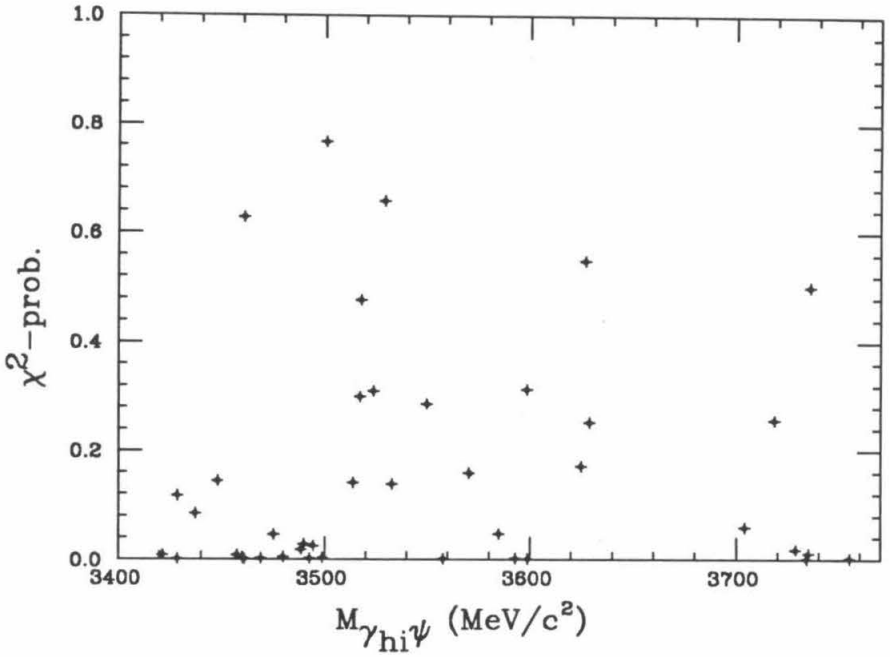

Figure 5.3.1: $M_{\gamma_{hi}J/\psi}$ vs. χ^2−probability of the 5C fit.

The events passing all cuts are fit to hypothesis $\psi(3770) \rightarrow 2\gamma J/\psi$; $J/\psi \rightarrow \mu^+\mu^-$. This is a 5C fit, 1C coming from the mass constraint of the J/ψ and 4C from the four momentum constraints. In the fit, the photons used by the fitter must be those identified as good photons. Events with χ^2−probability of the fit greater than 10% are retained.

Fig. 5.3.1 shows the invariant mass of the higher energy photon with the J/ψ vs. χ^2−probability of the 5C fit. The signal candidates are those with $M_{\gamma_{hi}J/\psi} \sim 3510$ MeV. The χ^2−probability for these candidates is almost flat. Most background events have χ^2−probability less than 10% . The background has smaller χ^2−probability , since there is no direct decay process of the $\psi(3770)$ into $2\gamma + J/\psi$ with a notable branching ratio, and most of the background therefore arises from events with more than two photons, or with tracks that are not muons.

Since each event has two photons, it is necessary to determine which is the correct one to combine with J/ψ to reconstruct the χ_J . For the χ_1 and χ_2 , the photon energies radiated by the χ_J are larger than those radiated by the

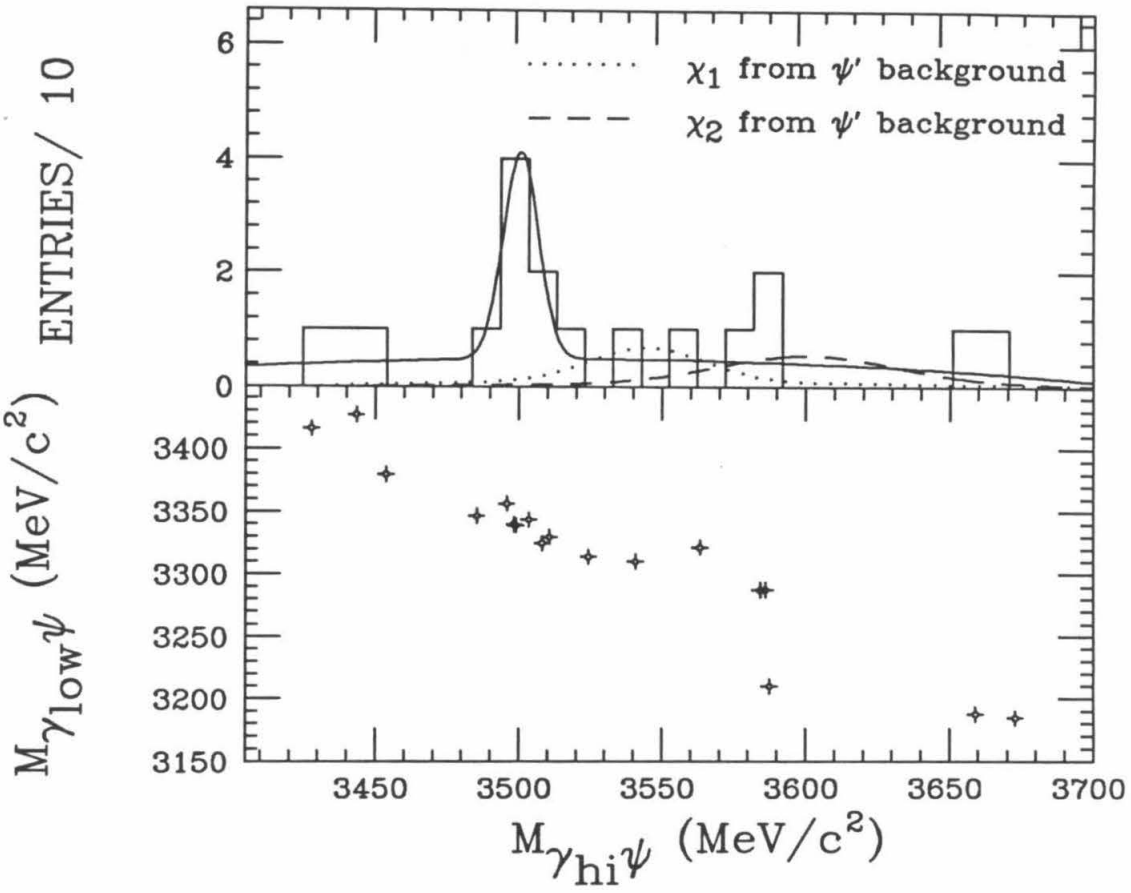

Figure 5.3.2: $M_{\gamma_{hi}J/\psi}$ from the 5C fit.

$\psi(3770)$. The photon with the higher fitted energy is therefore used. For the χ_0 , the situation is more complicated. This is not, however, expected to be observable, because of the small branching ratio.

The fitted masses are shown in Fig. 5.3.2. The quantity $M_{\gamma_{hi}J/\psi}$ is the invariant mass of the higher energy photon and J/ψ . There, $M_{\gamma_{lo}J/\psi}$ is the invariant mass of the lower energy photon and the J/ψ . The dotted line is for the χ_1 , and the dashed line is for the χ_2 produced by initial state radiation from the $\psi(3685)$.

Background

The initial state radiation $\psi(3685)$ events are the major background. Each such event contains three photons, one from the initial state radiation, one from the $\psi(3685)$, and one from the χ_J. This background is rejected by detailed consideration of the angles between the initial state photon and the other photons or the direction of the beam:

1. If three photons are well identified, the event is rejected by the cut requiring no more than two good photons.
2. If only two good photons are found, and the missing one is not in the same direction as these two, then the calculated mass of the χ_J will shift to a higher value.
3. If the initial state photon and the photon from χ_J are in the same direction, this background will have a different mass distribution from the signals.
4. If the initial state photon is in the same direction as the photon from the $\psi(3685)$, there is no distinction between this background and the signal. It will therefore not be rejected.

Only the last situation provides a major potential source of indistinguishable background. However, since the probability of the two photons' being in the same direction is small, this background is negligible. The total number of the $\psi(3685)$ events in this data sample is about 16×10^3. Two photons can be separated from each other when $\cos(\theta_{\gamma_1,\gamma_2}) \leq 0.95$ and only about 30% of the initial state photons escape the beam pipe. The detection and reconstruction efficiency is about 50% . The number of background events from this source is thus:

$$N_{\chi_J} = 16\times10^3 \times \frac{0.05}{2} \times 0.3 \times 0.5 \times Br(\psi(3685) \rightarrow \gamma\chi_J) \times Br(\chi_J \rightarrow \gamma J/\psi). \quad (5.1)$$

For the three χ_J states, the result is:

$$N_{\chi_0} = 0.0 \quad (5.2)$$

$$N_{\chi_1} = 1.3 \tag{5.3}$$

$$N_{\chi_2} = 0.7\ . \tag{5.4}$$

The overall $\psi(3685)$ background contributions are determined by using a Monte Carlo simulation method. The initial state photon has an angular distribution generated according to the prediction of Ref.(42). 2000 events are generated for each χ_J with $J = 0,\ 1,\ 2$. This is about 100 times more events than there are in the real background. The χ^2-probability distribution and the invariant masses distribution of χ_J are shown in Fig. 5.3.3. The widths of the χ_1 and χ_2 from the $\psi(3685)$ are much broader than those from the $\psi(3770)$. The masses of the χ_1 and χ_2 are also shifted up by about 40 MeV/c^2. Most events are peaked at the small χ^2-probability region. Fig. 5.3.3 also indicates that requiring χ^2-probability greater than 10% very effectively reduces the $\psi(3685)$ background.

Finally, the $\psi(3685)$ and continuum background contributions N_b are listed in Table 5.III. The continuum background is determined by a polynomial fit on the continuum background.

Efficiency

The reconstruction efficiencies are determined by using a combination of Monte Carlo generated and real di–muon events. The Monte Carlo method is first used to determine the reconstruction efficiencies without muon identification. The Monte Carlo events are generated with a uniform phase space distribution. Since the real events are not generated with a uniform phase space distribution, errors due to the angular dependence are expected. The correction to the angular dependence of the radiated photon of the $\psi(3770)$ has been made according to Table 5.II. The errors that are due to the angular distribution of the radiated photon of the χ_J are included in systematic errors. These errors are small (a few percent compared with the statistical errors of 50%). Then, the muon identification efficiency is determined from the real di-muon events, using the fact

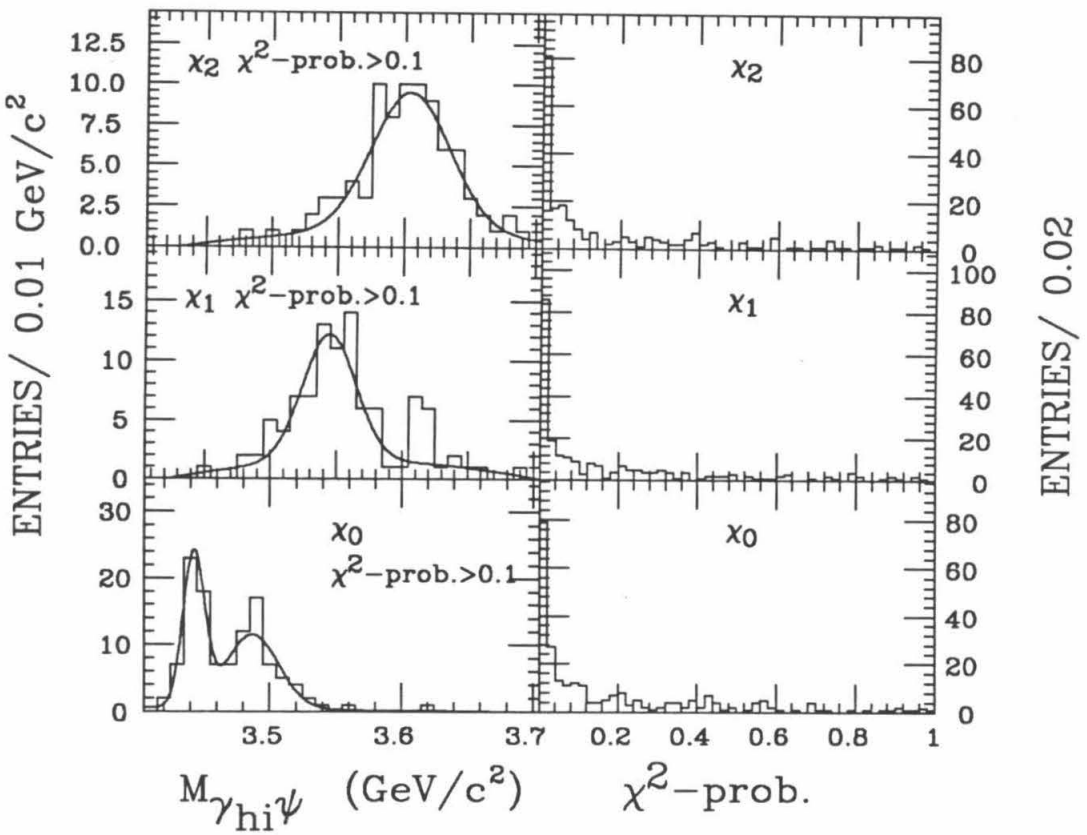

Figure 5.3.3: Monte Carlo simulations of initial state radiated $\psi(3685)$ background.

that the efficiency is flat for muons with momentum greater than 1 GeV. The muon identification efficiencies are 90% in the muon counter covered region and 92% outside the muon counter–covered region. The reconstruction efficiencies ϵ_s are listed in Table 5.III.

A check has been made to find out whether the kinematic cuts had introduced a bias in selecting events. Such a bias could result in an incorrectly estimated background level, especially for continuum background. A set of Monte Carlo events are generated with masses of $M_{\gamma J/\psi}$ uniformly distributed from 3.45 GeV to 3.70 GeV. If the detection and reconstruction efficiency have a bias, then the resulting distribution will not be uniform. The results of the Monte Carlo tests

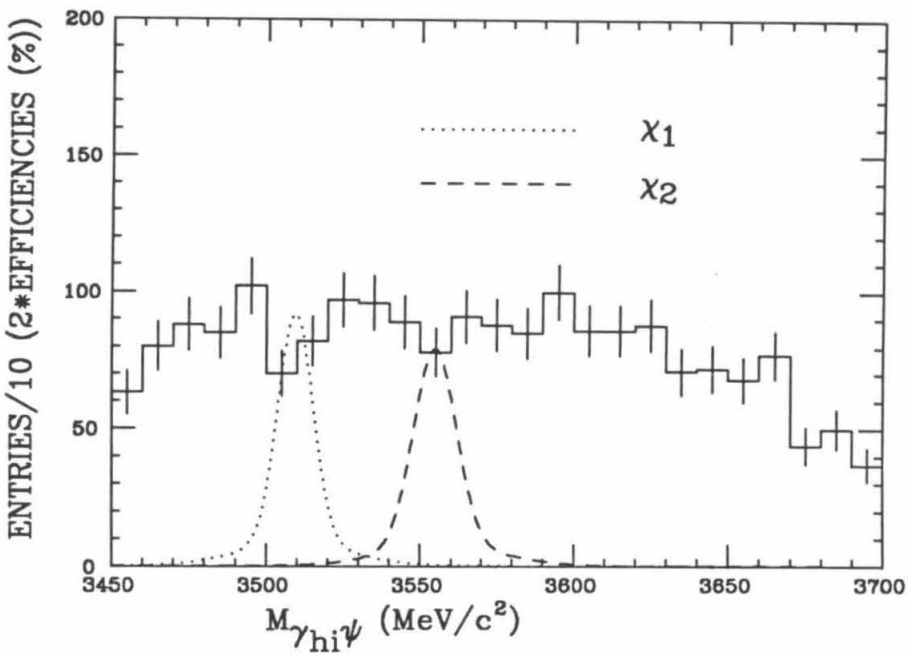

Figure 5.3.4: Efficiencies and resolutions of $M_{\gamma_{hi}J/\psi}$.

shown in Fig. 5.3.4 indicate that the efficiency is a smooth curve from 3.45 GeV to 3.7 GeV.

In the Monte Carlo simulation, the photon showers are generated by using a "fake–shower" method. Only the energy, the shape distributions of the showers, are generated. Comparing the fake photons with these from data on the decay $J/\psi \to \rho\pi \to \pi^+\pi^-\pi^0$, the major differences are the energy distributions and the detailed shapes of the shower at the ribs and the edges of the shower counters. This can introduce an error less than 10% in efficiency, which is included in the systematic errors.

Branching ratios

From the number of events N_s, the background N_b, the reconstruction efficiency ϵ_s, the total luminosity L and the branching ratios $Br(\chi_J \to \gamma J/\psi)$, the cross section times the branching ratios are:

States	Num. of Candidates	N_b	ϵ_s (%)	$\sigma_{\psi(3770)} \times Br(\psi(3770) \rightarrow \gamma\chi_J)$
χ_1	8.0	2.4	41.	$(8.3 \pm 4.2 \pm 1.5) \times 10^{-2}$ (nb)
χ_2	2.0	1.0	39.	$\leq 1.4 \times 10^{-1}$ nb (at 90% C.L.)

Table 5.III: χ_J branching ratios from $\gamma J/\psi$.

The statistical errors are determined by the number of signal candidates of the signals. For the state χ_1 , this will be $\sqrt{8}$ counts or $\sqrt{8}/(8.0-2.4) \simeq 51\%$. The systematic errors are dominated by the errors on the branching ratio of the $J/\psi \rightarrow \mu^+\mu^-$ (13%) and $\chi_J \rightarrow \gamma J/\psi$ (10%) and the difference between the Monte Carlo and real event distributions, especially for photons, which is also about 10% . In this analysis, the statistical errors are much larger than the systematic errors, which total 19% .

An upper limit for the decay $\psi(3770) \rightarrow \eta J/\psi$ can also be determined from this analysis. Monte Carlo calculations show the efficiency for reconstruction of the processes

$$\psi(3770) \rightarrow \eta J/\psi;\ \eta \rightarrow \gamma\gamma;\ J/\psi \rightarrow \mu^+\mu^- \tag{5.5}$$

to be 45 % . There is one event that is a candidate for this decay (see Fig. 5.3.6 with $M_{\gamma\gamma}$ around 549 MeV/c^2). Using the branching ratios from Ref.(2), the upper limit is determined to be:

$$\sigma_{\psi(3770)} \times Br(\psi(3770) \rightarrow \eta J/\psi) \leq 3.5 \times 10^{-2}\ nb\ at\ 90\%\ C.L.. \tag{5.6}$$

The angular distributions

The predicted angular distribution of the photon radiated by the $\psi(3770)$ relative to the beam direction is listed in Table 5.II. The comparison with the data is shown in Fig. 5.3.5. The prediction and the experimental measurements are consistent with one another.

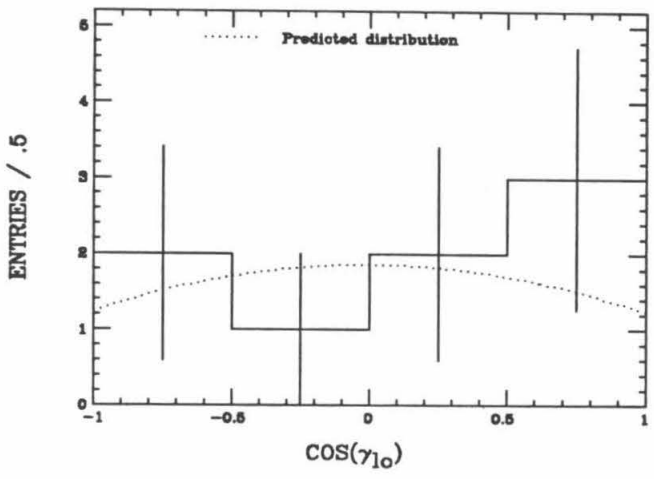

Figure 5.3.5: Angular distribution of the γ_{hi}.

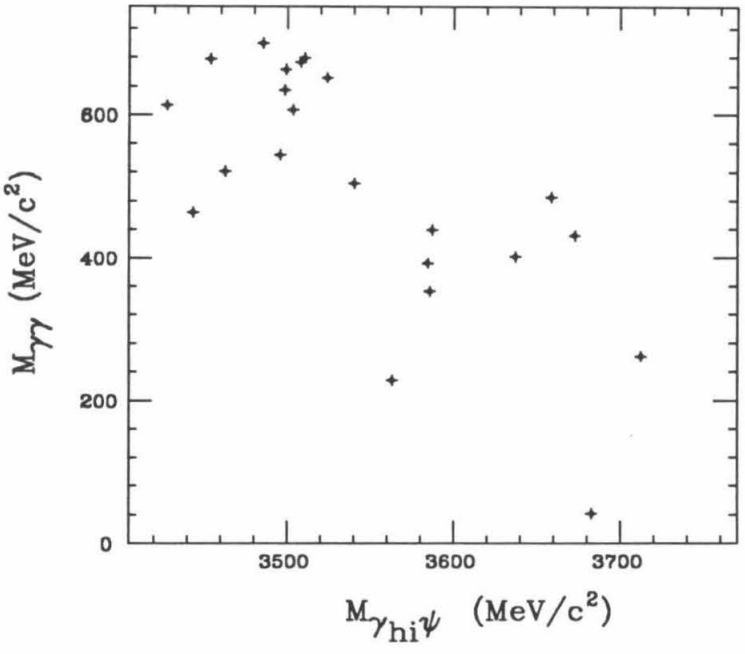

Figure 5.3.6: $M_{\gamma_{hi}J/\psi}$ vs. $M_{\gamma\gamma}$.

5.4 ANALYSIS OF $\psi(3770) \to \gamma\chi_J; \chi_J \to \pi^+\pi^-\pi^+\pi^-$

$\pi^+\pi^-\pi^+\pi^-$ is the largest decay mode of the χ_0 (see Table 5.I). All charged tracks in the event are identical, making it is relatively easier to reject background

than the case for non–identical particles. As in the earlier analysis, the major difficulty in this analysis is the $\psi(3685)$ background.

Events selection for $\psi(3770) \rightarrow \gamma\pi^+\pi^-\pi^+\pi^-$

Each event is required to have four good charged tracks, with none identified as an electron, muon , kaon or proton. No more than one good photon with shower energy greater than 50 MeV is permitted.

The electron identification is based mainly on the E/P method. ToF plays only a very small role in this analysis, since the mean momentum of the pions is about 800 MeV/c.

Muon candidates are those associated with two muon-layer hits. In the momentum range of this analysis, very few tracks are misidentified as muons.

Details of the particle identification have been discussed in Chapter 3.

A cut on the initial state masses reconstructed from pion pairs is used to reduce the $\psi(3685)$ hadronic transition background that is due to the processes: $e^+e^- \rightarrow \gamma\psi(3685)$; $\psi(3685) \rightarrow \pi^+\pi^- J/\psi$; $J/\psi \rightarrow l^+l^-$, where the leptons are misidentified as pions. Using the two pions as in Chapter 4, we can calculate the mass of the initial state:

$$\begin{aligned} M_{initial\ state} =& \sqrt{(E_{\pi^+\pi^-} + E_{J/\psi})^2 - (\vec{P}_{\pi^+\pi^-} + \vec{P}_{J/\psi})^2} \\ \simeq& E_{\pi^+\pi^-} + E'_{J/\psi} + O(10\ MeV)\ (for\ \psi(3685)\ and\ \psi(3770)). \end{aligned} \tag{5.7}$$

Here, $E'_{J/\psi} = \sqrt{M^2_{J/\psi} + P^2_{\pi^+\pi^-}}$, and $P_{\pi^+\pi^-}$ is the momentum of the two–pion system. The difference between this procedure and in Chapter 4 is the track selection. Only events containing two pairs, one of which has two opposite charged tracks with momentum greater than 1000 MeV/c, and the other with momentum less than 600 MeV/c, are background candidates. Fig. 5.4.1 shows this mass distribution. There is a clear $\psi(3685)$ signal structure. Any events in the region around $\psi(3685)$ mass $\pm$20 MeV will be rejected.

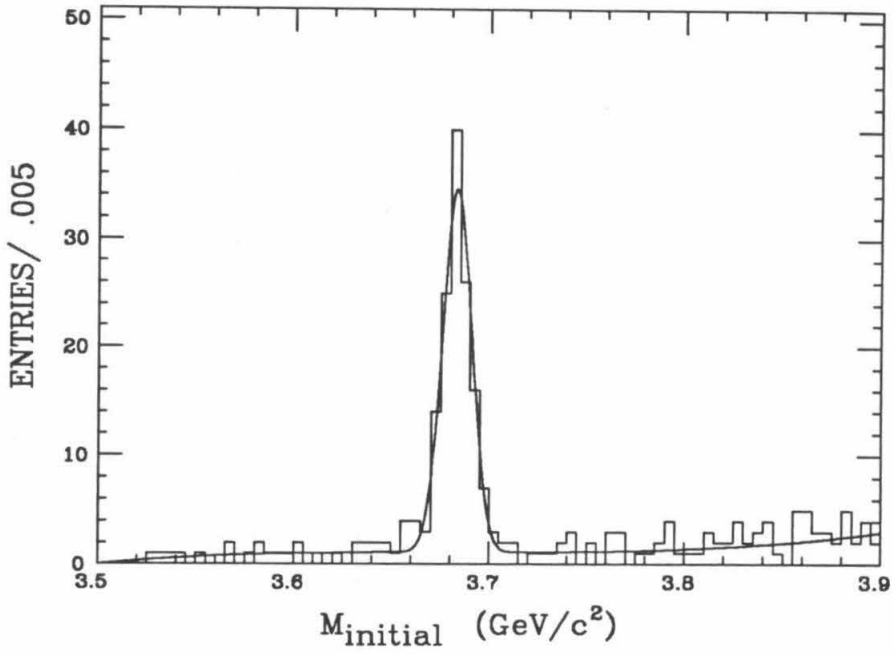

Figure 5.4.1: The $\psi(3685)$ reconstructed from the two lower momentum pions.

The invariant mass of each pair of oppositely charged tracks is required to be greater than 40 MeV/c^2 when the tracks are assumed to be electrons. This cut reduces the radiated Bhabha background with the photon converted into electron-positron pairs.

Fig. 5.4.2 shows the total momentum vs. the invariant mass of the charged tracks after these cuts. The region around a total momentum of 338 MeV/c and the invariant mass of the pions 3.415 GeV/c^2 is the potential χ_0 signal.

A cut is now used to reduce the background with recoil mass not equal to zero. The idea is to use the constraint so that for a one–photon process, the missing energy should equal the missing momentum of the charged tracks. We define U as:

$$U = E_{missing} - P_{missing}. \tag{5.8}$$

Here, $E_{missing} = 2E_{beam} - \sum_{i=1}^{4} E_i$ and $P_{missing} = |\sum_{i=1}^{4} \vec{P}_i|$ are the missing energy and missing momentum. E_{beam} is the beam energy, E_i and $\vec{P}_i$ are the

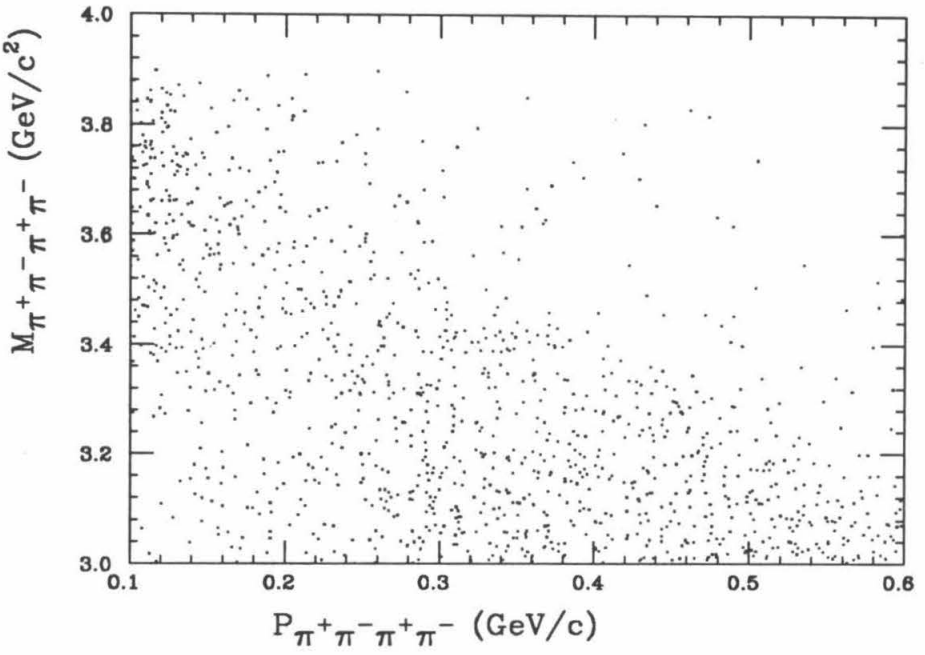

Figure 5.4.2: Raw $P_{charge\ total}$ vs. raw $M_{\pi^+\pi^-\pi^+\pi^-}$.

energy and momentum of the ith charged track.

In this analysis, events with $|U| > 0.1$ are rejected. This corresponds to a $\sim 2\sigma$ cut on the signal according to Monte Carlo studies (see Fig. 5.4.3). Most background that is due to heavy neutrals such as K_L^0, η etc. will be removed by this cut. Some π^0 background, from the reaction $e^+e^- \to \pi^+\pi^-\pi^+\pi^-\pi^0$ and the initial state radiation $\psi(3685)$ background, will, however, not be removed by this U-cut. To see this, we can use the π^0 background as an example. One notes that by definition :

$$U = \frac{M^2_{missing}}{E_{missing} + P_{missing}}, \tag{5.9}$$

so, for π^0 in this reaction,

$$U \sim 0.02 < 0.1 \quad . \tag{5.10}$$

To remove the π^0 background, the events are fitted to the hypothesis $\psi(3770) \to \pi^+\pi^-\pi^+\pi^- + \gamma\gamma$, a 4C fit and $\psi(3770) \to \pi^+\pi^-\pi^+\pi^-\pi^0$, a 5C fit.

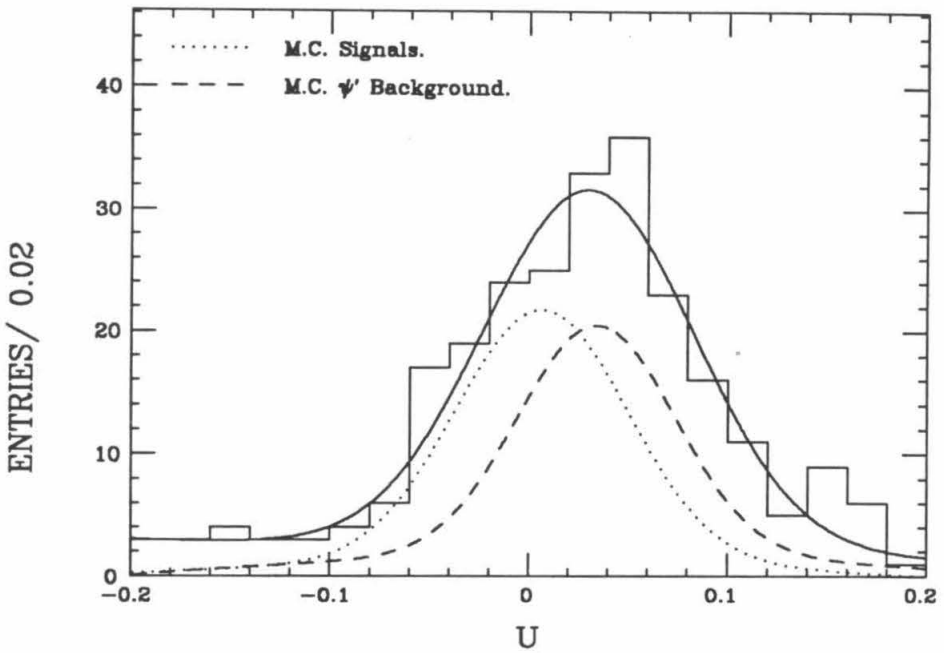

Figure 5.4.3: The $U = E_{missing} - P_{missing}$ parameter.

After the 4C fit, the invariant masses of the two photons indicate the presence of a clear π^0 background. To use the measured information most efficiently, a cut is made on the χ^2–probability of the 5C fit. Any event with the 5C fit χ^2–probability greater than 1% are rejected as π^0 background.

The 4C fit to $\psi(3770) \rightarrow \pi^+\pi^-\pi^+\pi^- + \gamma\gamma$ also allows us to reject some initial state radiation $\psi(3685)$ background. Any event with the 4C fit χ^2–probability greater than 1% and with the invariant mass of the 4 pions and the higher energy photon less than 3700 MeV, is rejected. Monte Carlo tests indicate that this cut reduces the efficiency for signals by less than 2%, while rejecting about 35% of the $\psi(3685)$ background. Fig. 5.4.4 shows the mass distribution in the data and the Monte Carlo. The Monte Carlo distribution is different from the data, indicating that this cut also reduces other types of background, which contain two photons in each event.

Using the track pairs from the 4C fit, a background that is due to K_s^o is also observed. Therefore, any event with an invariant mass of pion pairs within ± 10

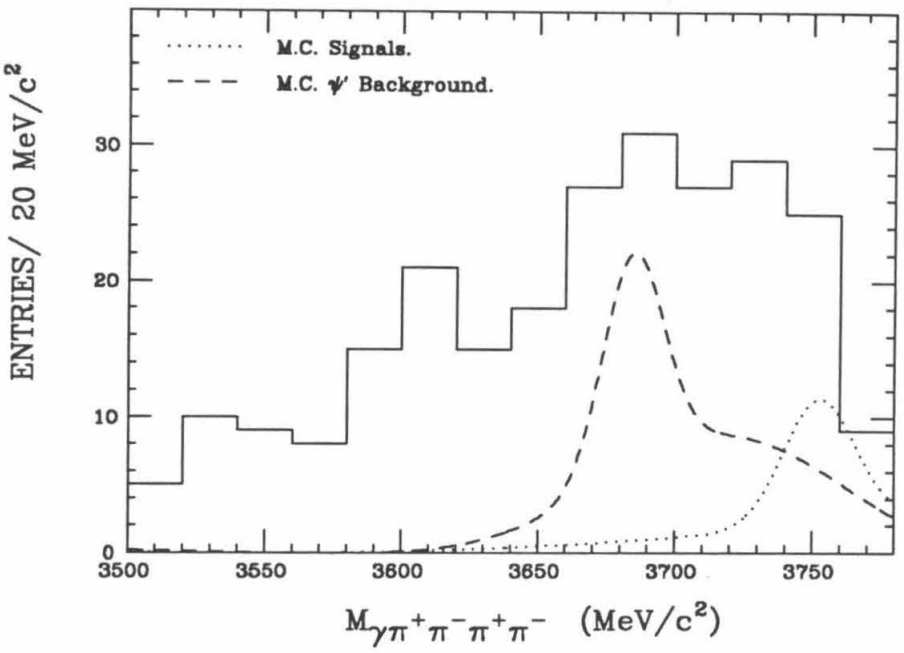

Figure 5.4.4: The invariant masses of the higher energy γ and $\pi^+\pi^-\pi^+\pi^-$.

MeV/c^2 of the K_s mass is rejected. Monte Carlo tests indicate that this cut causes less than 1% loss of signal.

Another requirement, effective in reducing the $\psi(3685)$ background, is on the alignment of the missing momentum and the direction of the photon. The alignment is defined as the largest $\cos\theta$ between the missing momentum of the charged tracks and the direction of the photons. A number of situations may occur. First, if a good photon has been found, then the alignment is the $\cos\theta$ between the missing momentum and this photon. Second, if no good photon has been found, but there is at least one neutral track in the shower counters, the alignment is defined as the largest $\cos\theta$ between the missing momentum and all shower tracks. Third, if no neutral track been found in the shower counter, then the alignment is defined as greater than 1. In this way, events in which the photon hits the edges of the showers counter and the ribs will still be collected to achieve a maximum efficiency. Finally, it is required that the $\cos\theta$ of the alignment be greater than 0.98.

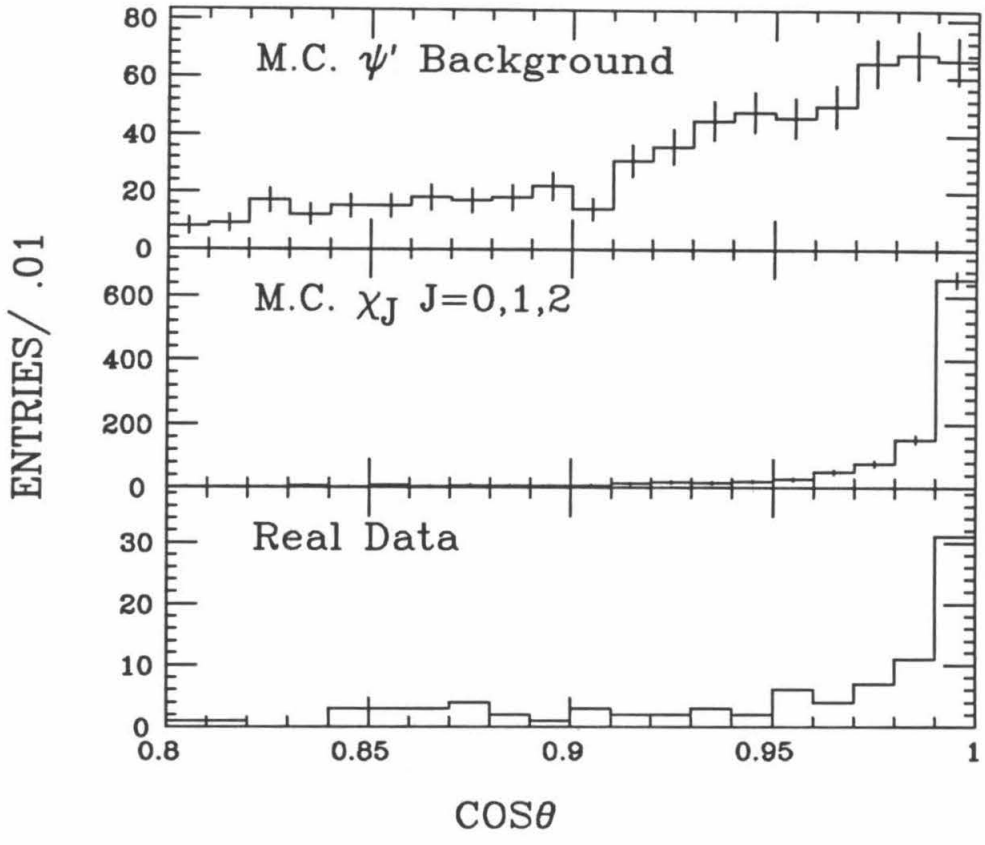

Figure 5.4.5: The best alignment between the γ and $P_{\pi^+\pi^-\pi^+\pi^-}$.

A comparison of the best alignment between data and Monte Carlo for the signals and for the $\psi(3685)$ background is shown in Fig. 5.4.5. The cut at 0.98 is seen to be very effective in reducing $\psi(3685)$ background, with only a small loss of signal.

Events with no detected photon are not shown in Fig. 5.4.5. These amount to about 5% for the signal, 4% for the $\psi(3685)$ background according to Monte Carlo studies, and 12% for the data. The data have a larger fraction of events without a detected photon because of additional non–$\psi(3685)$ background.

The final step is to fit the events to the hypothesis $\psi(3770) \rightarrow (missing - \gamma) + \pi^+\pi^-\pi^+\pi^-$. This is a 1C fit, the constraint coming from the requirement that the missing energy equal the missing momentum. A 1C fit is used instead of

a 4C fit because the 1C fit gives a higher efficiency that is due to photon detection efficiency and lack of alignment of the measurements from the drift chamber and shower detector.

According to the Monte Carlo, in this analysis the difference between the mass resolution of the 1C and 4C fit is small. The additional three constraints of the 4C are the energy, the angle ϕ , and angle λ of the photon. The photon energy contributes a negligible constraint on the $M_{\pi^+\pi^-\pi^+\pi^-}$ which is due to the large error on the photon energy measurement, compared with the both energy and momentum resolution of the four charged tracks. The missing momentum and the direction of the photon before the fit have already been required to be very well aligned. The constraint on the alignment has only a small effect on the resolution of the $M_{\pi^+\pi^-\pi^+\pi^-}$. Therefore, the additional three constraints have a very small effect on the resolution of the $M_{\pi^+\pi^-\pi^+\pi^-}$.

The χ^2−probability of the 1C fit is required to be greater than 10% . This is a very tight cut compared to the other cut on the χ^2−probability of the fit, because of the looser constraints.

A scatter plot of the 1C fitted invariant mass of the four pions vs. the χ^2−probability is shown in Fig. 5.4.6. The invariant mass of the four pions with χ^2−probability greater than 10% is shown in Fig. 5.4.7. A global fit to the Fig. 5.4.7 gives the mass of the χ_0 as 3412±6 MeV/c^2 and the χ_1 as 3504±8 MeV/c^2, and yields 13±4 event candidates for the χ_0 , 4.6±2.8 event candidates for the χ_1 and no candidates for the χ_2 . Fig. 5.4.6 shows that candidate events for theses resonances have a flat χ^2−probability distribution within statistical errors.

Background

The most important background comes from the initial state radiated $\psi(3685)$ background. There are two photons in each event for this background, but one has a small probability of being detected because it is likely to be along

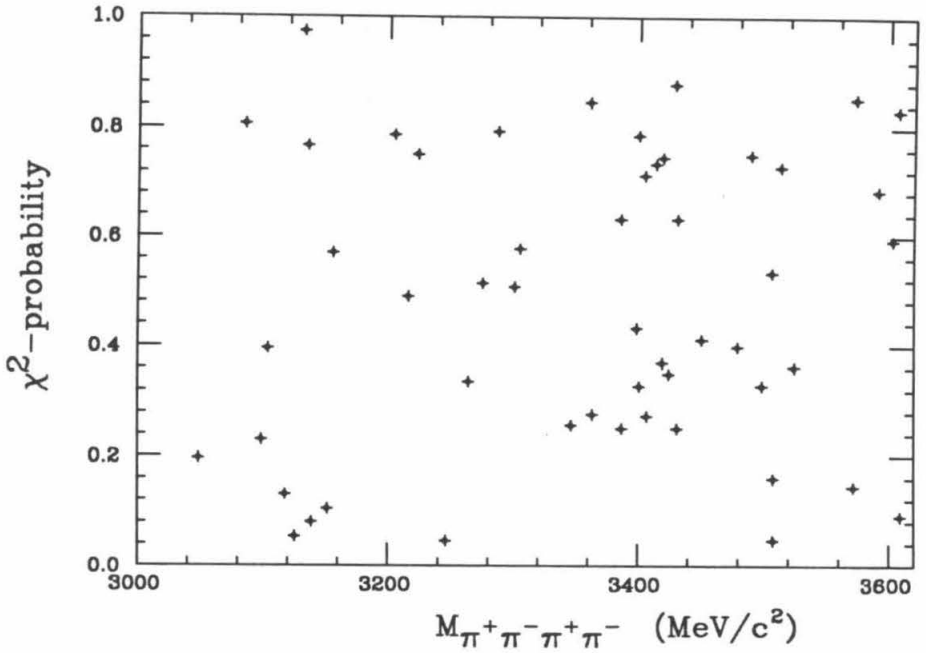

Figure 5.4.6: $M_{\pi^+\pi^-\pi^+\pi^-}$ vs. χ^2−probability .

the beam-pipe direction.[42] About 70% of these events will be detected with one photon, and 30% with two photons. Four cases can be distinguished:

1. Only one photon has been detected; the other is along the beam pipe or has not been found for some other reasons.
2. Two photons are detected, which are not in the same direction, and are therefore distinguishable.
3. Both photons are detected, but they are in the same direction and cannot be distinguished from each other.
4. No photon has been detected.

For case 1, events are likely to be rejected by the alignment or U cut. The events of case 2 are most likely removed by the mass requirement in the 4C fit or by the alignment cut. Case 3 is the worst one, as there is no way to distinguish between the signal and the background, but the probability of two photons' being in the same direction is very small. Case 4 may be partially rejected by the U

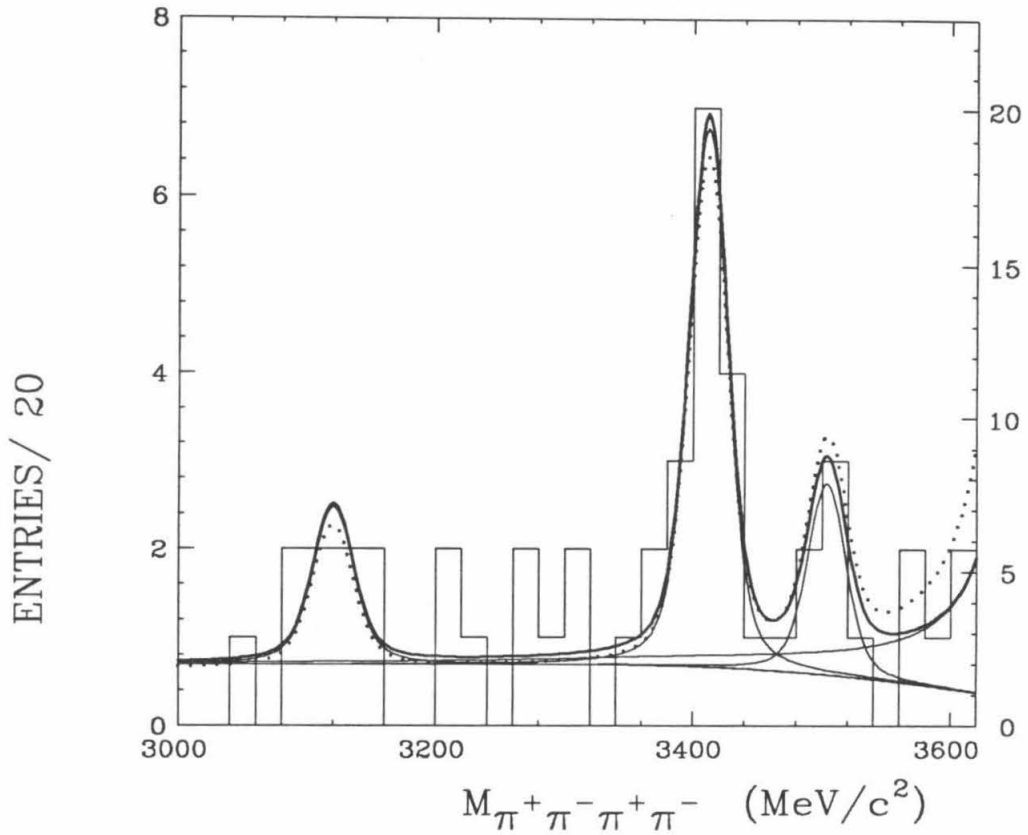

Figure 5.4.7: The invariant masses of the $\pi^+\pi^-\pi^+\pi^-$ after 1C fit. Dotted line is with efficiency correction.

cut. The cut on the χ^2−probability of the 1C fit, in fact, is very similar to the U cut except that it takes account of the measurement errors and also helps to reduce the background level.

The χ_J background from the $\psi(3685)$ is also studied using the Monte Carlo. One thousand Monte Carlo events have been generated for each χ_J; $J = 0, 1, 2$ with the initial state photon having a distribution predicted by Ref.(42). We have already discussed many characteristics of this background under the U cut, 4C fit, the best alignment cut and the 1C fit. The invariant mass distribution of $\pi^+\pi^-\pi^+\pi^-$ from this background, after the 1C fit to the hypothesis $\psi(3770) \rightarrow (missing - \gamma) + \pi^+\pi^-\pi^+\pi^-$ and the cuts, is shown in Fig. 5.4.8.

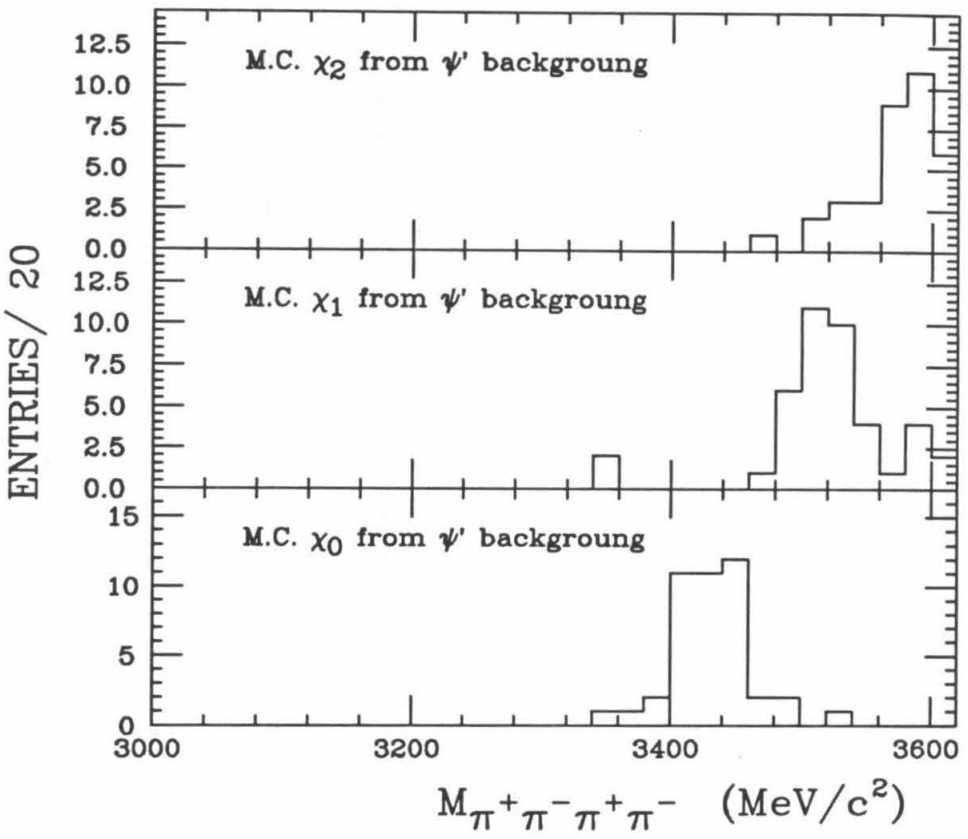

Figure 5.4.8: $M_{\pi^+\pi^-\pi^+\pi^-}$ of $\psi(3685)$ from M.C.

Mode	ϵ_{reject}	Br($\chi \to \pi^+\pi^-\pi^+\pi^-$)	Background events
$\chi_0 \to \pi^+\pi^-\pi^+\pi^-$	0.043	0.038±0.008	2.5
$\chi_1 \to \pi^+\pi^-\pi^+\pi^-$	0.041	0.017±0.005	1.0
$\chi_2 \to \pi^+\pi^-\pi^+\pi^-$	0.035	0.022±0.005	1.0

Table 5.IV. $\psi(3685)$ background for $\pi^+\pi^-\pi^+\pi^-$ of the χ_J .

Table 5.IV gives the number of $\psi(3685)$ background events from the Monte Carlo calculation.

There are also other potential types of background events. For example,

1. $\psi(3770) \to D\bar{D}$ and $D\bar{D} \to (4 - prongs) + neutral.$

2. $e^+e^- \rightarrow \gamma\psi(3685); \psi(3685) \rightarrow (4-prongs)$.

3. $e^+e^- \rightarrow \gamma J/\psi; J/\psi \rightarrow \pi^+\pi^-\pi^+\pi^-$.

4. $\psi(3770) \rightarrow \pi^+\pi^-\pi^+\pi^-\pi^0$.

5. $e^+e^- \rightarrow \pi^+\pi^-\pi^+\pi^-\pi^0$.

6. $e^+e^- \rightarrow (m-\gamma)(4-prongs)$.

Here, $m = 0, 1, 2...$.

All these backgrounds are negligible. They are rejected by the U cut, the 1C fit, the 5C fit for π^0, the 4C fit, the K_s cut, the photon conversion cut, the alignment cut and the good photon cut.

Efficiency

The total efficiency has been analyzed by a Monte Carlo calculation. The Monte Carlo events are generated with a uniform phase–space distribution for the photons and pions. Since the efficiencies are not strongly related to the direction of the photon or photon–detection efficiency, corrections for the actual angular distributions (Table 5.II) have been found unnecessary.

During the determination of the efficiency, the misidentification of the pions as electrons is studied by using both real $J/\psi \rightarrow \rho\pi \rightarrow \pi^+\pi^-\pi^0$ events and Monte Carlo events, where electron identification has been described in Chapter 3. First, by using the pion tracks in $J/\psi \rightarrow \rho\pi \rightarrow \pi^+\pi^-\pi^0$ events, the fraction of the misidentifications as a function of momentum is measured. Then, during the Monte Carlo test of the reconstruction programs, instead of using the electron identification procedure, this function is used for the probability of misidentification for this momentum. In this way, the error in the reconstruction efficiency is controlled within a few percent.

The distribution of the efficiency as a function of the invariant masses of the $\pi^+\pi^-\pi^+\pi^-$ has the same shape as the lower boundary line in Fig. 5.4.7. The efficiency for each state is listed in Table 5.V.

Decays	Efficiency
$\chi_0 \rightarrow \gamma\pi^+\pi^-\pi^+\pi^-$	0.31
$\chi_1 \rightarrow \gamma\pi^+\pi^-\pi^+\pi^-$	0.28
$\chi_2 \rightarrow \gamma\pi^+\pi^-\pi^+\pi^-$	0.25

Table 5.V: Reconstruction efficiencies for $\pi^+\pi^-\pi^+\pi^-$.

States	Events	$\sigma_{\psi(3770)} \times Br(\psi(3770) \rightarrow \gamma\chi_J)$
$\psi(3770) \rightarrow \gamma\chi_0$	10	$0.091 \pm 0.037 \pm 0.021$
$\psi(3770) \rightarrow \gamma\chi_1$	3.6	$0.081 \pm 0.063 \pm 0.025$
$\psi(3770) \rightarrow \gamma\chi_2$	0.0	≤ 0.104 (90% C.L.)

Table 5.VI: χ_J branching ratios from $\pi^+\pi^-\pi^+\pi^-$.

The branching ratio $\psi(3770) \rightarrow \gamma\chi_J$ from the $\pi^+\pi^-\pi^+\pi^-$ mode

The branching ratios are given by:

$$\sigma \times Br(\psi(3770) \rightarrow \gamma\chi_J) = \frac{number\ of\ events}{L \times Br.(\chi_J \rightarrow \pi^+\pi^-\pi^+\pi^-) \times \epsilon_{efficiency\ of\ the\ system}}. \quad (5.11)$$

The integrated luminosity L for this $\psi(3770)$ sample is 9.3 pb^{-1}. Using the branching ratios from Table 5.I, the total cross section of the $\psi(3770)$ times the branching ratios of the $\psi(3770) \rightarrow \chi_J$ are shown in Table 5.VI.

Systematic errors arise from several sources. For example:

1. Monte Carlo shower simulations: 10 to 20 % (see Ref.(45)).
2. Uncertainty of the branching ratios of the decay $\chi_J \rightarrow \pi^+\pi^-\pi^+\pi^-$.
3. Background: a). The Monte Carlo simulation of the $\psi(3685)$ background. b). Uncertainty in the determination of event loss due to pions misidentified as electrons.

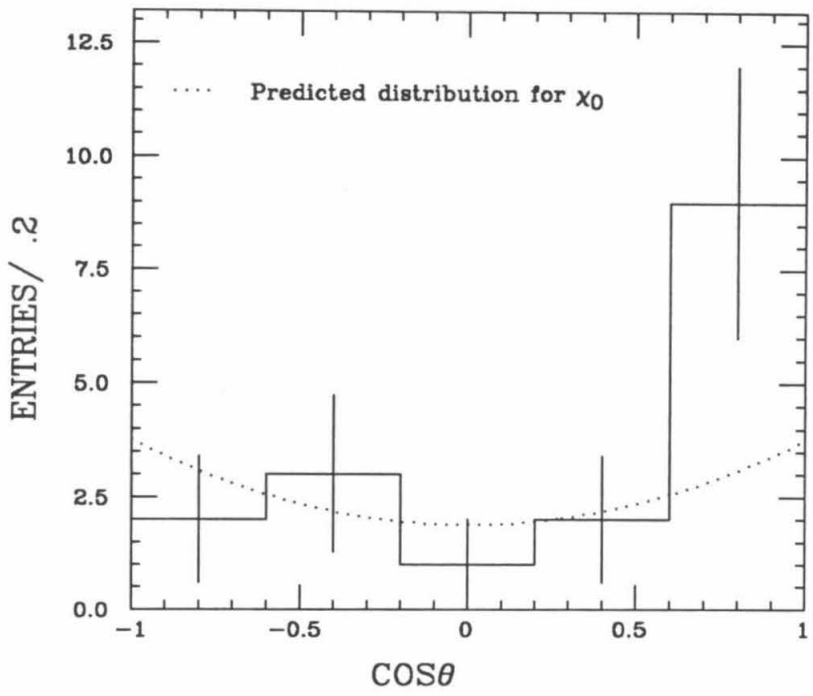

Figure 5.4.9: Angular distribution of γ from $\psi(3770)$.

5.5 Analysis of $\psi(3770) \to \gamma\chi_J; \chi_J \to \pi^+\pi^-\pi^+\pi^-\pi^+\pi^-$

The analysis of the χ_J decay into $\pi^+\pi^-\pi^+\pi^-\pi^+\pi^-$ is very similar to the analysis of χ_J decay into $\pi^+\pi^-\pi^+\pi^-$, except for the following differences:

1. There are six prongs in each event.
2. The particle identification method is slightly different. Events with tracks identified as electrons are not rejected. It is required, however, that the sum of the total identified pion tracks and the possible pion tracks is six. Details of the particle identification criteria have been discussed in Chapter 3.

The change of particle identification criteria is necessary because of the reconstruction efficiency. First, since the mean momentum of the charged tracks in this channel is 500 to 600 MeV/c compared with 800 to 900 MeV/c for the $\pi^+\pi^-\pi^+\pi^-$ case, the simple E/P method of electron identification would cause

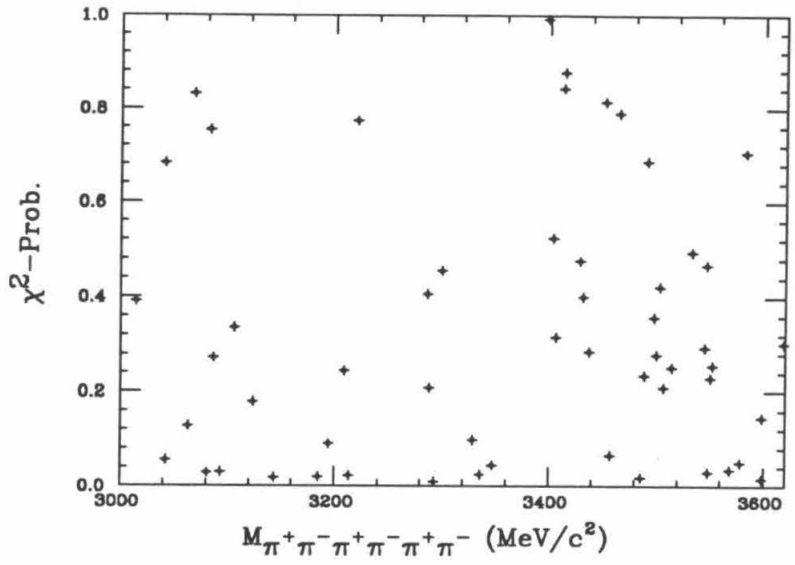

Figure 5.5.1: $M_{\pi^+\pi^-\pi^+\pi^-\pi^+\pi^-}$ vs. χ^2–probability .

a large fraction of pions to be misidentified as electrons. Also, since there are six charged tracks in each event, the probability of at least one track in each event's being misidentified as an electron is larger than in the four prong case.

A scatter plot of six–pion mass vs. χ^2–probability of the 1C fit to the hypothesis $\psi(3770) \rightarrow (missing - \gamma) + \pi^+\pi^-\pi^+\pi^-\pi^+\pi^-$ is shown in Fig. 5.5.1. The invariant masses of the 1C fitted $\pi^+\pi^-\pi^+\pi^-\pi^+\pi^-$ is shown in Fig. 5.5.2 for events with χ^2–probability greater than 10% .

Fig. 5.5.2 also shows the global fits of the 1C fitted invariant masses of the $\pi^+\pi^-\pi^+\pi^-\pi^+\pi^-$. The χ_0 and χ_1 signals are significant. The fit gives the mass of the χ_0 as 3417 ± 7 MeV, the χ_1 as 3500 ± 12 MeV, and the χ_2 as 3551 ± 8 MeV, consistent with the masses from the $\gamma J/\psi$ and the $\pi^+\pi^-\pi^+\pi^-$ cases as shown in Fig. 5.3.2 and Fig. 5.4.7, and from other experiments.

The initial state radiated $\psi(3685)$ background contributions are again determined by the Monte Carlo method. The momentum resolution of the six prong case is better than that in the case of four prongs; the $\psi(3685)$ background is thus more likely to be rejected.

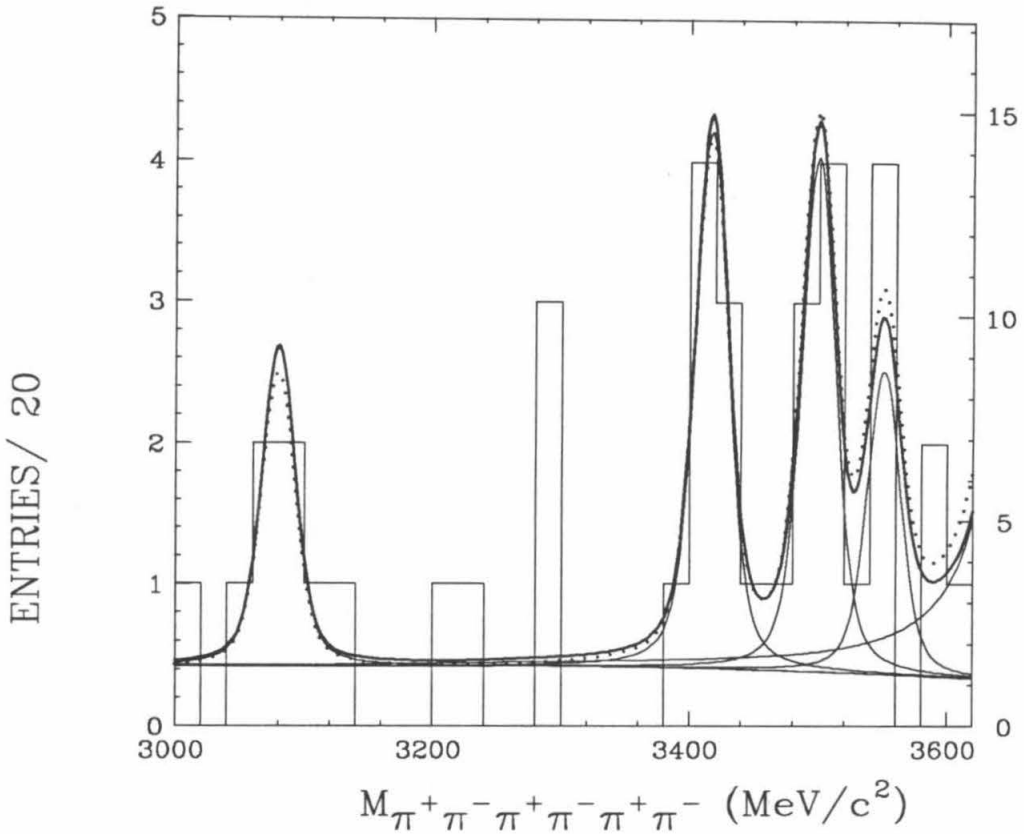

Figure 5.5.2: The 1C fitted masses of the $\pi^+\pi^-\pi^+\pi^-\pi^+\pi^-$.

Modes	Events	$\psi(3685)$ Bkgd	$\epsilon_{recon.}$	$\sigma_{\psi(3770)} \times Br(\psi(3770) \rightarrow \gamma\chi)$
χ_0	7.2	1.4	0.30	0.14±0.07±0.04
χ_1	6.7	0.9	0.28	0.10±0.05±0.04
χ_2	4.0	0.4	0.28	0.13±0.08±0.09

Table 5.VII χ_J branching ratios from $\pi^+\pi^-\pi^+\pi^-\pi^+\pi^-$.

5.6 Conclusion

The electromagnetic transitions of the $\psi(3770)$ to the χ_J states have been

Modes	Number of events	$\sigma_{\psi(3770)} \times Br(\psi(3770) \to \gamma\chi)$ (nb)
$\chi_1 \to \gamma J/\psi$	5.6	0.083±0.042±0.015
$\chi_2 \to \gamma J/\psi$	1	$\leq$ 0.14 (at 90% C.L.)
$\chi_0 \to \gamma\pi^+\pi^-\pi^+\pi^-$	10.	0.091 ±0.037 ± 0.021
$\chi_1 \to \gamma\pi^+\pi^-\pi^+\pi^-$	3.6	0.081 ±0.063 ± 0.025
$\chi_2 \to \gamma\pi^+\pi^-\pi^+\pi^-$	0.0	$\leq$0.10 (at 90% C.L.)
$\chi_0 \to \gamma\pi^+\pi^-\pi^+\pi^-\pi^+\pi^-$	5.8	0.14±0.07±0.04
$\chi_1 \to \gamma\pi^+\pi^-\pi^+\pi^-\pi^+\pi^-$	5.8	0.10±0.05±0.04
$\chi_2 \to \gamma\pi^+\pi^-\pi^+\pi^-\pi^+\pi^-$	3.6	0.13±0.08±0.09

Table 5.VIII: χ_J branching ratios from all modes.

$\psi(3770) \to \gamma+$	$\sigma_{\psi(3770)} \times Br(\psi(3770) \to \gamma\chi)$ (nb)
χ_0	0.10±0.04
χ_1	0.088±0.032
χ_2	$\leq$ 0.10 (at 90% C.L.)

Table 5.IX: Weighted average and errors of electric dipole transitions.

observed in three decay modes of the χ_J . The results are summarized in Table 5.VIII.

From Table 5.VIII, the weighted average and error can be calculated. These are listed in Table 5.IX. Table 5.X gives a list of the partial widths and the branching ratios based on the three different experimental measurements of the total cross section of the $\psi(3770)$.

These results can be compared with the predicted values in Table 1.II. The

$\sigma_{\psi(3770)}$ (nb)	$\Gamma(\psi(3770) \to \gamma\chi_0)$ (100×keV)	$Br(\psi(3770) \to \gamma\chi_0)$ $(\times 10^{-2})$
5.00 (Mark–III)[5]	5.1±1.9	2.0±0.7
6.75 (Crystal–Ball)[39]	3.8±1.4	1.5±0.6
9.3 (Mark–II)[37]	2.7±1.0	1.1±0.4
	$\Gamma(\psi(3770) \to \gamma\chi_1)$	$Br(\psi(3770) \to \gamma\chi_1)$ $(\times 10^{-2})$
5.00 (Mark–III)	4.4±1.6	1.8±0.6
6.75 (Crystal–Ball)	3.3±1.2	1.3±0.5
9.3 (Mark–II)	2.4±0.9	0.95±0.34
	$\Gamma(\psi(3770) \to \gamma\chi_2)$	$Br(\psi(3770) \to \gamma\chi_2)$ $(\times 10^{-2})$
5.00 (Mark–III)	$\leq$ 5.2	$\leq$ 2.1
6.75 (Crystal–Ball)	$\leq$3.9	$\leq$1.6
9.3 (Mark–II)	$\leq$2.8	$\leq$ 1.1

Table 5.X Branching ratios and partial widths.

experimental measurements and the predicted values are shown in Fig. 5.6.1. It seems that with the total cross section of the $\psi(3770)$ in the range of 6 to 8 nb, the predictions are consistent with the experimental measurements.

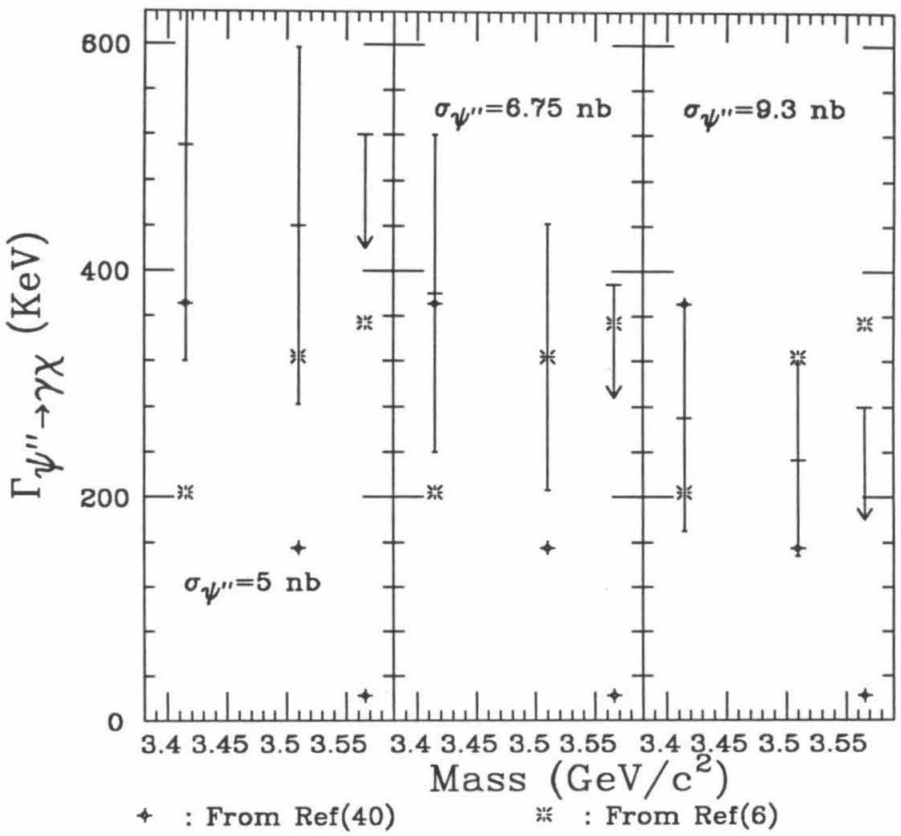

Figure 5.6.1: The comparison between predicted and measured widths.

6. DIRECT HADRONIC DECAYS OF THE $\psi(3770)$

6.1 $\pi^+\pi^-\pi^0$ FINAL STATE

Introduction

The studies for the $\rho\pi$ final states may help clarify the V–P puzzle and the rescattering as discussed in Section 1.8.

Event selection

Each event is required to have two good charged tracks, none of tracks is identified as an electron, muon, kaon or proton. Each event is required to have two good photons with a minimum energy of 30 MeV. The recoil mass of the two charged tracks in each event is required to be less than 1 GeV/c^2. Particle identification methods have been discussed in Chapter 3.

The events are fitted to the 4 constraint hypothesis $e^+e^- \rightarrow \gamma\gamma\pi^+\pi^-$ by using SQUAW. The events with χ^2–probability of the 4C fit greater than 5% are retained. The invariant mass of two photons is shown in Fig. 6.1.1

The rest–frame decay angle of the π^0 and η can be measured and used to reject the background. If $\cos\theta'$ is the cosine of the angle between the direction of the photon and the direction of the missing momentum of the charged tracks, then the decay angle in the rest frame of the π^0 or η will be:

$$\cos\theta_{\pi^0} = \frac{\cos\theta' + \beta_{\pi^0}}{1 + \beta_{\pi^0} \times \cos\theta'} \tag{6.1}$$

$$\cos\theta_{\eta} = \frac{\cos\theta' + \beta_{\eta}}{1 + \beta_{\eta} \times \cos\theta'} \quad . \tag{6.2}$$

Here, β_{π^0} is the velocity of the π^0, and β_η is the velocity of the η, which can be calculated from the momentum of the charged tracks. Since both the π^0 and the η are spin–zero mesons, the decay angles of the photons from π^0 (or η) are uniformly distributed in the π^0 or η rest frame. The background, in general, is

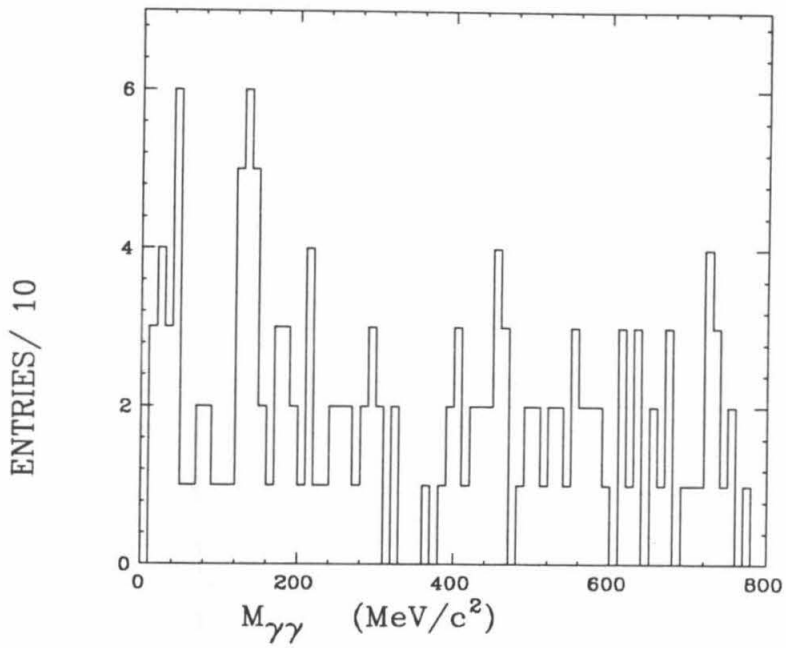

Figure 6.1.1: $M_{\gamma\gamma}$ before the rest–frame decay angle cut.

peaked at $\cos\theta = \pm 1$. If we reject those events with large $|\cos\theta|$, we can improve the signal to background ratios.

Fig. 6.1.2 is this $\cos\theta$ distribution of the data with the rest frame calculated from the fitted invariant masses and the fitted total momentum of the two photons. The photon with larger energy is used to calculate the angle. The dotted and dashed lines are the Monte Carlo calculation for the signals for π^0 and η decay. It is clear that a cut on $|\cos\theta| \leq 0.8$ is very effective in reducing the background.

A hand scan is performed on these events after the rest–frame decay angle cut. Seven events are rejected by this scan. Three events are found to have four charged tracks, with the additional charged tracks not being reconstructed. Four events are found to have three photons.

Finally, following the hand scan, the invariant masses of the two photons are shown in Fig. 6.1.3. There are two structures, one at the π^0 mass and another at

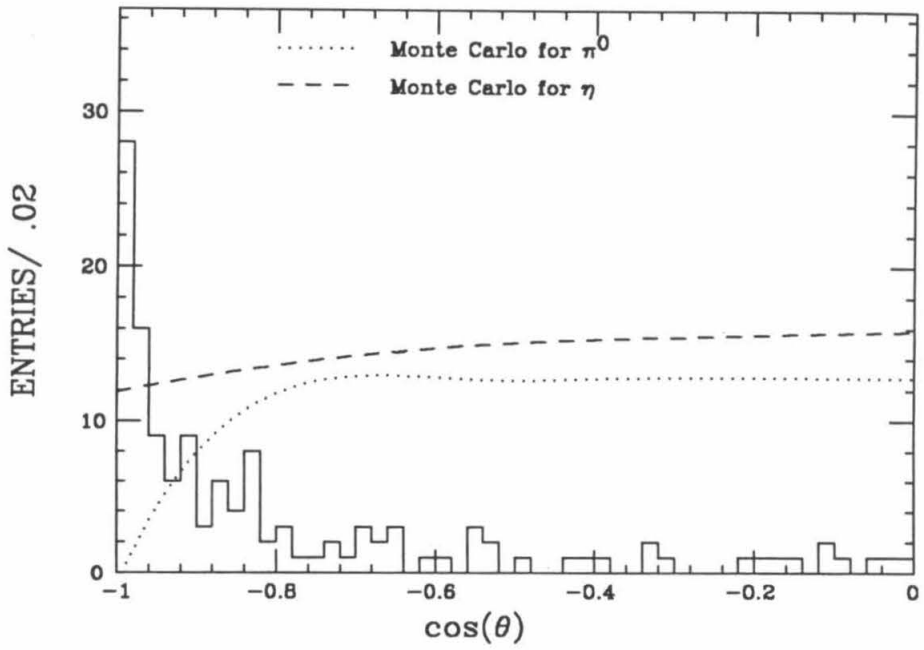

Figure 6.1.2: The rest frame decay angles.

the η mass. The curves are from a global fit that takes account of the efficiency correction, with fixed widths for the π^0 and η determined from the Monte Carlo. The fitted masses of the two photons vs. the χ^2–probability are shown in Fig. 6.1.4. Within the statistical error, the distribution for the signals are flat when the χ^2-probability is greater than 5% . Eight events are π^0 candidates and seven are η .

A study is made to investigate the $\rho\pi$ intermediate state. Requiring the invariant mass of the two photons within ± 20 MeV/c^2 of the π^0 mass, Fig. 6.1.5. shows $M^2_{\pi^+\pi^0}$ vs. $M^2_{\pi^-\pi^0}$ (see Fig. 6.1.6 for Monte Carlo data).

Background

The possible sources of the background are:

1. Radiative Bhabhas and di-muon events.
2. Radiative $\psi(3685)$ events.
3. Misidentification of $K^\pm\pi^\mp\pi^0$ and $K^+K^-\pi^0$.

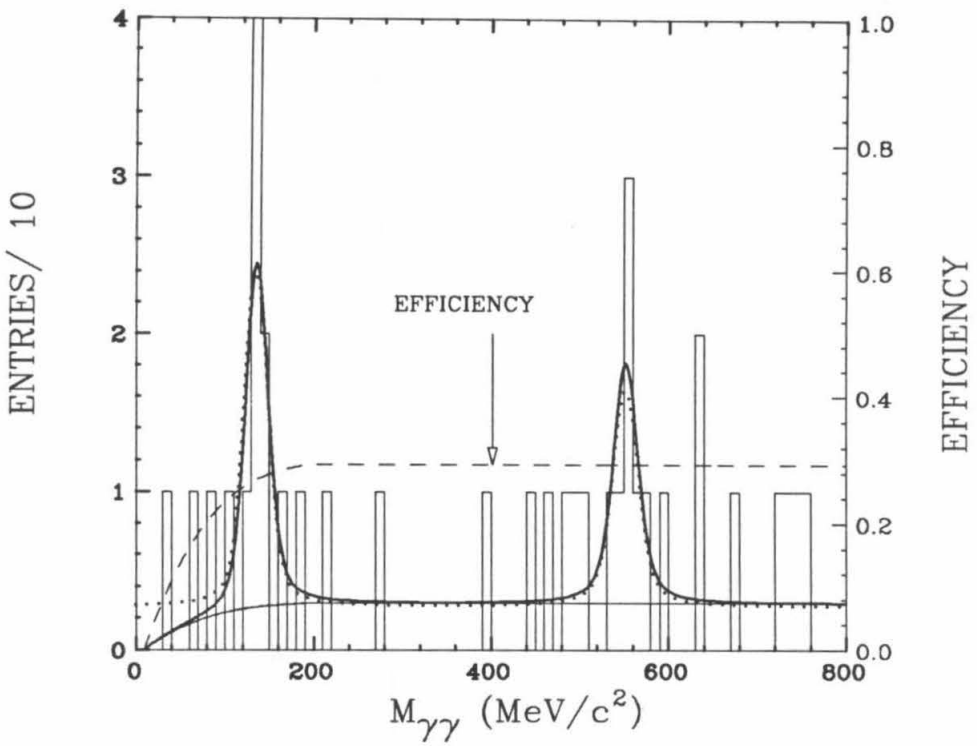

Figure 6.1.3: $M_{\gamma\gamma}$ after the rest–frame decay angle cut.

4. Continuum production of $\pi^+\pi^-\pi^0$.

The radiative Bhabha background gives a continuous mass distribution of the two photons peaked at low masses; they can be easily separated from signals. The total number of initial state radiative $\psi(3685)$ events before reconstructing in this decay channel is about 1.4 events. This background is therefore negligible. The background that is due to misidentification of $K^{\pm}\pi^{\mp}\pi^0$ and $K^+K^-\pi^0$ has a small effect on the signal, since the total number of events is small, and they are also rejected by the event selection procedure.

There is, in fact, no serious background except for the continuum background. Since the continuum contribution is identical to the signal, we cannot separate these events from those that is due to the decay of the $\psi(3770)$.

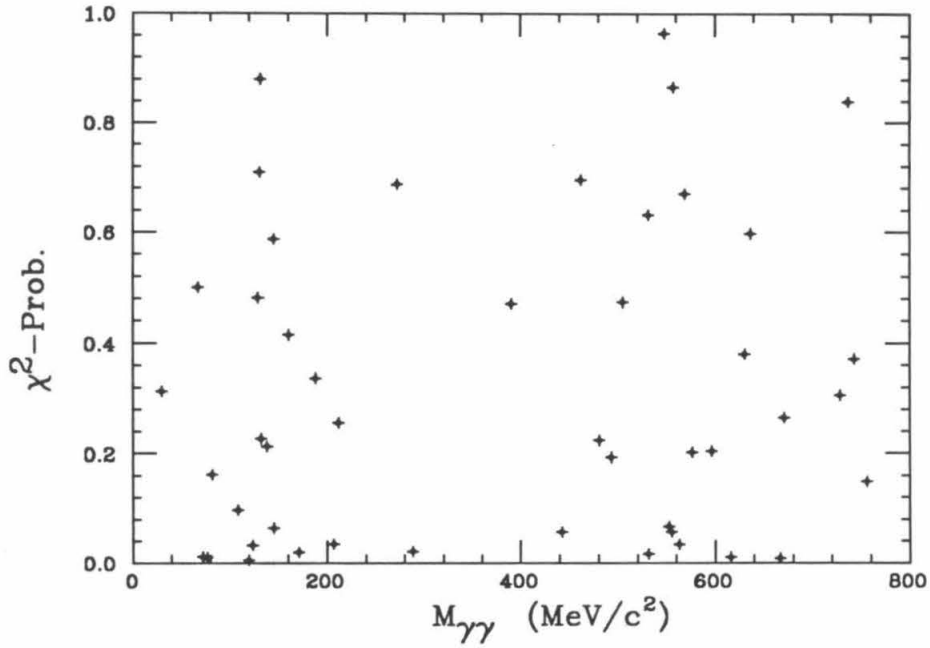

Figure 6.1.4: $M_{\gamma\gamma}$ vs. χ^2-probability of $2\pi^{\pm}2\gamma$.

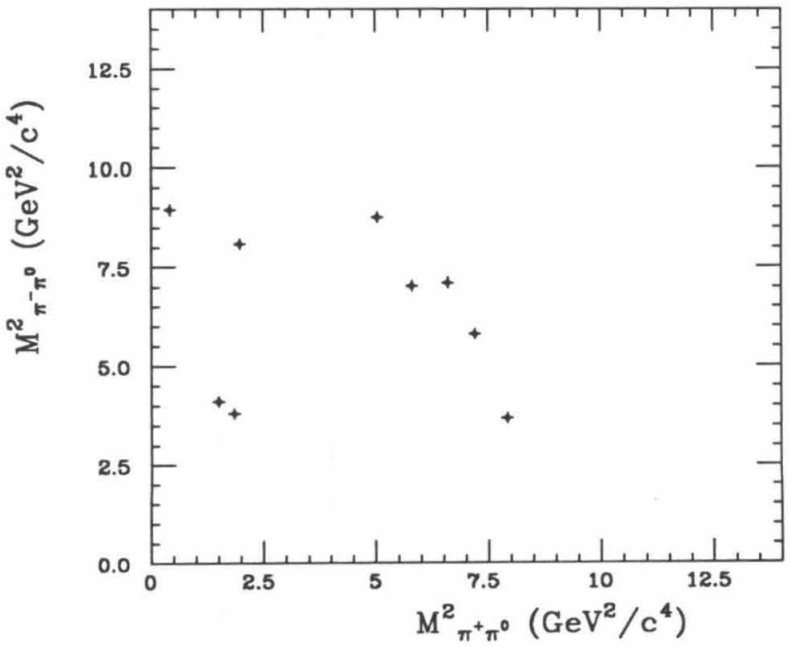

Figure 6.1.5: $M^2_{\pi^+\pi^0}$ vs. $M^2_{\pi^-\pi^0}$ of $2\pi^{\pm}2\gamma$.

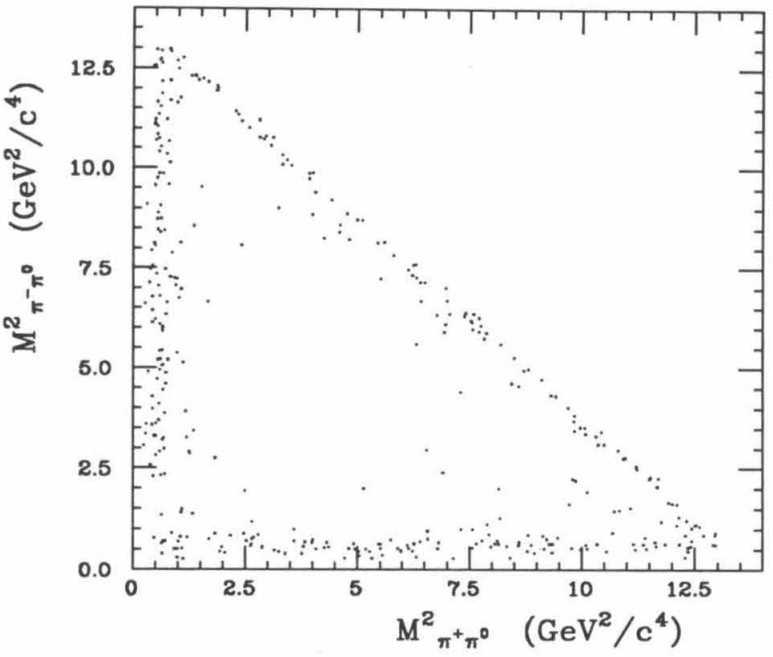

Figure 6.1.6: $M^2_{\pi^+\pi^0}$ vs. $M^2_{\pi^-\pi^0}$ from M.C..

Efficiency

The reconstruction efficiency is determined by a combination of Monte Carlo calculation and of data at the J/ψ . The situation is very similar to the case of the calculation of the reconstruction efficiency for the process $\psi(3770) \rightarrow \gamma\pi^+\pi^-\pi^+\pi^-$. First, using the data sample for the process $J/\psi \rightarrow \rho\pi$, we determine the fraction of pions misidentified as electrons as a function of momentum. This function is then used during the reconstruction of the Monte Carlo events to determine the overall efficiency.

This method omits the dependence of the misidentification probability for the pions as electrons on polar angles. As an example, this misidentification probability in the region between the barrel and end cap shower counters could be different from that in other regions. This uncertainty is included in the systematic error.

Finally, the reconstruction efficiencies including the uncertainty that is due

Mode	$\epsilon_{recon.}$
$\rho^0\pi^0$	0.23 ± 0.05
$\rho^{\pm}\pi^{\mp}$	0.26 ± 0.05
$\pi^+\pi^-\eta$	0.27 ± 0.05

Table 6.I Reconstruction efficiencies for $\pi^+\pi^-\gamma\gamma$.

$\sigma_{\psi(3770)}$ nb	$\Gamma(\psi(3770) \to \rho\pi)$ (KeV) (at 90% C.L.)	$Br(\psi(3770) \to \rho\pi)$ (at 90% C.L.)
5.00 (Mark–III)[5]	$\leq 31.$	$\leq 1.3 \times 10^{-3}$
6.75 (Crystal–Ball)[39]	$\leq 23.$	$\leq 9.4 \times 10^{-4}$
9.3 (Mark–II)[37]	$\leq 17.$	$\leq 6.8 \times 10^{-4}$

Table 6.II Upper limits for $\rho\pi$ final states.

to the use of the fake shower method and the uncertainty in the misidentification function of the pions as electrons are listed in Table 6.I.

Conclusion

The total cross section for the $\rho\pi$ final state including contributions from the $\psi(3770)$ and from the continuum is:

$$\sigma_{\psi(3770)} \times Br(\rho\pi) + \sigma_{continuum} = (3.5 \pm 1.2 \pm 0.7) \times 10^{-3} \qquad (6.3)$$

$$\sigma_{\psi(3770)} \times Br(\pi^+\pi^-\eta) + \sigma_{continuum} = (5.9 \pm 2.7 \pm 1.2) \times 10^{-3}. \qquad (6.4)$$

An up limits of the $\psi(3770) \to \rho\pi$ are summarized in Table 6.II.

These values can be compared with the partial width of the $\Gamma(\phi \to \rho\pi) =$ 633 KeV, $\Gamma(J/\psi \to \rho\pi) = 800$ eV and $\Gamma(\psi(3685) \to \rho\pi) = 17$ eV.

6.2 OTHER NON–CHARMED HADRONIC FINAL STATES OF THE $\psi(3770)$

Introduction

In this section, searches for a number of other non–charmed hadronic final states of the $\psi(3770)$ are summarized. These modes are listed in Table 6.III.

Event selection

The "good charged track" and "good photon" identification methods have been discussed in Chapter 3 and will therefore not be repeated here. A good photon is required to have a shower energy greater than 30 MeV.

The basic requirements for each mode are listed in Table V.III. In addition to these requirements, no identified muon can be present in any final state. No good photon is found for modes that do not contain photons. A minimum of two good photons are required for modes containing a π^0 or a η ; the maximum number of photons allowed in each event is determined from the background level.

As an example: for mode $p^+p^-\pi^+\pi^-\pi^0$, it is required that each event have two or three good photons, one or two pions, one or two protons, and no muons, or kaons.

The events are fitted to the hypotheses listed in Table 6.III by using SQUAW. In the fit, a track used by the fitter as a certain type is required to be at least a "possible" of this type if particle identification is present. Unidentified tracks are always accepted. All photons must be "good photons." Only the events with the χ^2–probability of the 4C fit greater than 5% are retained.

A rest frame decay angle cut is also applied to those modes that contain a π^0 or a η . The rest frame is the frame calculated using the fitted momenta and mass of the two photons. The absolute value of the cosine of the decay angle is required to be less than 0.9 except for mode $K^+K^-K^+K^-\gamma\gamma$, where it is 0.8. The tighter cut in the $K^+K^-K^+K^-\gamma\gamma$ mode is found necessary to keep a reasonable single to noise ratio.

Final states	Minimum	Maximum	Fit hypo. ($e^+e^- \rightarrow$)
$\pi^+\pi^-\pi^+\pi^-$	4 possible $\pi^\pm$	$0K^\pm$, $0p^\pm$	$\pi^+\pi^-\pi^+\pi^-$
$\pi^+\pi^-\pi^+\pi^-\pi^0$	2γ , 4 possible $\pi^\pm$	2γ ,$0K^\pm$, $0p^\pm$	$\pi^+\pi^-\pi^+\pi^-\gamma\gamma$
$\pi^+\pi^-\pi^+\pi^-\eta$	2γ , 4 possible $\pi^\pm$	2γ ,$0K^\pm$, $0p^\pm$	$\pi^+\pi^-\pi^+\pi^-\gamma\gamma$
$K^+K^-K^+K^-$		$0\pi^\pm$, $0p^\pm$	$K^+K^-K^+K^-$
$K^+K^-K^+K^-\pi^0$	2γ	3γ ,$0\pi^\pm$, $0p^\pm$	$K^+K^-K^+K^-\gamma\gamma$
$K^+K^-K^+K^-\eta$	2γ	3γ ,$0\pi^\pm$, $0p^\pm$	$K^+K^-K^+K^-\gamma\gamma$
$p^+p^-\pi^+\pi^-$	$1\pi^\pm$, $1p^\pm$	$2\pi^\pm$, $2p^\pm$,$0K^\pm$	$p^+p^-\pi^+\pi^-$
$p^+p^-\pi^+\pi^-\pi^0$	2γ ,$1\pi^\pm$, $1p^\pm$	3γ ,$2\pi^\pm$, $2p^\pm$,$0K^\pm$	$p^+p^-\pi^+\pi^-\gamma\gamma$
$p^+p^-\pi^+\pi^-\eta$	2γ ,$1\pi^\pm$, $1p^\pm$	3γ ,$2\pi^\pm$, $2p^\pm$,$0K^\pm$	$p^+p^-\pi^+\pi^-\gamma\gamma$

Table 6.III Cuts and fit hypotheses.

The invariant masses of the two photons are shown in Fig. 6.2.1 for modes containing two photons. A π^0 signal is found in each mode with high statistical significance. A large η signal is also found in the mode $\pi^+\pi^-\pi^+\pi^-\gamma\gamma$. An η may also exist in the mode $p^+p^-\pi^+\pi^-\gamma\gamma$ but with less statistical significance. No η is found in the $K^+K^-K^+K^-\gamma\gamma$ mode.

The χ^2−probability distributions for the modes whose final states do not contain photons are shown in Fig. 6.2.2.

Background

The sources of background are:

1. $D\bar{D}$ background.
2. Decays of $\psi(3685)$ produced via initial state radiation.
3. Misidentification of particle types.
4. Continuum background.

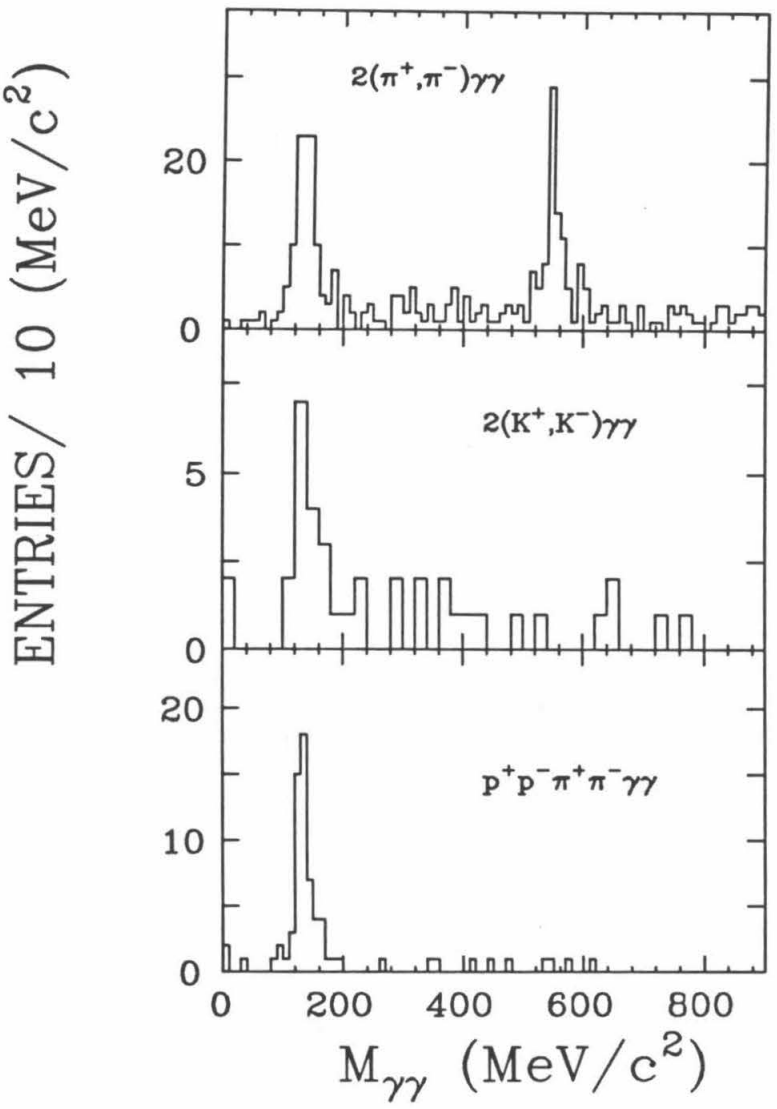

Figure 6.2.1: $M_{\gamma\gamma}$ from the 4C fit with the rest frame decay angle cut.

The contributions of the $D\bar{D}$ background can be calculated, since most branching ratios for the interesting final states are available. This background contributes a very small percentage to the total number of events.

The contributions of the $D\bar{D}$ background can also be checked by using the maximum momentum track method. The decays of the $\psi(3770)$ into each final state through $D\bar{D}$ are two–step decays. Now, if we compare the largest mo-

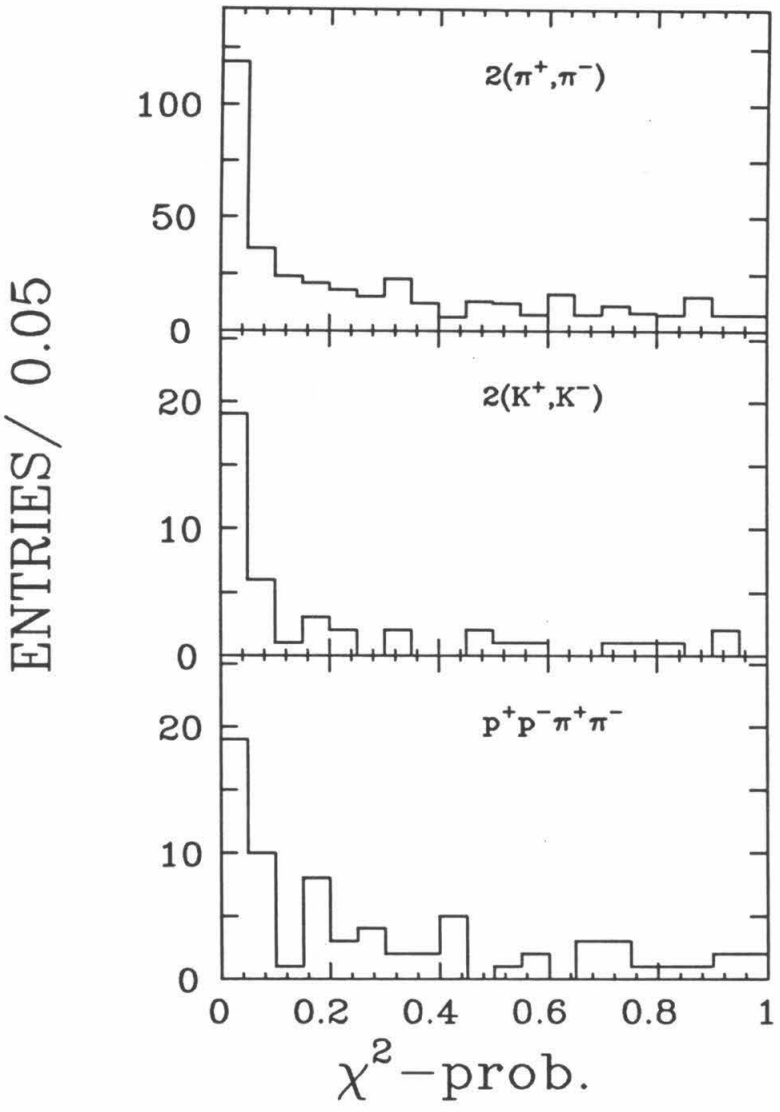

Figure 6.2.2: χ^2−probability of modes with photons.

mentum of the tracks in the decays through $D\bar{D}$ and not through $D\bar{D}$, we find that the decays through $D\bar{D}$ yield smaller laboratory momenta than those not through $D\bar{D}$. The momenta of tracks from the decays through $D\bar{D}$ are limited by half of the mass of the D or about one–quarter of the $\psi(3770)$ mass, since the D is produced almost at rest. However, for the one–step decay, the momentum is limited by about one–half of the $\psi(3770)$ mass.

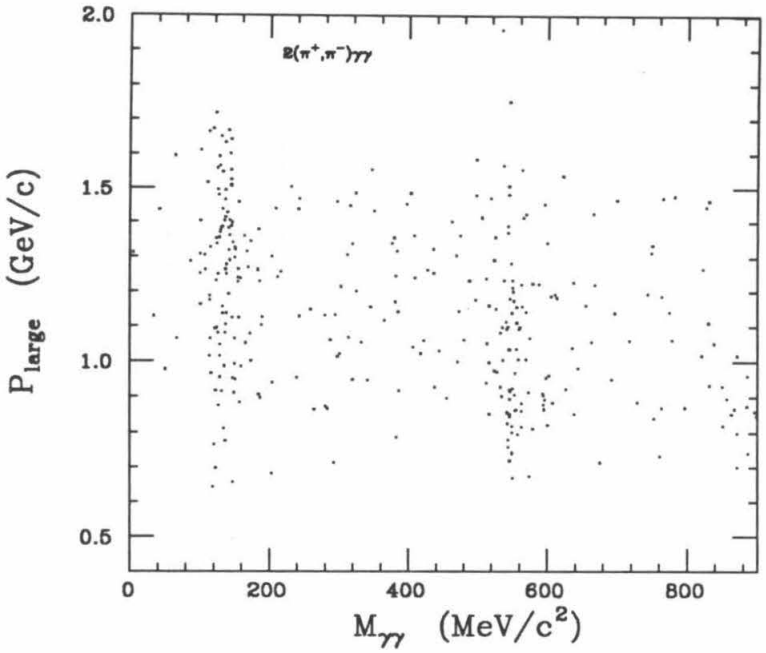

Figure 6.2.3: $M_{\gamma\gamma}$ vs. $P_{largest}$.

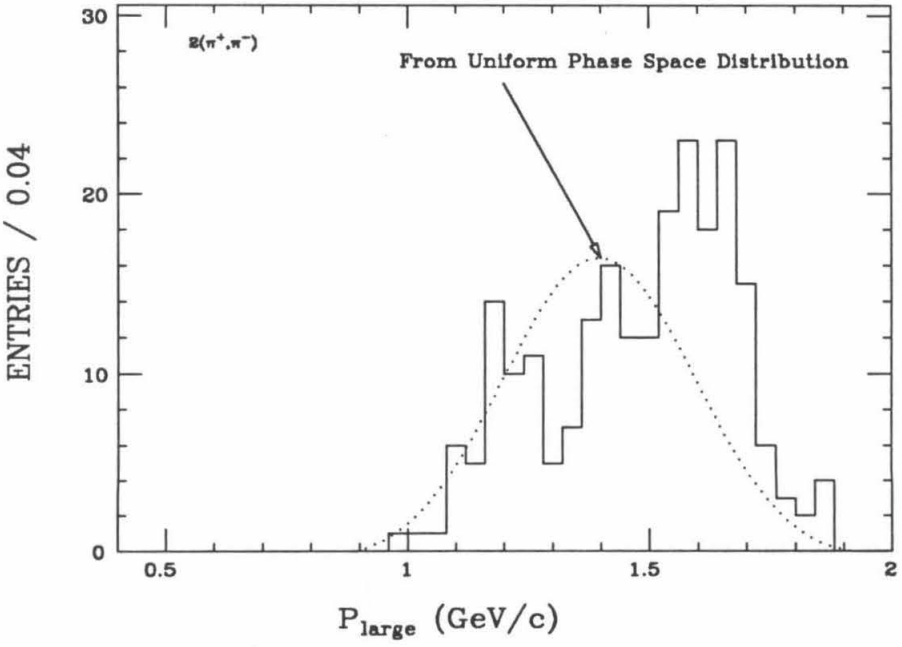

Figure 6.2.4: $P_{largest}$ from modes without γ .

Fig. 6.2.3 shows invariant masses of the two photons vs. the largest momentum of the charged tracks for the mode of $\pi^+\pi^-\pi^+\pi^-\gamma\gamma$. For the π^0 band, $D\bar{D}$ background could exist only with this momentum, less than 1 GeV/c, while most events in this plot indicate that this momentum is greater than 1 GeV/c. In the η band, at least half of the events have this momentum greater than 1 GeV/c.

Fig. 6.2.4 shows the distribution of the largest momentum for the mode $\pi^+\pi^-\pi^+\pi^-$. The events in the figure have χ^2−probability greater than 10% . All events have at least one track with momentum greater than 1 GeV/c. The distribution also appears quite different from the uniform phase space distribution shown by the dotted line. The difference indicates the existence of intermediate states.

The 4C fit for modes containing only charged tracks have very strong kinematic constraints. Almost no background events except continuum could pass the fits with a χ^2−probability greater than 10% .

The rejection factors for the initial state radiation $\psi(3685)$ are determined using the Monte Carlo method and are found to be 1% to 7% , depending on the mode. For the modes whose final states contain two photons, less $\psi(3685)$ background is rejected, but the invariant mass distributions of the background are different from the signals because of the pulls on the energy of the photons. This difference amounts to 50 MeV at the η mass. The contribution of this background for most modes is negligible except for the $\pi^+\pi^-\pi^+\pi^-\pi^0$ mode, where it is estimated to be 3.5 events.

The contributions from the continuum background is undeterminable because of the unknown production cross section at the $\psi(3770)$ energy.

The total background contributions are summarized and listed in Table 6.IV.

Efficiencies

The efficiency for each mode is determined by Monte Carlo calculation. For

Mode	Events	Background	$\epsilon_{recon.}$ (%)	$\sigma_\psi(3770) \times Br. + \sigma_{continuum}$ ($\times 10^{-2}$ nb)
$\pi^+\pi^-\pi^+\pi^-$	229	0	48	5.1±0.3±0.5
$\pi^+\pi^-\pi^+\pi^-\pi^0$	94	7	26	3.6±0.4±0.7
$\pi^+\pi^-\pi^+\pi^-\eta$	83	0	28×0.389	8.2±1.0±1.2
$K^+K^-K^+K^-$	17	0	20	0.91±0.22±0.09
$K^+K^-K^+K^-\pi^0$	14	0	12	1.3±0.4±0.3
$K^+K^-K^+K^-\eta$	1	0	11×0.389	$\leq$ 0.98 (at 90% C.L.)
$p^+p^-\pi^+\pi^-$	41	0	32	1.4±0.2±0.1
$p^+p^-\pi^+\pi^-\pi^0$	54	0	16	3.6±0.5±0.7
$p^+p^-\pi^+\pi^-\eta$	3	0	20×0.389	$\leq$ 0.93 (at 90% C.L.)

Table 6.IV Branching ratios of non–charmed hadronic decays. The factor 0.389 in the efficiencies comes from $Br(\eta \to \gamma\gamma) = 0.389$.

a final state not containing photons, the efficiency is determined directly. For a final state containing photons, the efficiency is studied to ensure that there is no significant bias in reconstruction. The efficiencies as a function of the invariant masses of the two photons for the $\pi^+\pi^-\pi^0$ mode are shown as the dashed line in Fig. 6.1.3. The efficiency for the other modes is very similar.

The efficiencies are listed in Table 6.IV.

The branching ratios and conclusion

The total cross section σ for each mode listed in Table 6.IV is the sum of $\sigma_{\psi(3770)} \times Br$ and the continuum production. The total cross section σ is determined from

Mode	Num. Events	$\epsilon_{recon.}(\%)$	$\sigma(4.14) \times 10^{-2}$ (nb)
$\pi^+\pi^-\pi^+\pi^-$	50	43	1.8±0.3±0.2
$\pi^+\pi^-\pi^+\pi^-\pi^0$	23	23	1.6±0.4±0.7
$\pi^+\pi^-\pi^+\pi^-\eta$	26	27×0.389	3.9±0.8±0.6
$K^+K^-K^+K^-$	3	25	≤0.42 (at 90% C.L.)
$K^+K^-K^+K^-\pi^0$	6	12	0.79±0.42±0.16
$K^+K^-K^+K^-\eta$	1	14×0.389	≤ 1.1 (at 90% C.L.)
$p^+p^-\pi^+\pi^-$	19	33	0.91±0.21±0.09
$p^+p^-\pi^+\pi^-\pi^0$	15	19	1.3±0.3±0.3
$p^+p^-\pi^+\pi^-\eta$	1	24×0.389	≤ 0.66 (at 90% C.L.)

Table 6.V Number of events and cross sections at 4.14 GeV.

$$\sigma = \frac{\text{"}Num.\ Events\text{"} - \text{"}Num.\ of\ Background\text{"}}{\epsilon_{recon.} \times L}, \tag{6.5}$$

where the "*Num. Events*" is the number of observed signal candidate events from Fig. 6.2.1 and Fig. 6.2.2; "*Num. of Background*" is the sum of $D\bar{D}$, $\psi(3685)$ and misidentification tracks; $\epsilon_{recon.}$ is the reconstruction efficiency determined from the Monte Carlo tests, and L is the total luminosity for this data sample.

For modes that do not contain π^0 and η, only those events having an χ^2–probability greater than 10 % are used.

The systematic errors are estimated in the following way:

1. For modes having no photons in the final state, the error is estimated to be 10% , which is due to mainly the unknown distribution of charged tracks in the detector and particle identification errors.

2. For modes having π^0 in the final state, the error is estimated to be 20% . 10% is due to the unknown distribution of the tracks in the detector and particle identification errors; 17% is due to the uncertainty in low–energy photon simulation.

3. For the final states containing an η , the uncertainty is estimated to be 15% . It is less than that for the π^0 case, as photon energies are higher.

6.3 Measurement at $\sqrt{s} = 4.14$ GeV

A data sample, at an energy close to but not on the $\psi(3770)$ resonance with a large integrated luminosity, would be necessary to determine the continuum background contributions in Table 6.IV. Since this data sample is not available, the data sample at 4.14 GeV, which is 370 MeV above the $\psi(3770)$, has been analyzed to improve our understanding of the OZI–suppressed decays of the $\psi(3770)$.

Table 6.V gives a list of the measurements of the 4.14 GeV data, based on the same reconstruction procedure as the measurements listed in Table 6.IV.

6.4 Conclusion

A number of possible non-$D\bar{D}$, non–charm hadronic decays have been observed at the $\psi(3770)$ resonance. Since the continuum background has not been measured, the branching ratios of the $\psi(3770)$ decay into these states cannot be determined directly . If we treat the measurements at 4.14 GeV as continuum and then assume that the cross section falls as $1/s$, the branching ratios of the non–charmed hadronic decays at the $\psi(3770)$ can be estimated (see Table 6.VI). Properly these should be viewed as lower bounds.

Mode	$\sigma_{\psi(3770)} \times Br.$ ($\times 10^{-2}$ nb)	Γ (keV) ($\sigma_{\psi(3770)} = 8.0 \pm 0.7$ nb)
$\pi^+\pi^-\pi^+\pi^-$	2.9±0.8	91±25
$\pi^+\pi^-\pi^+\pi^-\pi^0$	1.7±1.0	53±31
$\pi^+\pi^-\pi^+\pi^-\eta$	3.4±2.0	106±63
$K^+K^-K^+K^-$		
$K^+K^-K^+K^-\pi^0$		
$K^+K^-K^+K^-\eta$		
$p^+p^-\pi^+\pi^-$	0.28±0.38	9±12
$p^+p^-\pi^+\pi^-\pi^0$	2.1±1.0	66±31
$p^+p^-\pi^+\pi^-\eta$		

Table 6.VI Branching ratios treating 4.14 GeV as continuum.

7. CONCLUSION

The non–$D\bar{D}$ decays of the $\psi(3770)$ are observed and measured for the first time, including hadronic transitions, electromagnetic transitions and a number of non–charmed, hadronic, final states. These measurements provide us additional information to understand the quarkonium system, especially in the unique situation when quarkonium is in a D–wave and is mixed with an S–wave.

The hadronic transitions are measured to be:

$$\sigma_{\psi(3770)} \times Br(\psi(3770) \rightarrow \pi^+\pi^- + J/\psi) = (1.1 \pm 0.5 \pm 0.2) \times 10^{-2}\ nb \qquad (7.1)$$

and an upper limit:

$$\sigma_{\psi(3770)} \times Br(\psi(3770) \rightarrow \eta + J/\psi) \leq 3.5 \times 10^{-2}\ nb\ at\ 90\%\ C.L. \qquad (7.2)$$

The partial width $\Gamma(\psi(3770) \rightarrow \pi^+\pi^- + J/\psi)$ is related to the production cross section of the $\psi(3770)$. It has two different values since, as discussed in Chapter 1, the cross section has two different values, depending on the methods used for the measurement. Using the average, $\sigma_{\psi(3770)} = 8.0 \pm 0.7\ nb$, of the previous measurements, it is $34 \pm 14 \pm 7$ keV. Using the Mark III measurement $\sigma_{\psi(3770)} = 5.0 \pm 0.5\ nb$, it is $55 \pm 23 \pm 11$ keV. The later one is close to 71 keV, the predicted value calculated by using Kuang-Yan's method[17]. It requires the mixing angle to be (35^{+6}_{-9}) or (41^{+6}_{-8}) degrees for the prediction based on Moxhay's method, to be consistent with the measurement, using $\sigma_{\psi(3770)} = 8.0 \pm 0.7\ nb$ or $\sigma_{\psi(3770)} = 5.0 \pm 0.5\ nb$, respectively.

The angular and mass distributions of the two–pion system from the hadronic transition are measured (see Figs. 4.7.1 and 4.7.2). Because of limited statistics, the results do not allow significant conclusions when they are compared with the different predictions based on Eqs. 1.54, 1.56, 1.72, and 1.57.

Mode ($\psi(3770) \rightarrow$)	$\sigma_{\psi(3770)} \times Br.$ ($\times 10^{-2}$ nb)	$\Gamma(8.0 \pm 0.7$ $nb)$ (100×keV)	$\Gamma(5.0 \pm 0.5$ $nb)$ (100×keV)
$\gamma\chi_0$	10±4	3.2±1.2	5.1±1.9
$\gamma\chi_1$	8.8±3.2	2.8±1.0	4.4±1.6
$\gamma\chi_2$	$\leq$ 10. (90% $C.L.$)	$\leq$ 3.3 (90% $C.L.$)	$\leq$ 5.2 (90% $C.L.$)

Table 7.I: Radiative decay rates.

The electromagnetic transition rates are listed in Table 7.I.

A comparison between the measured widths and the predictions indicate that the measurements are more consistent with a total $\psi(3770)$ production cross section $\sigma_{\psi(3770)} = 8.0 \pm 0.7$ nb. With this cross section and similar measurements at the $\psi(3685)$, the mixing angles and the minimum χ^2 of the fit can be determined. The results are listed in Table 7.II. Combining these with the results from the hadronic transition, the relation of the χ^2 and the mixing angles is shown in Fig. 7.1.1.

Several non–charmed hadronic final states at the $\psi(3770)$ energy are observed with an undetermined continuum background and the results are listed in Table 7.III. The measurements of similar channels at 4.14 GeV may give some intuitive understanding of this continuum background. Based on the continuum background extrapolated from 4.14 GeV, the measurements in Table 7.III indicate a possibility of a large width of non–charmed, hadronic, final states.

One should understand that the determination of the continuum background at $\psi(3770)$ energy based on 4.14 GeV data is not well justified. At 4.14 GeV, it is not necessary that all the events arise from the uncharmed continuum, and it need not be the case that the cross section for the continuum varies $1/s$.

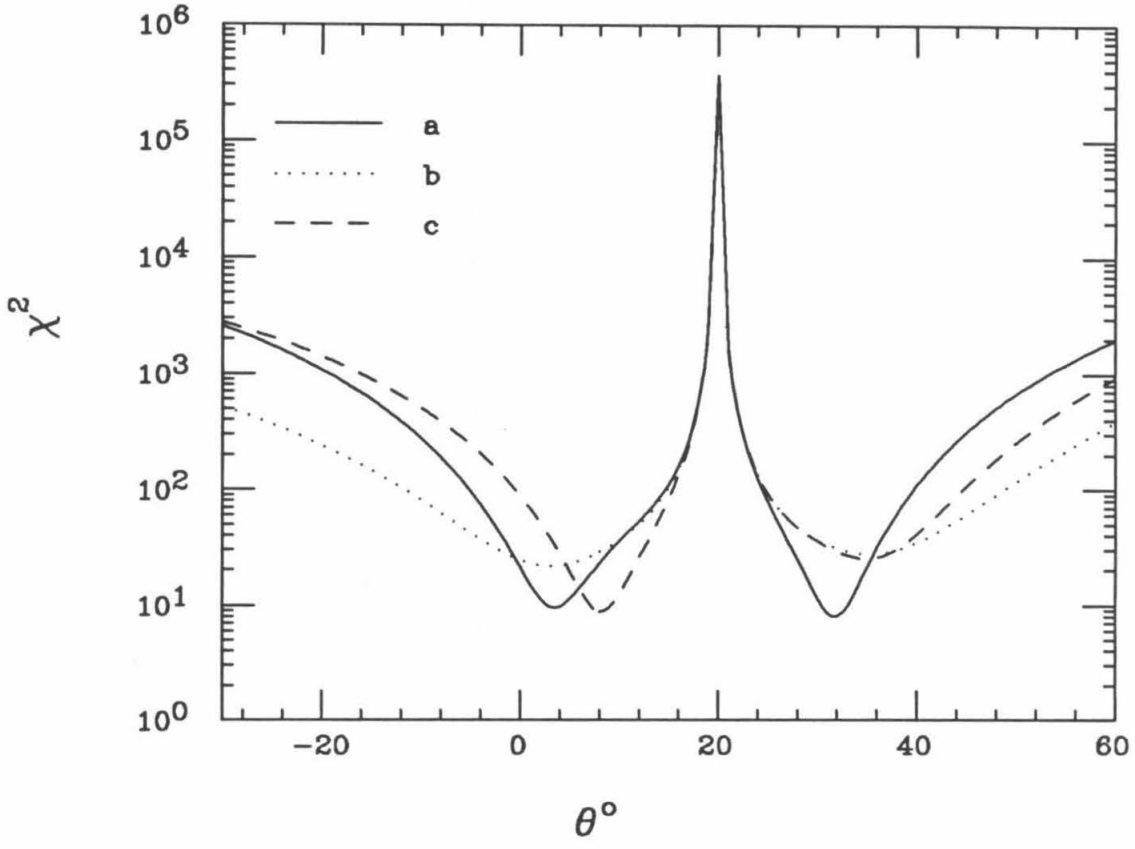

Figure 7.1.1: Comparing predictions, mixing angles and data. This figure showes the relationship between the χ^2 and the mixing angle based on the measured and the predicted values for the electromagnetic transition rates at the $\psi(3685)$ and $\psi(3770)$, the hadronic transition rate and the electronic annihilation rate at $\psi(3770)$. *a*). based on the prediction from Grotch[6]. *b*). based on the predictions from Daghighian and Silverman[22,47]. *c*). based on the predictions from Lane[40].

Finally, because of these measurements, we now have more knowledge about the quarkonium system. First, the hadronic transition rate of the $\psi(3770)$ is smaller than the $\psi(3685)$. The multipole expansion method gives a prediction

Model	χ^2_{small} (per Constraint)	θ_{small} (^{o})	χ^2_{large} (per Constraint)	θ_{large} (^{o})
Grotch[6]	0.4	2	1.7	32
Daghighian[22,47]	2.5	-1	2.9	36
Lane[40]	1.1	9	2.9	36

Table 7.II: Comparison with predictions and mixing angles.

correct in order of magnitude. The prediction based on Moxhay's method requires a large mixing angle between the 2^3S_1 and 1^3D_1, to be consistent with the data. There is also a suggestion that the mass distribution of the two pions does not agree with the predictions, as is also the case at the $\Upsilon(3S)$. The possibility of a very large mixing angle between S and D wave suggests that some decay properties of the $\psi(3685)$ and $\psi(3770)$ should be correlated and may lead to a resolution for the $V - P$ puzzle[23].

Second, the electromagnetic transition rates of the $\psi(3770)$ are found to be much larger than those of the $\psi(3685)$. Grotch's predictions with relativistic corrections are consistent with the measurements[6]. Two different mixing angles can be found based on the predictions; one is very small and one is very large. The larger angle is consistent with the mixing angle determined from the hadronic transition measurement.

Third, a large number of unexpected, non–charmed, hadronic final states are observed, but with uncertain contamination by a continuum background. The total rates are predicted to be about 50 keV; however, the measurements are at least a factor of six larger. If these large decay rates can be confirmed, they may be explained by the rescattering process. A comparison with the decays of the $\phi \rightarrow K\bar{K}$ will lead us to a further understanding of the strong coupling constant $\alpha_s(q^2)$.

Mode	$\sigma_{\psi(3770)} \times Br. + \sigma_{continue}$ $(\times 10^{-2}\ nb)$	$\sigma(4.14GeV)$ $(\times 10^{-2}\ nb)$	$\sigma_{\psi(3770)} \times Br.^{a}$ $(\times 10^{-2}\ nb)$
$\pi^+\pi^-\pi^0$	0.35±0.12±0.07		
$\pi^+\pi^-\eta$	0.59±0.27±0.12		
$\pi^+\pi^-\pi^+\pi^-$	5.1±0.3±0.5	1.8±0.3±0.2	2.9±0.8
$\pi^+\pi^-\pi^+\pi^-\pi^0$	3.6±0.4±0.7	1.6±0.4±0.7	1.7±1.0
$\pi^+\pi^-\pi^+\pi^-\eta$	8.2±1.0±1.2	3.9±0.8±0.6	3.4±2.0
$K^+K^-K^+K^-$	0.91±0.22±0.09	≤0.42 (90 % C.L.)	
$K^+K^-K^+K^-\pi^0$	1.3±0.4±0.3	0.79±0.42±0.16	
$K^+K^-K^+K^-\eta$	≤ 0.98 (90% C.L.)	≤ 1.1(90% C.L.)	
$p^+p^-\pi^+\pi^-$	1.4±0.2±0.1	0.91±0.21±0.09	0.28±0.38
$p^+p^-\pi^+\pi^-\pi^0$	3.6±0.5±0.7	1.3±0.3±0.3	2.1±1.0
$p^+p^-\pi^+\pi^-\eta$	≤ 0.93 (90% C.L.)	≤ 0.66 (90% C.L.)	

Table 7.III: Non–charmed final state decay rates. *a*). Obtained by using 4.14 GeV measurements as continuum background and assuming the cross sections of the continuum background scale as $\frac{1}{s}$.

APPENDIX

A: MAJOR PARAMETERS OF MARK-III DETECTOR[48]

Detector component	Thickness (% r.l.)
Beam pipe (1.5 mm thick Be)	0.40
Inner Trigger Chamber	0.68
Inner wall of drift chamber	0.16
Drift Chamber gas	0.75
Drift Chamber wires	0.15
Total above	2.14
ToF	12.0
Aluminum spool	28.0

Table A.I: Material thicknesses traversed by particles

Overall inner radius	14.47 cm
overall outer radius	114.26 cm
Layer 2:	
Length	177.8 cm. 32 cells
Number of wires/cell	15
Innermost wire N1	17.45 cm radius
Outermost wire N15	31.45 cm radius
Charge division wires N1 and N15	57μm diam. stainless steel
Sense wire N2 to N14	20μm diam. tungsten
Smallest half–width (at wire N2)	1.81 cm (400 ns)
Largest half–width (at wire N14)	2.99 cm (660 ns)
Displacement of alternate wires	$\pm$150μm
Layer 3-8:	
Length	233.7 cm
Number of wires/cell	5
N1 and N5, quard and charge division	57 μm diam. stainless steel
N2, N3 and N4, sense wires	20 μm diam. tungsten
Field wire	175 μm BeCu
Radius at center wire N3	13.45$\times L$ cm (L=layer number)
Number of cells/layer	16$\times L$
Angle of stereo layer 4	7.7^o
Angle of stereo layer 6	-9.0^o
Charge division	layer 3, 5 and 7
Half–cell width	2.64 cm $\simeq$ 580 ns
Staggering	$\pm$400μm

Table A.II: Drift chamber specifications.

Barrel shower counter:	
Spool length	385.0 cm
Spool outer diameter	252 cm
Spool thickness	2.3±0.4 cm
Flange outer diameter	261.8 cm
Cell width, inner layer	2.4 cm
Cell width, outer layer	3.2 cm
Gas thickness/cell	1.27 cm
Length of active volume (including anterior ribs)	348.00 cm
Number of layers	24
Thickness of aluminum sheets	0.064 cm
Thickness of Pb sheets	0.28 cm
Thickness of Al, Pb, Al glue sandwich	0.46 cm
Length of Pb sheets	348.00
Number of Pb per circumference	10
Width of ribs	2.67 cm
Height of I beams	1.24 cm
Width of top flange of I beams	1.02 cm
Thickness of I beam material	0.076 cm
Sense wire type	Stablohm 800 stainless steel
Sense wire diameter	46 μm
Gas	80% argon; 20% methane
Gas flow	10000 liters (one volume)/day

Table A.III: Barrel–shower counter specifications.

Endcaps:	
Front layer to interaction region	139.0 cm
Back layer to interacton region	177.8 cm
Radius of outer sensitive region	105.4 cm
Radius of inner sensitive region	35.0 cm (approx.)
Radius of outer assemblie	110.5 cm
Radius of inner assemblie	32.5 cm
Front solid angle subtended	$2 \times 8.5\% \times 4\pi$
Back solid angle subtended	$2 \times 6.5\% \times 4\pi$
Tube thickness, interior	1.17 cm
Tube width, interior	2.71 cm
Tube–wall thickness	0.064 cm
Pb sheet thickness/layer	0.279 cm
Adhesive thickness/layer	0.025 cm
Number of layers	24
Number of cells/layer	94
Sense wire type	Stablohm 800 stainless steel
Sense wire diameter	37 μm
Gas	80% argon; 20% methane
Gas fllow	one volume/day
Polar angle of sensitive regions	
Front outer	37.2^o
Front inner	14.1^o
Back outer	31.9^o
Back inner	11.1^o

Table A.IV: End cap shower counter specifications.

Total modules	135
Tubes/module	8
Overlape of adjacent tubes	1/3 tubes
Tube size	5 cm outer diameter, 4.2 m long
Sense wire	50 μm s.s. 380 Ω/m for charge division
Gas	80% argon, 20% methane, 100 ppm O_2
Gas flow	1 vol./36 hrs.
Absorber for inner layer	coil, shower counter and 20 cm iron
Absorber for outer layer	an additional 13 cm iron
Resolution in azimuth	1 cm (4 mr)
Resolution axially	6 cm (24 mr)
Calibration	Charge injection directly on wires
Mutiple Scattering for 1 GeV/c muons:	
Inner layer	5 cm equivalent
Outer layer	9 cm equivalent

Table A.V: Muon system specifications.

REFERENCES

1. G. Goldhaber, F. Pierre, G. Abrams *et al.*, *Phys.Rev.Lett.* **37** (1976) 255.
2. M. Aguilar-Benitez *et al.*, *Phys.Lett.* **170B** (1986) 1.
3. P. Rapidis, *et al. Phys.Rev.Lett.* **39** (1977) 526; *Phys.Rev.Lett.* **39** (1977) 1301 .
4. W. Bacino, *et al.*, *Phys.Rev.Lett.* **40** (1977) 526.
5. J. Adler, *et al.*, A Reanalysis of Charmed D Meson Branching Fractions, SLAC-PUB-4291, June 1987.
6. H. Grotch, X. Zhang and K. J. Sebastian, *Phys.Rev.* **35D** (1987) 2900.
7. H. J. Lipkin, *Nucl.Phys.* **B244** (1984) 147; *Phys.Lett.* **179B** (1986) 278.
8. M. E. B. Franklin, *et al.*, *Phys.Rev.Lett.* **51** (1983) 963; M. E. B. Franklin, Ph.D. Thesis: Selected Studies of Charmonium Decays, SLAC-PUB-254, Aug. 1982.
9. For more detail, see J. M. Jauch and F. Rohrlich: The Theory of Photons and Electrons, Second Expanded Edition, Springer-Verlag, New York, Heidelberg, Berlin,(1976).
10. A.Ore and J. L. Powell, *Phys.Rev.* **75** (1949) 1696.
11. G. Belanger and P. Moxhay, *Phys.Lett.* **B199** (1987) 575.
12. T. Appelquist, R. M. Barnett and K. Lane, *Ann.Rev.Nucl.Part.Sci.* **28** (1978) 387; M. Krammer, H. Krasemann, Lectures given at 18th Int. Universitatswochen fur Kernphysik, Schladming, Austria, Feb. 28 - Mar. 10, 1979. Published in Schladming School, 1979:259.
13. Y. M. Li and J. Z. Zhang, *Nuovo.Cim.* **97A** (1987) 281-288.
14. H. J. Schnitzer, *Phys.Rev.Lett.* **35** (1975) 1540.; J. Pumplin, W. Repko and A. Sato, *Phys.Rev.Lett.* **35** (1975) 1538; H. J. Schnitzer, *Phys.Lett.* **65B** (1976) 239.

15. V. A. Novikov, *et al.*, Phys. Rep. 41, No.1 (1978), 1-133.

16. T. M. Yan, *Phys.Rev.* **D22** (1980) 1652.

17. Y. P. Kuang and T. M. Yan, *Phys.Rev.* **D24** (1981) 2874.

18. Y. P. Kuang, S. F. Tuan and T. M. Yan, $^1P_1$ States of Heavy Quarkonia, UH-511-611-87.

19. T. Bowcock, *et al.*, *Phys.Rev.Lett.* **58** (1987) 307.

20. E. Eichten, *et al.*, *Phys. Rev. Lett.*, **34** (1975) 369 ; **36** (1976) 500.

21. E. Eichten, *et al.*, *Phys. Rev.* **D17**, 3090 (1978) ; **D21**, (1980) 203.

22. F. Daghighian and D. Silverman, *Phys.Rev.* **D36** (1987) 3401.

23. S. J. Brodsky, G. P. Lepage and S. F. Tuan, Exclusive Charmonium Decays: The J/ψ ($\psi(3685)$)$\rightarrow \rho\pi$, $K^*\bar{K}$ Puzzle, SLAC-PUB-4276, UH-511-618-87, May, 1987.

24. M. Voloshin and V. Zakharov, *Phys.Rev.Lett.* **45** (1980) 688.

25. A. Billoire, R. Lacaze, A. Morel and H. Navelet, *Nucl.Phys.* **B155** (1979) 493-508.

26. H. Goldberg, *Phys.Rev.Lett.* **35** (1975) 605.

27. K. Gottfried, *Phys.Rev.Lett.* **40** (1978) 538.

28. M. Peskin, *Nucl.Phys.* **B156** (1979) 365; G. Bhanot and M. Peskin, *Nucl.Phys.* **B156** (1979) 391.

29. P. Moxhay, "Hadronic Transitions of D-wave Quarkonium," COLO-HEP-163, Nov. 1987.

30. V.A. Novikov and M.A. Shifman, *Z.Phys.* **C8** (1981) 43.

31. H. Yamamoto, A. Nishimura and Y. Yamaguchi, *Prog.Theor.Phys.* **58** (1977) 374; **59** (1977) 2151.

32. S. P. Misra, K. Biswal, and B. K. Parida, *Phys.Rev.* **D21** (1980) 2029; S. P. Misra, *Phys. Rev.* **D18** (1978) 1661; S. P. Misra, *Phys. Rev.* **D18** (1978) 1673.

33. S. Okubo, *Phys.Lett.* **5** (1963) 165; G. Zweig, CERN Reports Nos. TH 401, 1964; TH 412 1964; J. Iizuka, *Prog.Theor.Phys.Supp.* **21** (1966) 37-38.

34. W. Kwong, P. B. Mackenzie, R. Rosenfeld and J. L. Rosner, EFI 87-31.

35. J. E. Gaiser *et al.*, *Phys.Rev.* **D34** (1986) 711.

36. D. M. Coffman, Ph.D. Thesis: The Properties of Semileptonic Ddecays of Charmed D Mesons, CALT-68-1415.

37. R. H. Schindler, Ph.D. Thesis: Charmed Meson Production and Decay Properties at the $\psi(3770)$, SLAC-219 , UC-34d, (T/E), May 1979.

38. T. M. Himel, Ph.D. Thesis: Decays of the $\psi'(3684)$ to Other Charmonium States, SLAC-223 , UC-34d, (T/E/I), October 1979.

39. R. A. Partridge, Ph.D. Thesis: A Study of The $\psi''(3770)$ Using the Crystal Ball Detector, CALT-68-1150 , Feb., 1984.

40. K. Lane, HUPT-86/A045,6/1986.

41. M. Wise, private communication. The angular distributions of the photons from the ψ' and $\psi(3770)$ should be the same. The $\psi(3685)$ distribution is predicted by Ref.(20).

42. G. Bonneau and F. Martin, *Nucl. Phys.* **B27** (1971) 381.

43. G. Blaylock, Ph.D. Thesis, Direct Measurement of the Decays of Charmed D Mesons, RX-1127 (ILLINOIS) 1986.

44. I. Peruzzi, *et al.*, *Phys. Rev. Lett.* **39** (1977) 1301.

45. The major difference is in σ_ϕ. The average σ_ϕ of real photons is 20% higher than in the Monte Carlo. This difference is negligible in this analysis since the errors on the direction of missing momentum are much larger than the magnitude of σ_ϕ.

46. It is instructive to see how the equations are arrived at in the QED case. In QED:

$$U(\vec{x},t) = exp\Big(ie\int_0^{\vec{x}} d\vec{x'}\cdot\ \vec{A}(\vec{x'},t)\Big),$$

where the integral is along a straight line from 0 to $\vec{x}$;

$$A'_\mu = U^{-1}A_\mu U - \frac{i}{e}U^{-1}\partial_\mu U.$$

Using this U with the relationship of A and A', one can get:

$$A'_0(\vec{x},t) = A_0(\vec{x},t) + \int_0^{\vec{x}} d\vec{x'}\ \frac{\partial\vec{A}(\vec{x'},t)}{\partial t}$$

$$\vec{A'}(\vec{x},t) = \vec{A}(\vec{x},t) - \nabla\int_0^{\vec{x}}\ d\vec{x'}\cdot\vec{A}(\vec{x'},t).$$

Using,

$$\vec{E} + \nabla A_0 + \frac{\partial\vec{A}}{\partial t} = 0,$$

from electrodynamics and defining:

$$\vec{x'} = s\vec{x}, \quad 0 < s < 1,$$

we get:

$$A'_0(\vec{x},t) = A_0(0,t) - \int_0^1 ds\vec{x}\cdot\vec{E}(s\vec{x},t)$$

$$\vec{A'}(\vec{x},t) = -\int_0^1\ ds\vec{x}\times\vec{B}(s\vec{x},t).$$

where $\vec{E}$ and $\vec{B}$ are the electric and magnetic field, respectively. For QCD case, more detail can be found in Ref.(16).

47. D. Silverman, private communication.

48. D. Bernstein, *et al.*, *Nucl.Instr.Meth.* **226** (1984) 301.